Non-Linear Fibres for Widely Tunable Femtosecond Fibre Lasers

Pedersen, Martin Erland Vestergaard

Publication date:
2013

Document Version
Publisher's PDF, also known as Version of record

DTU Fotonik
Department of Photonics Engineering

Non-Linear Fibres for Widely Tunable Femtosecond Fibre Lasers

Martin Erland Vestergaard Pedersen

30th April 2013

Revision 1.0 - 30th June 2013

Department of Photonics Engineering
Technical University of Denmark

OFS Fitel Denmark

Contents

Preface

This thesis is submitted in candidacy for the Ph.D. degree from the Technical University of Denmark. The work presented is the result of the Industrial Ph.D. programme supported by the Danish Agency for Science, Technology, and Innovation. The partners of this Industrial Ph.D. programme was OFS Fitel Denmark and the Fiber Optics, Devices & Nonlinear Effects group at DTU Fotonik - Department of Photonics Engineering. The project was carried out from 1st November 2009 to the end of April 2013, with a leave for a period of six months from the Ph.D. project from 1st November 2011 to the end of April 2012. During the leave work was performed as full time employee at Incubation Center at OFS Fitel Denmark, with a focus on polarisation-maintaining fibres.

The work during the Ph.D. project was conducted at OFS Fitel Denmark, DTU Fotonik, Cornell University, and Imperial College London. The project has been supervised by

- Karsten Rottwitt, Professor, dr.techn., Department of Photonics Engineering, Technical University of Denmark, Kgs. Lyngby
- Kim Giessmann Jespersen, Ph.D., OFS Fitel Denmark, Brøndby
- Lars Grüner-Nielsen, Ph.D., OFS Fitel Denmark, Brøndby

Lars Grüner-Nielsen replaced Kim Giessmann Jespersen as supervisor at the company for the last two months of the project, as Kim Giessmann Jespersen acquired a new employment.

Acknowledgments

First of all, I should like to thank my supervisors Karsten Rottwitt, Kim Giessmann Jespersen, and Lars Grüner-Nielsen for the encouragement and the many fruitful discussions.

Secondly, I should like thank Chris Xu and his group at Cornell University for our close and beneficial collaboration during the project and for being so friendly to me on my two visits to Cornell University.

Thirdly, I should like to thank Roy Taylor for allowing me to join his Femtosecond Optics Group at Imperial College London for a period of 4 months. I should especially also like to thank the entire Femtosecond Optics Group for the delightful collaboration both in and outside the optics laboratory during my visit.

I should also like to thank the many good people who have passed through the office at Technical University of Denmark over the years and contributed to brighten up the days, especially I would like to thank Anders Tegtmeier Pedersen, Christian Agger, Henrik Steffensen, Johan Raunkjær Ott, Lars Søgaard Rishøj, and Mikkel Heuck.

Also I should like to thank the good people at OFS Fitel Denmark. Especially, I should like to thank the entire Incubation Center.

Last but certainly not least, I should like to thank Dorthe Fuglede and Lars Søgaard Rishøj for their meticulous proofreading, and Lars Søgaard Rishøj for posing so many intelligent questions.

Martin Erland Vestergaard Pedersen
Kongens Lyngby, Denmark, 30$^{\text{th}}$ April, 2013.

Abstract

This Ph.D. thesis investigates how intramodal and intermodal non-linear processes in few-moded fibres can be used to generate light sources at wavelengths outside the spectral gain-bands of rare-earth-doped optical-fibres.

The design of two specialty few-moded fibres for use in a widely tunable femtosecond fibre laser is presented. The two fibres are used to facilitate the shifting of a soliton in a cascade configuration from the ytterbium gain-band and to a wavelength of 1280 nm. The temporal pulse duration is on a femtosecond scale with a pulse energy of 5 nJ. The experimentally observed soliton self-frequency shift and thereby the outcome of the experimental demonstration of the widely tunable femtosecond fibre laser is shown to depend highly on the chirped of the input pulse into the first few-moded fibre in the cascade setup. Furthermore, an alternative splicing process, with a combination of a fusion splicer and a gas-line burner, is applied to the few-moded fibres.

An intermodal four-wave mixing process and a novel intermodal Čerenkov generation process are demonstrated experimentally in one of the two speciality few-moded fibres. The two intermodal processes are described theoretically and numerically. For the intermodal four-wave mixing experiment an alternative version of the Generalised Non-Linear Schrödinger Equation is derived, which includes the correct dispersion of the transverse field. It is observed that the alternative version of the Generalised Non-Linear Schrödinger Equation, as opposed to the commonly used version, is able to reproduce the intermodal four-wave mixing experiment.

The relation between the intramodal self-phase modulation and the intramodal Raman effect is determined from experimental measurements on a number of step-index fibres. The Raman fraction is found to vary with the germanium concentration. For the considered step-

index fibres the Raman fraction varies from 0.16 to 0.15 with increasing germanium concentration, which is lower than the often cited value of 0.18.

Furthermore, an extensive work regarding modelling of mode-locked lasers was performed. The result of this is reported for an all-normal dispersive polarisation-maintaining laser.

Resumé (In Danish)

I denne ph.d. afhandling undersøges det, hvordan ikke-lineære processer bestående af interaktioner imellem den samme *tilstand af lyset*[1] og imellem forskellige *tilstande af lyset* kan bruges til at generere lyskilder ved bølgelængder, som ligger uden for det spektrale forstærkningsområde af optiske fibre doteret med sjældne jordarter, hvor de før nævnte ikke-lineære processer foregår i fibre som understøtter et begrænset antal *tilstande af lyset*.

Designet af to specielle fibre som understøtter et begrænset antal *tilstande af lyset* er præsenteret. Fibrene er designet til anvendelse i en femtosekund fiberlaser, hvor det er muligt at indstille bølgelængden af lyspulsen i et meget bredt område. Bølgelængden af lyspulsen ændres ved at udnytte solitonpulsens egenskab til at skifte sin egen frekvens. Skiftet af solitonpulsen foregår fra forstærkningsområdet af ytterbium til en bølgelængde på 1280 nm ved at bruge de to specielle fibre i en kaskade konfiguration. Den skiftede solitonpuls har en pulsenergi på 5 nJ og en pulsbrede på en femtosekund skala. Den eksperimentelle observation af solitonpulsens egenskab til at skifte sin egen frekvens viser sig at være meget afhængig af fasen på den oprindelig puls som kobles ind i den første af to specielle fibre. Da den eksperimentelle demonstration af femtosekund fiberlaser er direkte relateret til solitonpulsens egenskab til at skifte sin egen frekvens, får fasen på den oprindelig puls også en betydning for resultatet af den eksperimentelle demonstration. Endvidere er en alternativ splejsningsmetode anvendt på fibrene som understøtter et begrænset antal *tilstande af lyset*. Den alternative splejsningsmetode består af en kombination af et fusionssplejsningsapparat og en gaslinjebrænder.

I en af de to specielle fibre som understøtter et begrænset antal *til-*

[1] Oversat fra det engelske begreb "mode", som i dette tilfælde betegner tilstanden af lyset i en optisk fiber.

stande af lyset er en blandingsproces med fire bølger imellem forskellige *tilstande af lyset* og en Čerenkov genereringsproces imellem forskellige *tilstande af lyset* eksperimentelt demonstreret. De to processer imellem forskellige *tilstande af lyset* er beskrevet både teoretisk og numerisk. I forbindelse med eksperimentet med blandingsprocessen med fire bølger imellem forskellige *tilstande af lyset* er der udledt en alternativ udgave af den generelle ikke-lineær Schrödinger ligning, som i modsætning til den almindeligt anvendte udgave er i stand til at genskabe eksperimentet med blandingsprocessen med fire bølger imellem forskellige *tilstande af lyset*.

Forholdet mellem modulationen til egen fase af den samme *tilstand af lyset* og Raman effekten af den samme *tilstand af lyset* er bestemt ud fra målinger på en række fibre med en indeksprofil bestående af en flad cirkulær kerne med højere indeks end den omkringliggende kappe. For disse fibre varierer Raman brøkdelen fra 0,16 til 0,15 for en stigende koncentration af germanium, hvilket er lavere end den ofte citerede værdi på 0,18.

Derudover er der blevet udført et omfattende arbejde angående modellering af lasere hvor *tilstanden af lyset* er fastlåst. Resultatet af dette arbejde er præsenteret for en laser, som består af fiberstykker der alle har normale dispersions egenskaber og samtidig er polarisationsbevarende.

List of Publications

The work carried out during this Ph.D. project has resulted in the following publications and patents, which have been separated into two groups, one for the publications and patents that forms the basis for the thesis and one for the work which is outside the scope of this thesis :

The Basis for the Thesis

Pending Patent Applications

- PCT International Patent Application for
  "Fiber Designs for Wavelength Tunable Ultra-Short Pulse Lasers,"
  L. Grüner-Nielsen, D. P. Jakobsen, M. E. V. Pedersen, C. Xu, J. Cheng

- United States Patent Application for
  "Optical Mode Conversion by Nonlinear Effects,"
  L. Grüner-Nielsen, D. P. Jakobsen, M. E. V. Pedersen, C. Xu, J. Cheng

- United States Patent Application for
  "Optical Mode Conversion Using Intermodal Cherenkov Radiation,"
  L. Grüner-Nielsen, D. P. Jakobsen, M. E. V. Pedersen, C. Xu, J. Cheng

Accepted Journal Papers

- J. Cheng, M. E. V. Pedersen, K. Charan, K. Wang, C. Xu, L. Grüner-Nielsen, and D. Jakobsen, "Intermodal cherenkov radiation in a

higher-order-mode fiber," *Opt. Lett.*, vol. 37, no. 21, pp. 4410–4412, Nov 2012.

- J. Cheng, M. E. V. Pedersen, K. Charan, K. Wang, C. Xu, L. Gruner-Nielsen, and D. Jakobsen, "Intermodal four-wave mixing in a higher-order-mode fiber," *Applied Physics Letters*, vol. 101, no. 16, p. 161106, 2012.

- M. E. V. Pedersen, J. Cheng, K. Charan, K. Wang, C. Xu, L. Grüner-Nielsen, and D. Jakobsen, "Higher-order-mode fiber optimized for energetic soliton propagation," *Opt. Lett.*, vol. 37, no. 16, pp. 3459–3461, Aug 2012.

- M. E. V. Pedersen, E. Kelleher, J. Travers, Z. Sun, T. Hasan, A. Ferrari, S. Popov, and J. Taylor, "Stable gain-guided soliton propagation in a polarized yb-doped mode-locked fiber laser," *Photonics Journal, IEEE*, vol. 4, no. 3, pp. 1058 –1064, june 2012.

- J. Cheng, M. E. V. Pedersen, K. Wang, C. Xu, L. Grüner-Nielsen, and D. Jakobsen, "Time-domain multimode dispersion measurement in a higher-order-mode fiber," *Opt. Lett.*, vol. 37, no. 3, pp. 347–349, Feb 2012.

- M. E. V. Pedersen, P. Kristensen, L. Gruner-Nielsen, and K. Rottwitt, "Impact of the scalar approximation on the prediction of the group velocity dispersion," *Lightwave Technology, Journal of*, vol. 29, no. 21, pp. 3129 –3134, nov.1, 2011.

Accepted Conference Contributions

- J. Cheng, M. E. V. Pedersen, K. Charan, K. Wang, C. Xu, L. Grüner-Nielsen, and D. Jakobsen, "Simultaneous wavelength and mode conversion in a higher-order-mode fiber," in *Frontiers in Optics Conference*. Optical Society of America, 2012, p. FW5D.4.

- J. Cheng, M. E. V. Pedersen, K. Charan, C. Xu, L. Gruner-Nielsen, and D. Jacobsen, "High-efficiency intermodal four-wave mixing in a higher-order-mode fiber," in *Lasers and Electro-Optics (CLEO), 2012 Conference on*, may 2012, pp. 1 –2.

- M. E. V. Pedersen, J. Cheng, K. Charan, K. Wang, C. Xu, L. Grüner-Nielsen, and D. Jakobsen, "Optimization of a higher-order-mode

fiber for energetic soliton propagation," in *CLEO: Science and Innovations*. Optical Society of America, 2012, p. CTh4G.2.

- M. E. V. Pedersen, T. Palsson, K. Jespersen, D. Jakobsen, B. Palsdottir, and K. Rottwitt, "The raman contribution to the intensity dependent refractive index in optical fibers," in *Photonics Conference (PHO), 2011 IEEE*, oct. 2011, pp. 571 –572.

Submitted Publications

- M. E. V. Pedersen, J. Cheng, C. Xu, and K. Rottwitt, "Transverse field dispersion in the generalised non-linear schrödinger equation: Four wave mixing in a higher-order-mode fiber," *Lightwave Technology, Journal of*.

- K. Charan, M. E. V. Pedersen, K. Wang, L. Grüner-Nielsen, D. Jakobsen, and C. Xu, "Experimental demonstration of soliton cascade in higher-order-mode fibers," *Opt. Lett.*.

Outside the Scope of the Thesis

Accepted Journal Papers

- S. H. M. Larsen, M. E. V. Pedersen, L. Grüner-Nielsen, M. F. Yan, E. M. Monberg, P. W. Wisk, and K. Rottwitt, "Polarization-maintaining higher-order mode fiber module with anomalous dispersion at 1 μm," *Opt. Lett.*, vol. 37, no. 20, pp. 4170–4172, Oct 2012.

- K. G. Jespersen, T. Le, L. Grüner-Nielsen, D. Jakobsen, M. E. V. Pedersen, M. B. Smedemand, S. R. Keiding, and B. Palsdottir, "A higher-order-mode fiber delivery for ti:sapphire femtosecond lasers," *Opt. Express*, vol. 18, no. 8, pp. 7798–7806, Apr 2010.

Accepted Conference Contributions

- T. Geisler, M. E. V. Pedersen, S. Herstrøm, "Measurement of Spatial and Polarization Birefringence in Two-Mode Elliptical Core Fibers," in *Optical Fiber Communication (OFC), 2013 Conference on*, march 2013, p. OW1K.3.

- L. Grüner-Nielsen, S. Herstrøm, S. Dasgupta, D. Richardson, D. Jakobsen, C. Lundström, P. Andrekson, M. E. V. Pedersen, and B. Palsdottir, "Silica-based highly nonlinear fibers with a high sbs threshold," in *Winter Topicals (WTM), 2011 IEEE*, jan. 2011, pp. 171 –172.

- L. Grüner-Nielsen, S. Dasgupta, M. Mermelstein, D. Jakobsen, S. Herstrom, M. E. V. Pedersen, E. Lim, S. Alam, F. Parmigiani, D. Richardson, and B. Palsdottir, "A silica based highly nonlinear fibre with improved threshold for stimulated brillouin scattering," in *Optical Communication (ECOC), 2010 36th European Conference and Exhibition on*, sept. 2010, pp. 1 –3.

Chapter 1

Introduction

In the following the background and motivation for the Ph.D. project is given. This is followed by a short description of the content and structure of the thesis.

1.1 Background & Motivation

In 1960 Theodore Maiman carried out the first demonstration of the lasing principal in a ruby crystal [1] based on the theoretical concept presented by Schawlow and Townes [2]. Since the first demonstration the field of lasers evolved quickly and most of the significant and fundamental discoveries within the field of lasers were obtained in the 1960s. Maiman's demonstration was shortly after followed by the first demonstration of a gas laser by Ali Javan *et al.* [3]. In 1961 the first demonstration of light generated by a non-linear process was shown [4]. Unfortunately, the editor of the journal mistook part of the recorded spectrum, which was generated by a second-harmonic process, as a misprint and removed it in the final edition of the paper, thereby removing the experimental documentation for the first observed optical non-linear effect. The first fibre laser was also demonstrated in 1961 [5] and in 1962 the first semiconductor laser was a realisation [6]. The laser has since then defined and revolutionised numerous scientific fields and our everyday life.

With the development of the low-loss fibre, the way was paved for the vast optical networks, which today spans the Earth connecting the majority of the population of the world to each other. In 2009 half of the Nobel prize in Physics was given to *Charles K. Kao* for his "ground-

breaking achievements concerning the transmission of light in fibers for optical communication" [7]. The fibre optics research community has benefited greatly from the advancement of the telecommunication industry. The fibre laser has several unique properties, some of these properties are that the laser is free of alignment of bulk components and therefore very robust, less sensitive to the environment, and requires less maintenance. The properties are of high interest for many of the commercial and industry applications involving lasers. A common method used in fibre lasers is to dope the fibre with rare earth elements, e.g. ytterbium, erbium, and thulium to obtain lasing in discrete spectral windows in the infra-red region [8]. It is possible to dope with other materials to obtain lasing in other spectral windows, however, these aforementioned rare-earth elements provide the highest conversion efficiencies. An often applied strategy, for lasing outside these spectral windows, is to utilise non-linear effects for generating light at other wavelengths. As the strength of the non-linear process is related to the peak power of the light, it is advantageous to generated the input light to the non-linear process with the aforementioned rare-earth elements. For most cases the non-linear processes include higher-harmonic generation, four-wave mixing (FWM), Raman scattering, and soliton self-frequency shift (SSFS) [9].

Fibres which supports more than the fundamental mode are generally denoted multi-mode fibres (MMFs). Historically, MMFs have been designed to support hundreds of modes [10], however, in recent years there have been a renewed interest in fibres, which only support a couple of modes. These fibres are denoted higher-order-mode (HOM) fibres or few-moded fibres (FMFs). In the beginning of the 1990s the first demonstration of dispersion compensation using a HOM in an optical fibre was carried out [11,12]. The interest was renewed in 2001 with a demonstration of an all-fibre system for a communication link over 1000 km using a HOM for the dispersion compensation [13]. The properties of HOMs also provide a path for bend-insensitive large-mode-area fibres [14] and anomalous dispersion below 1.3 μm [15]. However, it is within optical communications that the FMF has received the largest amount of attention, since space-division multiplexing could potentially increase the communication capacity significantly [16–19].

The Ti:Sapphire laser has had and will presumably continue to have a significant impact with the field of optics and lasers for the years to come. The state of the art commercial Ti:Sapphire laser can provide less

than 20 fs pulses with a tuning range of approximately 100 nm. When used in combination with an optical parametric oscillator, this tuning range can be extended to an impressive wavelength tuning range from 750 nm to 1600 nm. The Ti:Sapphire laser is the workhorse of nearly all time-resolved research owing to its flexibility, high pulse quality, and high pulse energies.

As the Ti:Sapphire laser is very versatile one very significant goal within the field of fibre laser would be to construct an all fibre-based counterpart of the Ti:Sapphire laser. The main focus of the Ph.D. project has been to make an all fibre-based short-pulse laser, which could be tuned to deliver pulse in the wavelength from the ytterbium gain-band region to approximately at a wavelength of 1.3 μm, as this could have a potential application within a number of fields. Furthermore, the possibility of having a fibre delivery with diffraction-limited output generates a high practical value to such a fibre laser. The fibre delivery can e.g. provide high quality light for microscopic imaging or enable delivery of light into human tissue, *in vivo*, for diagnostic purposes. The specific properties, such as the high peak-power, of the tunable femtosecond fibre laser make it highly suitable for non-linear processes such as multi-photon spectroscopy, which is an emerging application of femtosecond pulses in biophotonics [20–24]. *In vivo* deep-tissue multi-photon microscopy requires a significant pulse energy in order to achieve adequate signal-to-noise ratio and a fast frame rate. This requires output pulse energies greater than 5 nJ from the source. To facilitate the wavelength tuning of the femtosecond pulses an approach is to use SSFS [25, 26]. To support a soliton the considered fibre is required to have anomalous dispersion to counter the accumulated non-linear phase-shift. Micro-structured photonic-crystal fibres (PCFs) could be used to support a soliton in this wavelength region, however, generally PCFs have a small effective mode area in order to provide the required anomalous dispersion [27, 28]. Therefore the energy of the soliton is also small and in general pulse energies of sub-nanojoules is obtained. A hollow core photonic bandgap fibre could be used to support a soliton, but with the extremely low non-linearity the energy of the soliton would be very large and in the range of hundreds of nanojoules [29]. Unfortunately, this pulse energy is too high for any *in vivo* application in human tissue. In between these two energy regions are the soliton pulse energy in a FMF. Previous reports of the soliton energy in FMFs have been limited to around 1 nJ in this wavelength

region [30]. Therefore, the main focus of the Ph.D. project has been to design and construct a fibre-based laser system, which is able to deliver a wavelength tunable femtosecond pulse with a pulse energy of 5 nJ. The laser system is to be pumped by an ytterbium-based source and to shift the pulses to 1280 nm.

1.2 Content of the Thesis

To ease the reading experience, acronyms are used throughout the thesis. The definition of an acronym is provided in each chapter for the first appearance of the acronym. The complete list of acronyms can be found in App. C.

To give a more detailed overview of the chapters in this thesis a short description of each chapter is given in this section. The structure of the thesis is as follows:

- **In Chap. 2** the governing equation for the pulse propagation, which is Generalised Non-Linear Schrödinger Equation (GNLSE), is derived from Maxwell's equations. The GNLSE is derived in order to expand the framework of the GNLSE to include multi-mode (MM) interaction and the correct dispersion of the transverse field distribution. In the end of the chapter the framework for the modesolver used throughout the project is briefly explained.

- **In Chap. 3** there is an investigation of the Raman contribution to the intensity-dependent refractive index for a number of step-index silica-based fibres with a germanium-doped core and cladding of pure silica.

- **In Chap. 4** the general outline and optimisation of the designs of the two essential FMFs are presented. This is followed by a characterisation of the two essential FMFs and a consideration on how to excite the desired $LP_{0,2}$ mode. The two essential FMFs are denoted by the acronym of their project names throughout the thesis. The fibres are referred to as the left-sided fibre (LSF) and the right-sided fibre (RSF). The origin for the project names is explained in the chapter. The chapter is rounded off with a section about splicing two different FMFs together.

- **In Chap. 5** the two fibre-based oscillators, which are utilised in this project are presented. They both use an ytterbium-doped fibre as the gain medium. The first of the oscillators, a HOM dispersion-balanced laser, is used to excite a soliton in the two essential FMFs. The second oscillator, an all-normal dispersive (ANDi) polarisation-maintaining (PM) laser, has been subjected to a more thorough theoretical investigation.

- **In Chap. 6** the simulated and experimentally observed SSFSs to longer wavelengths are presented in the LSF and the RSF for an input pulse, which is either an unchirped femtosecond pulse or a chirped picosecond pulse.

- **In Chap. 7** the two different intermodal non-linearity processes, which were observed in the LSF, are presented together with the theoretical explanation of the two processes. The two processes are an intermodal FWM process and an intermodal Čerenkov process. The derived GNLSE with the correct dispersion of the transverse field distribution from Chap. 2 is shown to be of importance when simulating the intermodal FWM experiment in the LSF.

- **In Chap. 8** the conclusion of the thesis is presented.

- **In Chap. 9** the outlook with recommendations for continuation of the project is presented.

Chapter 2

Theory

In this chapter the main theoretical foundation for this work is presented. The starting point is Maxwell's equations from which the governing equation for propagation of an optical pulse through an optical fibre is derived, which is known as the Generalised Non-Linear Schrödinger Equation (GNLSE). The GNLSE is both expand to included multiple modes and rewritten to include the correct dispersion of the transverse field. Finally, the framework for the applied modesolver is briefly presented.

2.1 Maxwell's Equations

Light is a special form of electromagnetic radiation. Electromagnetic radiation is governed by Maxwell's equations. Maxwell's equations are the basic foundation for describing the physical dynamics of light. Therefore, the theory presented in this work will start the derivation from Maxwell's equations. The Maxwell's equations are

$$\boldsymbol{\nabla} \times \mathbf{E} = -\frac{\partial \mathbf{B}}{\partial t}, \tag{2.1.1}$$

$$\boldsymbol{\nabla} \times \mathbf{H} = \mathbf{J}_f + \frac{\partial \mathbf{D}}{\partial t}, \tag{2.1.2}$$

$$\boldsymbol{\nabla} \cdot \mathbf{D} = \rho_f, \tag{2.1.3}$$

$$\boldsymbol{\nabla} \cdot \mathbf{B} = 0, \tag{2.1.4}$$

where $\mathbf{E}$ is the electric field, $\mathbf{B}$ is the magnetic field, $\mathbf{D}$ is the electric displacement field, $\mathbf{H}$ is the magnetising field, $\mathbf{J}_f$ is the free current

density, ρ_f is the free charge density, t is the time, and $\boldsymbol{\nabla}$ is the nabla operator. All the symbols in bold are vectors. The auxiliary fields are given as

$$\mathbf{D} = \varepsilon_0 \mathbf{E} + \mathbf{P}, \tag{2.1.5}$$

$$\mathbf{B} = \mu_0 \mu_r \mathbf{H}, \tag{2.1.6}$$

where ε_0 is the permittivity of free-space or the electric constant, $\mathbf{P}$ is the induced polarisation, μ_0 is the vacuum permeability or the magnetic constant, and μ_r is the relative permeability. In glass composites, it is reasonable to assume

$$\rho_f = 0, \tag{2.1.7}$$

$$\mathbf{J}_f = 0, \tag{2.1.8}$$

$$\mu_r = 1, \tag{2.1.9}$$

as glass is non-magnetic and an insulator. Maxwell's equations are then written as

$$\boldsymbol{\nabla} \times \mathbf{E} = -\mu_0 \frac{\partial \mathbf{H}}{\partial t}, \tag{2.1.10}$$

$$\boldsymbol{\nabla} \times \mathbf{H} = \varepsilon_0 \frac{\partial \mathbf{E}}{\partial t} + \frac{\partial \mathbf{P}}{\partial t}, \tag{2.1.11}$$

$$\boldsymbol{\nabla} \cdot \mathbf{D} = 0, \tag{2.1.12}$$

$$\boldsymbol{\nabla} \cdot \mathbf{H} = 0. \tag{2.1.13}$$

Taking the curl of 2.1.10 results in

$$\boldsymbol{\nabla} \times (\boldsymbol{\nabla} \times \mathbf{E}) = -\mu_0 \boldsymbol{\nabla} \times \left(\frac{\partial \mathbf{H}}{\partial t} \right) = -\mu_0 \varepsilon_0 \frac{\partial^2 \mathbf{E}}{\partial t^2} - \mu_0 \frac{\partial^2 \mathbf{P}}{\partial t^2}. \tag{2.1.14}$$

Transforming the equation from the time domain to the frequency domain with a Fourier transformation gives

$$\boldsymbol{\nabla} \times \left(\boldsymbol{\nabla} \times \tilde{\mathbf{E}} \right) = \frac{\omega^2}{c^2} \tilde{\mathbf{E}} + \mu_0 \omega^2 \tilde{\mathbf{P}}, \tag{2.1.15}$$

where ω is the angular frequency of the light and it has been used that the speed of light in vacuum is $c = \frac{1}{\sqrt{\varepsilon_0 \mu_0}}$. The definition of the applied convention of the Fourier transform can be found in App. A.1.1. The tilde emphasises that the variable is the frequency domain version of the variable. It is assumed that it is valid to write

$$\boldsymbol{\nabla} \cdot \tilde{\mathbf{D}} = \varepsilon_0 \varepsilon_r \boldsymbol{\nabla} \cdot \tilde{\mathbf{E}}, \tag{2.1.16}$$

where ε_r is the relative dielectric constant. Eq. 2.1.16 is strictly only valid for a uniform medium. However, for optical fibres, which only consist of regions with doped silica, the spatial variation of the relative dielectric constant, ε_r, is small, which justifies the approximation. With the vector identities, given in App. A.1.1, and the assumption of a uniform medium, the wave-equation is derived from Eq. 2.1.15 and is given by

$$-\boldsymbol{\nabla}^2\tilde{\mathbf{E}} = \frac{\omega^2}{c^2}\tilde{\mathbf{E}} + \mu_0\omega^2\tilde{\mathbf{P}}. \tag{2.1.17}$$

The induced polarisation is expanded in a power series as [31]

$$\tilde{\mathbf{P}} = \sum_{q=1}^{\infty}\tilde{\mathbf{p}}^{(q)}, \tag{2.1.18}$$

where the first order, i.e. linear, contribution to the induced polarisation is $\tilde{\mathbf{p}}^{(1)} = \varepsilon_0\chi^{(1)}\tilde{\mathbf{E}}$. Where $\chi^{(1)}$ is the linear electric susceptibility. Inserting the expanded power series for the induced polarisation into Eq. 2.1.17 gives

$$-\boldsymbol{\nabla}^2\tilde{\mathbf{E}} = \frac{\omega^2}{c^2}\left(1+\chi^{(1)}\right)\tilde{\mathbf{E}} - \mu_0\omega^2\sum_{q=2}^{\infty}\tilde{\mathbf{p}}^{(q)} = \frac{\omega^2}{c^2}\varepsilon_r\tilde{\mathbf{E}} + \mu_0\omega^2\tilde{\mathbf{P}}_{NL}, \tag{2.1.19}$$

where $\tilde{\mathbf{P}}_{NL}$ is the non-linear induced polarisation. The order of the non-linearities is defined as the power of the electric field, $\tilde{\mathbf{E}}$, in the equation. The first non-linear correction to the induced polarisation is due to the second-order electric susceptibility, $\chi^{(2)}$, which is negligible in optical fibres due to the random orientation of the crystalline structure in silica, i.e. silica is an anisotropic material. This makes the third-order electric susceptibility, $\chi^{(3)}$, the most significant non-linear effect in optical fibres. Therefore, the non-linear induced polarisation for the angular frequency of ω_σ is written as

$$\tilde{\mathbf{P}}_{NL} = \frac{3}{4}\varepsilon_0\chi^{(3)}\left(-\omega_\sigma;\omega_j,-\omega_k,\omega_l\right) : \tilde{\mathbf{E}}\left(\omega_j\right)\tilde{\mathbf{E}}^*\left(\omega_k\right)\tilde{\mathbf{E}}\left(\omega_l\right). \tag{2.1.20}$$

The notation for the third order non-linearity follows the one outlined in [32]. The pre-factor of $\frac{3}{4}$ is given with respect to the considered interaction of electric fields and the possible distinct frequency permutations. The non-linear interaction given in Eq. 2.1.20 is responsible for multiple non-linear processes including self-phase modulation (SPM).

2.2 Pulse-Propagation

For most cases it is sufficient to consider a scalar version of the governing equation for pulse-propagation. In the situations where the wave-guide contribution to the dispersion is dominant the full-vectorial equation is needed [33–35]. In the following it is assumed that the electric field in the time domain is polarised in the **x** direction and travelling in the **z** direction

$$\mathbf{E}(\mathbf{r},t) = \frac{1}{2}\mathbf{x}\left\{E(x,y,z,t)\exp\left[-i\omega_0 t\right] + \text{c.c.}\right\}, \tag{2.2.1}$$

where E is the complex electrical amplitude, which is multiplied with a carrier wave and the *c.c.* is the complex conjugate. In the frequency domain, the Fourier transform of $E(x,y,z,t)$ is given as

$$\tilde{E}(x,y,z,\omega) = \tilde{F}(x,y,\omega)\,\tilde{\mathcal{A}}(z,\omega-\omega_0)\exp\left[i\beta(\omega_0)\,z\right], \tag{2.2.2}$$

where it has been assumed that it is possible to separate the amplitude of the electric field into a transverse field distribution $\tilde{F}$, a longitudinal amplitude $\tilde{\mathcal{A}}$, and the spatial part of the carrier wave, where β is the propagation constant. It is now possible to write an equation for the transverse problem and the longitudinal problem using the separation of variables method. The calculation for the separation of variables is performed in App. A.1.2. By using the method of separation of variables two independent homogeneous differential equations are obtained

$$\boldsymbol{\nabla}_\perp^2\tilde{F} + \left(\frac{\omega^2}{c^2}\varepsilon_r - \left(\beta'\right)^2\right)\tilde{F} = 0, \tag{2.2.3}$$

$$\boldsymbol{\nabla}_z^2\tilde{\mathcal{A}} + 2i\beta(\omega_0)\frac{\partial}{\partial z}\tilde{\mathcal{A}} + \left(\left(\beta'\right)^2 - \beta^2(\omega_0)\right)\tilde{\mathcal{A}} = 0. \tag{2.2.4}$$

If only linear induced polarisation effects are considered, then

$$\beta' = \beta = \frac{\omega}{c}n_{eff}, \tag{2.2.5}$$

where n_{eff} is the effective index of the mode in the fibre. In the following the non-linear induced polarisation is considered as a perturbation and the equation is solved to first order of the perturbation. The third order induced polarisation is introduced into the equation as a perturbation to the relative dielectric constant as

$$\varepsilon_r = \varepsilon^0 + \eta\Delta\varepsilon, \tag{2.2.6}$$

where ε^0 is the unperturbed value, $\Delta\varepsilon$ is the perturbation, and $\eta \in [0;1]$, this results in a perturbation of both $\tilde{F}$ and $(\beta')^2$. The perturbation calculation is performed in App. A.1.2. The perturbed propagation-constant square is given as

$$(\beta\prime)^2 = \beta^2 + \Delta\beta^2, \tag{2.2.7}$$

where the first order correction $\Delta\beta^2$ is given as

$$\Delta\beta^2 = \frac{\omega^2}{c^2} \frac{\int_A \Delta\varepsilon \left|\tilde{F}\right|^2 \mathrm{d}A}{\int_A \left|\tilde{F}\right|^2 \mathrm{d}A}. \tag{2.2.8}$$

The non-linear induced polarisation introduces a negligible correction to the transverse problem and therefore the first order perturbation of the transverse problem is disregarded. However, for the longitudinal problem the non-linear induced polarisation has a significant influence.

2.2.1 Generalised Non-Linear Schrödinger Equation

The GNLSE will be derived in this section. In anticipation of expanding the GNLSE to include multiple modes and to include the correct dispersion of the transverse field, the amplitude of the electric field is denoted with a subscript to keep track of different modes. The amplitude of the electric field that experiences a change due to the induced polarisation is denoted with $\tilde{E}_A$ and the amplitudes of the electric fields that take part of the third order non-linear interaction are denoted with $\tilde{E}_B$, $\tilde{E}_C$, and $\tilde{E}_D$. The propagation constant of the carrier wave is denoted β^{ref} to make the choice of reference frame arbitrary. The perturbation $\Delta\varepsilon$ from the previous section is written as

$$\Delta\varepsilon = \frac{\tilde{\mathrm{P}}_{NL}}{\varepsilon_0 \tilde{E}_A}, \tag{2.2.9}$$

where $\tilde{\mathrm{P}}_{NL}$ is the scalar version of the non-linear induced polarisation. With Eq. 2.2.9 $\Delta\beta^2$ is given as

$$\Delta\beta^2 = \frac{\int_A \frac{\chi^{(3)}\left(-\omega_\sigma;\omega_j,\omega_k,\omega_l\right)\tilde{E}_B\left(\omega_j\right)\tilde{E}_C^*\left(\omega_k\right)\tilde{E}_D\left(\omega_l\right)}{\tilde{F}_A \exp\left[i\beta^{\mathrm{ref}}\left(\omega_0\right)z\right]} \left|\tilde{F}_A\right|^2 \mathrm{d}A}{\int_A \left|\tilde{F}_A\right|^2 \mathrm{d}A} \times \frac{3}{4}\frac{\omega_\sigma^2}{c^2}\frac{1}{\tilde{\mathcal{A}}_A}. \tag{2.2.10}$$

The strength of the non-linear interaction is rewritten in terms of the intensity-dependent refractive index, which is related to the SPM effect. With the introduction of the intensity-dependent refractive index the pre-factor of $\frac{3}{4}$ is cancelled and the intensity-dependent refractive index is assumed fundamental for any of the non-linear processes, which take place in the fibre. The occurrence of distinct permutations for the different non-linear interactions is handled by summing all the distinct permutations together. For the SPM effect, it is possible to translate the third-order electric susceptibility, $\chi^{(3)}$, to an intensity-dependent refractive index [9]

$$\chi^{(3)} = \frac{4}{3} n_{eff}^2 \varepsilon_0 c n_2^I. \tag{2.2.11}$$

To be able to account for the frequency dependence of the non-linear response of a given material, a response function, $\tilde{R}$, is multiplied with the intensity-dependent refractive index, n_2^I. Hereby, Eq. 2.2.10 is given as

$$\begin{aligned}\Delta\beta^2 =& \frac{\int_A \tilde{R}\left(-\omega_\sigma;\omega_j,\omega_k,\omega_l\right)\tilde{E}_B\left(\omega_j\right)\tilde{E}_C^*\left(\omega_k\right)\tilde{E}_D\left(\omega_l\right)\tilde{F}_A^*\mathrm{d}A}{\int_A\left|\tilde{F}_A\right|^2\mathrm{d}A} \\ &\times\frac{\omega_\sigma^2 n_{eff,A}^2\varepsilon_0 n_2^I}{c}\exp\left[i\beta^{\mathrm{ref}}\left(\omega_0\right)z\right]\frac{1}{\tilde{\mathcal{A}}_A}.\end{aligned} \tag{2.2.12}$$

By inserting Eq. 2.2.12 into Eq. 2.2.4 the following differential equation for the longitudinal amplitude is obtained

$$\begin{aligned}&\boldsymbol{\nabla}_z^2\tilde{\mathcal{A}}_A - 2i\beta^{\mathrm{ref}}\left(\omega_0\right)\frac{\partial}{\partial z}\tilde{\mathcal{A}}_A + \left(\beta_A^2 - \left(\beta^{\mathrm{ref}}\left(\omega_0\right)\right)^2\right)\tilde{\mathcal{A}}_A = \\ &-\frac{\int_A \tilde{R}\left(-\omega_\sigma;\omega_j,\omega_k,\omega_l\right)\tilde{E}_B\left(\omega_j\right)\tilde{E}_C^*\left(\omega_k\right)\tilde{E}_D\left(\omega_l\right)\tilde{F}_A^*\mathrm{d}A}{\int_A\left|\tilde{F}_A\right|^2\mathrm{d}A} \\ &\times\frac{\omega_\sigma^2 n_{eff,A}^2\varepsilon_0 n_2^I}{c}\exp\left[-i\beta^{\mathrm{ref}}\left(\omega_0\right)z\right].\end{aligned} \tag{2.2.13}$$

For convenience the unit of the complex longitudinal amplitude $\tilde{\mathcal{A}}$ is converted to the unit of $\sqrt{\mathrm{W}}$. The conversion is done in App. A.1.2. $\tilde{\mathcal{A}}$ is replaced with the following expression

$$\tilde{\mathcal{A}} = \frac{\tilde{A}}{\sqrt{\frac{1}{2}c\varepsilon_0 n_{eff}\int\left|\tilde{F}\right|^2\mathrm{d}x\mathrm{d}y}}, \tag{2.2.14}$$

where $\tilde{A}$ is the new variable with the unit of $\sqrt{W}$. The right-hand side (RHS) of Eq. 2.2.13 is treated as an operator working on a vector as $\hat{\Pi}\tilde{A}$, where $\hat{\Pi}$ is the operator, this is the same approach as applied in [36]

$$\boldsymbol{\nabla}_z^2 \tilde{A}_A + 2i\beta^{\mathrm{ref}}(\omega_0)\frac{\partial}{\partial z}\tilde{A}_A + \left(\beta_A^2 - \left(\beta^{\mathrm{ref}}(\omega_0)\right)^2\right)\tilde{A}_A = \hat{\Pi}\tilde{A}_A. \tag{2.2.15}$$

The operator-vector product is given as

$$\begin{aligned}\hat{\Pi}\tilde{A}_A = &-\frac{\int_A \tilde{R}(-\omega_\sigma;\omega_j,\omega_k,\omega_l)\,\tilde{E}_B(\omega_j)\,\tilde{E}_C^*(\omega_k)\,\tilde{E}_D(\omega_l)\,\tilde{F}_A^*\mathrm{d}A}{\int_A \left|\tilde{F}_A\right|^2 \mathrm{d}A} \\ &\times \frac{\omega_\sigma^2 n_{eff,A}^2 \varepsilon_0 n_2^I}{c}\exp\left[-i\beta^{\mathrm{ref}}(\omega_0)\,z\right] \qquad (2.2.16) \\ &\times \frac{\sqrt{n_{eff,A}\int_A \left|\tilde{F}_A\right|^2 \mathrm{d}A}}{\sqrt{n_{eff,B}\int_A \left|\tilde{F}_B\right|^2 \mathrm{d}A}\sqrt{n_{eff,C}\int_A \left|\tilde{F}_C\right|^2 \mathrm{d}A}\sqrt{n_{eff,D}\int_A \left|\tilde{F}_D\right|^2 \mathrm{d}A}} \\ &= -\frac{2\omega_\sigma^2 n_{eff,A} n_2^I}{c^2}\tilde{q}_{A,B,C,D}. \qquad (2.2.17)\end{aligned}$$

For a silica-based fibre it is assumed that the effective indices of the different modes are approximately the same, which is true if the indices are compared at the same frequency. The $\tilde{q}_{A,B,C,D}$ factor is given as

$$\begin{aligned}\tilde{q}_{A,B,C,D} = &\frac{\int_A \tilde{F}_B \tilde{F}_C^* \tilde{F}_D \tilde{F}_A^* \mathrm{d}A}{\sqrt{\int_A \left|\tilde{F}_B\right|^2 \mathrm{d}A}\sqrt{\int_A \left|\tilde{F}_C\right|^2 \mathrm{d}A}\sqrt{\int_A \left|\tilde{F}_D\right|^2 \mathrm{d}A}\sqrt{\int_A \left|\tilde{F}_A\right|^2 \mathrm{d}A}} \\ &\times \tilde{R}(-\omega_\sigma;\omega_j,\omega_k,\omega_l)\,\tilde{A}_B \tilde{A}_C^* \tilde{A}_D, \qquad (2.2.18)\end{aligned}$$

where the fraction on the RHS is the field overlap, which is the inverse of the effective area. With the definition of the operator $\hat{\Pi}$ it is possible to factor 2.2.15 into

$$\left(i\frac{\partial}{\partial z} - \beta^{\mathrm{ref}}(\omega_0) + \sqrt{\beta_A^2 + \hat{\Pi}}\right)\left(i\frac{\partial}{\partial z} - \beta^{\mathrm{ref}}(\omega_0) - \sqrt{\beta_A^2 + \hat{\Pi}}\right)\tilde{A}_A = 0 \tag{2.2.19}$$

The first and the second parentheses are equivalent to a forward propagating wave and a backward propagating wave, respectively. By neglecting the backward propagating wave and expanding the square-root to a first order expansion under the assumption that the non-linear contribution to the propagation constants, i.e. $\left|\frac{\hat{\Pi}\tilde{A}_A}{\beta_A^2\tilde{A}_A}\right| << 1$ then[1]

$$\left(\frac{\partial}{\partial z} - i\left(\beta_A - \beta^{\mathrm{ref}}(\omega_0)\right)\right)\tilde{A}_A = -i\frac{\hat{\Pi}}{2\beta_A}\tilde{A}_A = i\frac{\omega_\sigma n_2^I}{c}\tilde{q}_{A,B,C,D}. \tag{2.2.20}$$

The coordinate system for the pulse propagation is translated into a moving time-frame. Introducing a moving frame $T = t - \frac{z}{v_g^{\mathrm{ref}}} = t - \beta_1^{\mathrm{ref}} z$ and $x = z$ changes the derivatives. In the moving time frame the temporal and spatial coordinates are redefined as t and z, respectively. The coordinate transformation is performed in App. A.1.2. Eq. 2.2.20 is then given as

$$\left(\frac{\partial}{\partial z} - i\left(\beta_A - \beta^{\mathrm{ref}}(\omega_0) - \beta_1^{\mathrm{ref}}(\omega_0)(\omega_\sigma - \omega_0)\right)\right)\tilde{A}_A = i\frac{\omega_\sigma n_2^I}{c}\tilde{q}_{A,B,C,D}. \tag{2.2.21}$$

Eq. 2.2.21 is valid for the frequency combination of the electric amplitudes E_B, E_C, and E_D that add to the frequency of the electric amplitude E_A, this is given as $\omega_\sigma = \omega_j + \omega_k + \omega_l$. Therefore, to account for all the possible frequency combinations, which yields a sum frequency of ω_σ, a double frequency integration is performed over $\tilde{q}_{A,B,C,D}$ in Eq. 2.2.21

$$\left(\frac{\partial}{\partial z} - i\left(\beta_A - \beta^{\mathrm{ref}}(\omega_0) - \beta_1^{\mathrm{ref}}(\omega_0)(\omega_\sigma - \omega_0)\right)\right)\tilde{A}_A = i\frac{\omega_\sigma n_2^I}{c}\int_{\omega_1}\int_{\omega_2}\tilde{q}_{A,B,C,D}\mathrm{d}\omega_2\mathrm{d}\omega_1. \tag{2.2.22}$$

The frequency dependence of n_2^I is neglected [37]. The double frequency integration over $\tilde{q}_{A,B,C,D}$ is performed in App. A.1.2. For the GNLSE the frequency dependence of the transverse fields of the different electric amplitudes is disregarded and this enables the RHS of Eq. 2.2.22 to be

[1] Another way to obtain this result is to use the slowly varying envelope approximation.

written as

$$i\frac{\omega_\sigma n_2^I}{c}\int_{\omega_1}\int_{\omega_2}\tilde{q}_{A,B,C,D}\mathrm{d}\omega_2\mathrm{d}\omega_1 = i\frac{\omega_\sigma n_2^I}{cA_{eff,A,B,C,D}} \times \mathcal{F}\left\{\mathcal{F}^{-1}\left\{\tilde{A}_B\right\}\mathcal{F}^{-1}\left\{\tilde{R}\mathcal{F}\left\{\mathcal{F}^{-1}\left\{\tilde{A}_C^*\right\}\mathcal{F}^{-1}\left\{\tilde{A}_D\right\}\right\}\right\}\right\}, \quad (2.2.23)$$

where A_{eff} is the effective transverse-mode-area, $\mathcal{F}$ denotes the Fourier transform from the time domain to the frequency domain, and $\mathcal{F}^{-1}$ denotes the inverse Fourier transform. The GNLSE is then given as

$$\frac{\partial\tilde{A}_A}{\partial z} = i\left(\beta_A - \beta^{\mathrm{ref}}(\omega_0) - \beta_1^{\mathrm{ref}}(\omega_0)(\omega_\sigma - \omega_0)\right)\tilde{A}_A + i\frac{\omega_\sigma n_2^I}{cA_{eff,A,B,C,D}} \times \mathcal{F}\left\{\mathcal{F}^{-1}\left\{\tilde{A}_B\right\}\mathcal{F}^{-1}\left\{\tilde{R}\mathcal{F}\left\{\mathcal{F}^{-1}\left\{\tilde{A}_C^*\right\}\mathcal{F}^{-1}\left\{\tilde{A}_D\right\}\right\}\right\}\right\}. \quad (2.2.24)$$

The dispersion of the transverse field of the different electric fields, which is involved in the non-linear interaction, has been disregarded. In [38] a simple correction to Eq. 2.2.24 is presented to approximate the dispersion of the transverse field with a first-order correction. Using the correction from [38] the GNLSE is the given as

$$\begin{aligned}\frac{\partial\tilde{A}_A}{\partial z} =& -\frac{\alpha_A}{2}\tilde{A}_A + i\left(\beta_A - \beta^{\mathrm{ref}}(\omega_0) - \beta_1^{\mathrm{ref}}(\omega_0)(\omega_\sigma - \omega_0)\right)\tilde{A}_A \\ &+ i\frac{\omega_\sigma n_2^I}{c\sqrt[4]{A_{eff,A,B,C,D}}}\mathcal{F}\left\{\mathcal{F}^{-1}\left\{\tilde{G}_B\right\}\mathcal{F}^{-1}\left\{\tilde{R}\mathcal{F}\left\{\mathcal{F}^{-1}\left\{\tilde{G}_C^*\right\}\right.\right.\right. \\ &\times\ \left.\left.\left.\mathcal{F}^{-1}\left\{\tilde{G}_D\right\}\right\}\right\}\right\}, \end{aligned} \quad (2.2.25)$$

where $\tilde{G} = \frac{\tilde{A}}{\sqrt[4]{A_{eff,A,B,C,D}}}$ and α is the power-loss coefficient, which also is introduced. Therefore, the GNLSE for an intramodal interaction is written as

$$\begin{aligned}\frac{\partial\tilde{A}}{\partial z} =& -\frac{\alpha}{2}\tilde{A} + i\left(\beta - \beta^{\mathrm{ref}}(\omega_0) - \beta_1^{\mathrm{ref}}(\omega_0)(\omega_\sigma - \omega_0)\right)\tilde{A} \\ &+ i\frac{\omega_\sigma n_2^I}{c\sqrt[4]{A_{eff}}}\mathcal{F}\left\{\mathcal{F}^{-1}\left\{\tilde{G}\right\}\mathcal{F}^{-1}\left\{\tilde{R}\left|\tilde{G}\right|^2\right\}\right\}, \end{aligned} \quad (2.2.26)$$

where Parseval's theorem has been applied. The conserved quantity can be shown to be proportional to the photon number by using the same method as outlined in [36].

The third-order non-linearity response function, R, is commonly modelled as a sum of an electronic response, a vibrational/rotational response, and an acoustic response. For silica the electronic response is on the order of a few femtoseconds, the vibrational/rotational response is on the order of a few hundreds of femtoseconds, and the acoustic response is on the order of a few nanoseconds. When considering pulses with a temporal duration in the sub-nanosecond range the response function is often modelled as

$$R(t) = (1 - f_R)\,\delta(t) + f_R h_R(t), \tag{2.2.27}$$

where $h_R(t)$ is the Raman-response function, the delta function represents the instantaneous electronic response, and f_R is the Raman fraction of the intensity-dependent refractive index. The Raman response function in silica is often modelled as a damped oscillator [36], however, more complex models exist [39,40]. The Raman fraction, f_R, for a pure silica-core fibre is reported to be 0.18 [41]. With the assumption about the response function, the GNLSE is written as

$$\begin{aligned}\frac{\partial \tilde{A}}{\partial z} =& -\frac{\alpha}{2}\tilde{A} + i\left(\beta - \beta^{\mathrm{ref}}(\omega_0) - \beta_1^{\mathrm{ref}}(\omega_0)(\omega_\sigma - \omega_0)\right)\tilde{A} \\ &+ i\frac{\omega_\sigma n_2^I}{c\sqrt[4]{A_{eff}}}\mathcal{F}\left\{(1 - f_R)|G|^2 G + f_R\mathcal{F}^{-1}\left\{\tilde{h}_R\left|\tilde{G}\right|^2\right\}G\right\}.\end{aligned} \tag{2.2.28}$$

Numerically the GNLSE is solved efficiently with the Fourth-Order Runge-Kutta in the Interaction-Picture (RK4IP) method [42].

Soliton Solution

A special solution to the Non-Linear Schrödinger Equation (NLSE) and therefore also the GNLSE is the soliton solution. The soliton solution occurs under the right circumstances, when the accumulated non-linear phase-shift is balanced by the anomalous dispersion. In the simple case of the NLSE the soliton solution is an attractive fixed point for the injected pulses. The soliton pulse solution is characterised by a $\mathrm{sech}^2\left(\frac{t}{T_0}\right)$ intensity profile and the peak power of the soliton pulse is given by [9]

$$P_p = \frac{N^2\,|\beta_2|\,cA_{eff}}{\omega n_2^I T_0^2}, \tag{2.2.29}$$

where N is the order of the soliton, β_2 is the group-velocity dispersion. For a soliton in the sub-picosecond range the shorter wavelength components act as a Raman amplifier for the longer wavelength components in an intra-pulse Raman scattering process. This shifts the soliton towards longer wavelengths, which is also known as the soliton self-frequency shift (SSFS). The soliton solution was first observed numerically [43, 44] and later experimentally [25]. The theory and an analytical solution for the SSFS were first presented in [26]. The equation for the centre frequency of the soliton as a result of SSFS is given as [40]

$$\frac{\partial\bar{\omega}}{\partial z} = -\frac{2P_p}{\pi^2 A_{eff}} \int_0^\infty \frac{g_r\left(\Omega\right)\left(\frac{\Omega\pi T_0}{2}\right)^3}{\sinh^2\left(\frac{\Omega\pi T_0}{2}\right)} \mathrm{d}\Omega, \tag{2.2.30}$$

where g_r is the Raman gain. With the model for the response function given in Eq 2.2.27, it is possible to rewrite Eq. 2.2.30 as

$$\frac{\partial\bar{\omega}}{\partial z} = -4\frac{\left|\beta_2\right| f_r}{\pi^2\left(T_0\right)^2} \int_0^\infty \frac{\Im\left\{\tilde{h}_R\left(\Omega\right)\right\}\left(\frac{\Omega\pi T_0}{2}\right)^3}{\sinh^2\left(\frac{\Omega\pi T_0}{2}\right)} \mathrm{d}\Omega, \tag{2.2.31}$$

where $\Im$ denotes the imaginary part. If the Raman response function is assumed approximately the same for all silica-based fibres, the magnitude of the SSFS is determined by the temporal duration of the pulse, the group velocity dispersion, and the Raman fraction. In Chap. 3 the intensity-dependent refractive index and the Raman contribution to the intensity-dependent refractive index is measured for a couple of simple step-index fibres with a germanium-doped core. The Raman fraction, f_R, is determined to be smaller than 0.18 as reported for a fibre with a pure silica-core [41].

2.2.2 Multi-Mode Generalised Non-Linear Schrödinger Equation

The multi-mode (MM) GNLSE in this work is based on the Eq. 2.2.25. This is similar to the framework of [45, 46], but in this section the dispersion of the transverse field is included with the fourth-order root method [38]. For an interaction with two different modes the equations

for the pulse propagation are given as

$$\begin{aligned}\frac{\partial \tilde{A}_A}{\partial z} =& -\frac{\alpha_A}{2}\tilde{A}_A + i\left(\beta_A - \beta^{\mathrm{ref}}(\omega_0) - \beta_1^{\mathrm{ref}}(\omega_0)(\omega_\sigma - \omega_0)\right)\tilde{A}_A \\ &+ \tilde{Q}_{A,A,A,A} + \tilde{Q}_{A,B,A,A} + \tilde{Q}_{A,A,B,A} + \tilde{Q}_{A,A,A,B} \\ &+ \tilde{Q}_{A,B,B,A} + \tilde{Q}_{A,B,A,B} + \tilde{Q}_{A,A,B,B} + \tilde{Q}_{A,B,B,B}, \qquad (2.2.32)\\ \frac{\partial \tilde{A}_B}{\partial z} =& -\frac{\alpha_B}{2}\tilde{A}_B + i\left(\beta_B - \beta^{\mathrm{ref}}(\omega_0) - \beta_1^{\mathrm{ref}}(\omega_0)(\omega_\sigma - \omega_0)\right)\tilde{A}_B \\ &+ \tilde{Q}_{B,B,B,B} + \tilde{Q}_{B,A,B,B} + \tilde{Q}_{B,B,A,B} + \tilde{Q}_{B,B,B,A} \\ &+ \tilde{Q}_{B,A,A,B} + \tilde{Q}_{B,A,B,A} + \tilde{Q}_{B,B,A,A} + \tilde{Q}_{B,A,A,A}, \qquad (2.2.33)\end{aligned}$$

where $\tilde{Q}_{A,B,C,D}$ is given as Eq. 2.2.23 with the fourth root method, which is written as

$$\begin{aligned}\tilde{Q}_{A,B,C,D} =& i\frac{\omega_\sigma n_2^I}{c\sqrt[4]{A_{eff,A,B,C,D}}}\mathcal{F}\left\{\mathcal{F}^{-1}\left\{\tilde{G}_B\right\}\mathcal{F}^{-1}\left\{\tilde{R}\right.\right. \\ &\left.\left.\times\mathcal{F}\left\{\mathcal{F}^{-1}\left\{\tilde{G}_C^*\right\}\mathcal{F}^{-1}\left\{\tilde{G}_D\right\}\right\}\right\}\right\}. \qquad (2.2.34)\end{aligned}$$

$\tilde{Q}_{A,B,C,D}$ represents the non-linear interaction for the given modal combination. For some modal combinations, $\tilde{Q}_{A,B,C,D}$ yields a zero value and can be disregarded. If the considered non-linear interaction is between one $\mathrm{LP}_{1,1}$ mode and three $\mathrm{LP}_{0,1}$ modes, then a difference in angular symmetry will yield a zero non-linear interaction. However, if the interaction is between one $\mathrm{LP}_{0,2}$ mode and three $\mathrm{LP}_{0,1}$ modes, the non-linear interaction will yield a non-zero value. More insight into symmetry overlap of the interacting modes is given in [45]. For the MM GNLSE the conserved quantity is proportional to the sum of the photon number for the different modes.

2.2.3 Transverse-Field Dispersion in the Generalised Non-Linear Schrödinger Equation

It was found that to accurately simulate the intermodal non-linear interaction in one of the few-moded fibres (FMFs) fabricated and used in this work the MM GNLSE failed to reproduce the experimentally obtained results. The failure of the MM GNLSE is caused by dispersion of the transverse field. In the GNLSE the dispersion of the transverse field is incorporated with the effect area parameter. Therefore, the GNLSE was re-derived from Maxwell's equations to include

the correct dispersion of the transverse field. The new version of the GNLSE is denoted the Transverse-Field Dispersion in the Generalised Non-Linear Schrödinger Equation (TFD-GNLSE). The derivation of the TFD-GNLSE follows the derivation for the GNLSE up to and including Eq. 2.2.22. The double frequency integration over $\tilde{q}_{A,B,C,D}$ in Eq. 2.2.22 is carried out in App. A.1.2. For the TFD-GNLSE the frequency dependence of the transverse fields of the different electric amplitudes is included and therefore the RHS of Eq. 2.2.22 is written as

$$\tilde{Q}_{A,B,C,D} = \int_{\omega_1}\int_{\omega_2} \tilde{q}_{A,B,C,D}\mathrm{d}\omega_2\mathrm{d}\omega_1 = i\frac{\omega_\sigma n_2^I}{c}\int_A \tilde{F}_{N,A}^* \times \mathcal{F}\left\{\mathcal{F}^{-1}\left\{\tilde{G}_B\right\}\mathcal{F}^{-1}\left\{\tilde{R}\mathcal{F}\left\{\mathcal{F}^{-1}\left\{\tilde{G}_C^*\right\}\mathcal{F}^{-1}\left\{\tilde{G}_D\right\}\right\}\right\}\right\}\mathrm{d}A, \quad (2.2.35)$$

where $\tilde{G} = \tilde{A}\tilde{F}_N$ and $\tilde{F}_N$ is the normalised transverse field, where the normalisation is

$$\tilde{F}_N = \frac{\tilde{F}}{\sqrt{\int_A \left|\tilde{F}\right|^2 \mathrm{d}A}}. \quad (2.2.36)$$

Numerical Considerations

In order to incorporate the correct dispersion of the transverse fields, the integration over the transverse area has to be carried out after the calculation of the double frequency integral, which is rewritten as a couple of Fourier transforms. As the integration over the transverse area is performed after the set of Fourier transforms, it implies that the numerically load increases significantly with respect to the GNLSE, since the number of applied sets of Fourier transform scales with the number of grid points for the transverse field distribution. This emphasises the significance of the fourth root method to approximate dispersion of the transverse field in [38], as the numerical computational load is unchanged with this method. To reduce the numerical computation load, it is advantageous to utilise that the fibres considered in this project have a radial symmetric refractive index profile and to solve the transverse problem in cylindrical coordinates. This reduces the numerical computational load, however, depending on the number of grid points in the radial direction the computational load may still be significant. To reduce the number of radial grid points used, a Gaussian quadrature rule is applied to compute the transverse field overlap. This approach is

similar to the one presented in [47], however in [47] it was only the fundamental mode that was considered and the result showed only a small discrepancy between the modified GNLSE and unmodified GNLSE.

The set of basic equations presented for the MM GNLSE in Sec. 2.2.2 is also valid for the TFD-GNLSE if $\tilde{Q}_{A,B,C,D}$ is replaced with the expression in Eq. 2.2.35.

In App. A.1.2 a verification of the numerical implementation of the TFD-GNLSE is performed. The verification is performed for a case of an intramodal non-linear interaction, where a SSFS takes place. The verification shows an excellent agreement between the TFD-GNLSE and the GNLSE.

2.3 Modesolver

The work in this section is based upon [48]. The modesolver used in this project is based on a full vectorial implementation of Maxwell's equations for a cylindrical fibre with a radial symmetric index profile. The modesolver solves for the $\tilde{\mathbf{H}}$ field and the equations for the radial, ρ, and the angular, θ, component is given as

$$\begin{aligned}\frac{\partial^2 \tilde{H}_\rho(\rho)}{\partial\rho^2} + \frac{1}{\rho}\frac{\partial \tilde{H}_\rho(\rho)}{\partial\rho} - \frac{m^2}{\rho^2}\tilde{H}_\rho(\rho) - \frac{1}{\rho^2}\tilde{H}_\rho(\rho) \\ + \frac{2m}{\rho^2}\tilde{H}_\theta(\rho) + \varepsilon_r(\rho)\, k_0^2 \tilde{H}_\rho(\rho) = \beta^2 \tilde{H}_\rho(\rho),\end{aligned} \tag{2.3.1}$$

$$\begin{aligned}\frac{\partial^2 \tilde{H}_\theta(\rho)}{\partial\rho^2} + \frac{1}{\rho}\frac{\partial \tilde{H}_\theta(\rho)}{\partial\rho} - \frac{m^2}{\rho^2}\tilde{H}_\theta(\rho) - \frac{1}{\rho^2}\tilde{H}_\theta(\rho) \\ + \frac{2m}{\rho^2}\tilde{H}_\rho(\rho) + \varepsilon_r(\rho)\, k_0^2 \tilde{H}_\theta(\rho) \\ + \frac{1}{\varepsilon_r(\rho)}\frac{\partial \varepsilon_r(\rho)}{\partial\rho}\left[-\frac{\partial \tilde{H}_\theta(\rho)}{\partial\rho} - \frac{1}{\rho}\tilde{H}_\theta(\rho) + \frac{m}{\rho}\tilde{H}_\rho(\rho)\right] = \beta^2 \tilde{H}_\theta(\rho),\end{aligned} \tag{2.3.2}$$

where ρ is the radial coordinate, θ is the angular coordinate, m is the angular eigenvalue and k_0 is the wave-vector in vacuum. It is seen that the radial, ρ, and the angular, θ, components are decoupled from the longitudinal, z, component, so it is possible to solve for these components separately. In order to obtain the full solution it is also necessary

to determine the longitudinal, z, component. This can be done by using that the magnetising field, $\tilde{\mathbf{H}}$, is divergence free

$$\tilde{H}_z = \frac{-i}{\beta}\left[\frac{1}{\rho}\tilde{H}_\rho + \frac{\partial \tilde{H}_\rho}{\partial \rho} - \frac{m}{\rho}\tilde{H}_\theta\right]. \tag{2.3.3}$$

In order to keep the complexity of the pulse propagation to a minimum and thereby also not increasing the required numerical computational load, the modes are treated as scalar modes, but with the dispersive properties from the full vectorial modesolver. For the symmetric $\mathrm{LP}_{0,x}$ modes the approximation is reasonable, as the two transverse components are identical.

Chapter 3

Non-Linearity in Optical Fibres

The work in this section is based upon [49]. Over the years determination of the intensity-dependent refractive index has received significant attention [37, 50–54]. However, only a few of the reported works have tried to take into account the Raman fraction of the intensity-dependent refractive index [41, 55, 56]. For a pure silica core fibre the Raman fraction, f_R, of the intensity-dependent refractive index is reported to be 0.18 [41]. This value is often used in pulse propagation in other silica-based fibres. However, this is questionable as the different dopants influence the Raman fraction. For numerically modelling of the soliton self-frequency shift (SSFS), one of the important parameters is the Raman fraction, f_R, of the intensity-dependent refractive index, see Eq. 2.2.31. In this chapter the measured intensity-dependent refractive index is presented for a couple of simple step-index fibres. The core of the fibres is doped with germanium and the cladding consists of pure silica. The measured Raman gain for the fibres is presented together with the complex Raman index of refraction, where the imaginary part of the complex index is related to absorption and gain. The real and imaginary parts of the complex index are connected through the Kramers-Krönig relations. From the Kramers-Krönig relations the real part of the complex Raman index of refraction is obtained. The value at zero detuning of the real part of the complex Raman index of refraction is the Raman process contribution to the self-phase modulation (SPM). SPM is directly related to the intensity-dependent refractive index. Therefore, it is possible from the measured intensity-dependent refractive index and

the Raman gain to calculate the Raman fraction, f_R, to the intensity-dependent refractive index. The choice of only considering simple step-index fibres with a core of germanium is to avoid contributions from other dopant materials such as fluorine and phosphor to the intensity-dependent refractive index. The parameters for the different step-index fibres are given in Table 3.1.

	Core radius [μm]	Δn $[\times 10^{-3}]$
Fibre 1	2.0	8
Fibre 2	2.2	21
Fibre 3	1.4	23
Fibre 4	1.6	30
Fibre 5	2.1	31

Table 3.1: An overview of the different step-index fibres with a germanium-doped core and pure silica-cladding. The index difference between the core and cladding is measured at a wavelength of 632.8 nm.

3.1 Intensity-Dependent Refractive Index

The intensity-dependent refractive index of the germanium-doped step-index fibres is measured with a SPM based technique, where the non-linear phase is retrieved from the ratio of the peak intensity of the SPM main peak and first-side bands [52]

$$\frac{I_0}{I_1} = \frac{J_0^2\left((\frac{\phi_{\text{spm}}}{2}\right) + J_1^2\left((\frac{\phi_{\text{spm}}}{2}\right)}{J_1^2\left((\frac{\phi_{\text{spm}}}{2}\right) + J_2^2\left((\frac{\phi_{\text{spm}}}{2}\right)}, \quad \text{where} \quad \frac{\phi_{\text{spm}}}{2} = \frac{2\omega_0}{c}\frac{n_2^I}{A_{\text{eff}}}L_{\text{eff}}\bar{P}. \tag{3.1.1}$$

The effective area, A_{eff}, is calculated from the measured refractive index profile of the different fibres. A sketch of the setup is seen in Fig. 3.1. The frequency separation of the two polarisation-maintaining (PM) continuous-wave (CW) distributed-feedback (DFB) lasers is 0.2 nm, which corresponds to a 50 GHz modulation, this means that stimulated-Brillouin scattering (SBS) is prevented. To avoid dispersion effects in the measurement the following inequality has to be fulfilled

$$\Delta\phi_{\text{spm}}\beta_2\Delta\omega_0^2 L << 1. \tag{3.1.2}$$

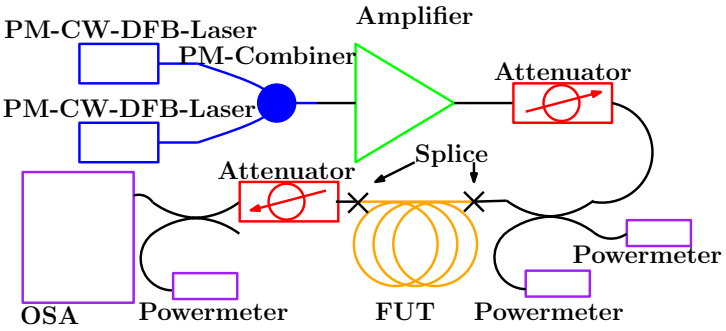

Figure 3.1: Sketch of the SPM-based setup.

This limits the possible length of the fibre-under-test (FUT). However, the problem resides in knowing, which length of a fibre will satisfy the inequality. The length of the fibres used in the measurements is 200 m. An example of the measured SPM spectrum for a varying optical input power is shown in Fig. 3.2. The two PM CW DFB are adjusted to have the same peak power and the SPM sidebands are clearly shown. Using

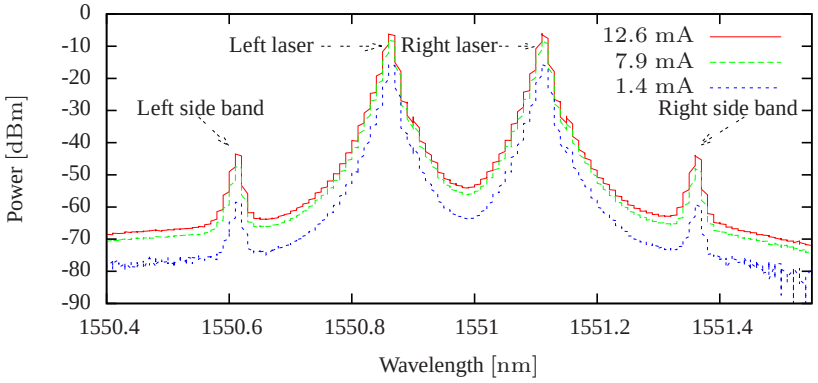

Figure 3.2: Example of a SPM measurement showing the spectrum for three different input powers.

Eq. 3.1.1 it is possible to obtain the non-linear phase as a function of the optical input power, an example is shown in Fig. 3.3. Both the left and right sides of the spectrum are used to retrieve the non-linear phase change as a function of the optical input power. The linear fits are fitted such that they both have the same slope but a different intersection

with the y-axis. In Fig. 3.4 the retrieved intensity-dependent refractive

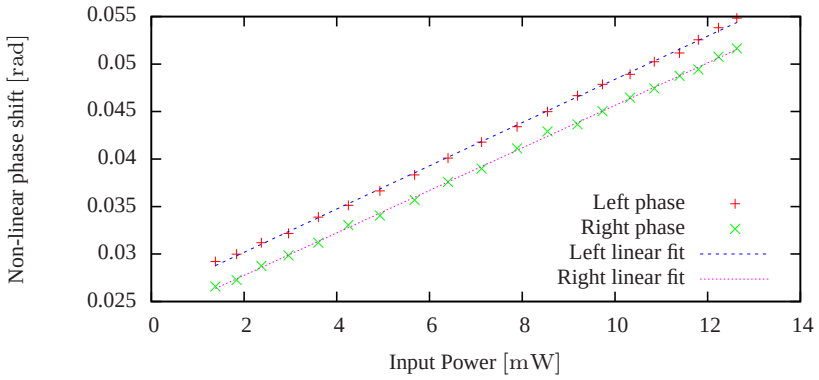

Figure 3.3: Example of the retrieved non-linear phase shift.

index for the considered step-index fibres is shown as a function of the weighted germanium concentration. The weighted germanium concentration is introduced to account for the varying intensity distribution across the core region for the different fibres. The weighted germanium concentration is given as

$$C_{ge} = \frac{\int_{\theta=0}^{2\pi}\int_{r=0}^{\infty} x_{ge}\left(\left|\tilde{F}\right|^2\right)^2 r\mathrm{d}r\mathrm{d}\theta}{\int_{\theta=0}^{2\pi}\int_{r=0}^{\infty}\left(\left|\tilde{F}\right|^2\right)^2 r\mathrm{d}r\mathrm{d}\theta}, \tag{3.1.3}$$

where r is the radial coordinate, θ is the angular coordinate, $\tilde{F}$ is the transverse field distribution of the electric field, and x_{ge} is the molar germanium concentration at a given point. From [57] the germanium concentration is related to the index of refraction at a given radial point. The weighted germanium concentration is calculated using the measured index profile of the different fibres. By performing a linear regression of the data points, the following expression for the intensity-dependent refractive index is obtained

$$n_2^I\left(C_{ge}\right) = 0.0340 \times 10^{-20}\frac{\mathrm{m}^2}{\mathrm{mol}\,\%\,\mathrm{W}}\,C_{ge} + 2.18 \times 10^{-20}\frac{\mathrm{m}^2}{\mathrm{W}} \tag{3.1.4}$$

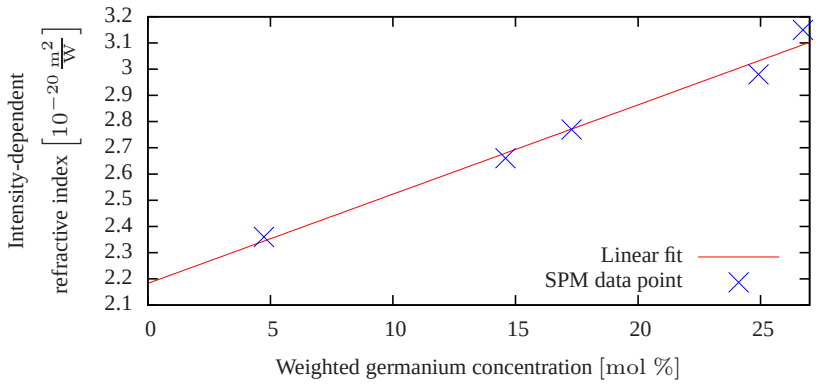

Figure 3.4: The intensity-dependent refractive index from both the electronic and vibrational/rotational contribution is plotted as a function of the weighted germanium concentration.

3.2 Complex Raman Index of Refraction

The Raman gain of the germanium doped step-index fibres is measured with an on/off gain measurement. The contribution from the Raman effects to the intensity-dependent refractive index is calculated from the measured Raman gain. The Raman gain is related to the imaginary part of the complex Raman index of refraction. The third-order non-linear effect, which causes the Raman amplification, can be written as an effective first-order effect, which is dependent on the Raman pump intensity. Therefore, is it valid to apply the Kramers-Krönig relations to the Raman effect. From the real part of the complex Raman index of refraction the Raman contribution to the intensity-dependent refractive index is obtained [41]. The complex Raman index of refraction is written as

$$n_{2,R}^{\dagger} = n_{2,R}^{I} + i\kappa_{2,R}^{I}, \tag{3.2.1}$$

where the $n_{2,R}^{I}$ is the real part of the complex Raman refractive index, i is the imaginary unit, and $\kappa_{2,R}^{I}$ is the imaginary part of the complex Raman refractive index. The Raman gain coefficient is given as

$$g_R = -2\frac{2\pi}{\lambda}\frac{\kappa_{2,R}^{I}}{A_{eff,R}}, \tag{3.2.2}$$

where $A_{eff,R}$ is the effective area of the Raman process, which takes the wavelength dependence of the field overlap between the pump and the

signal into consideration [58]. The effective Raman area is calculated from the measured index profile of the different fibres. The Kramers-Krönig relations for the complex Raman refractive index are given as [59]

$$n_{2,R}^{I}(\nu) = 1 - \frac{1}{\pi\nu}\text{p.v.}\int_{-\infty}^{\infty}\frac{\nu'\kappa_{2,R}^{I}(\nu')}{\nu'-\nu}\mathrm{d}\nu' \tag{3.2.3}$$

$$\kappa_{2,R}^{I}(\nu) = \frac{1}{\pi\nu}\text{p.v.}\int_{-\infty}^{\infty}\frac{\nu'\left(n_{2,R}^{I}(\nu')-1\right)}{\nu'-\nu}\mathrm{d}\nu', \tag{3.2.4}$$

where p.v. is the principal value of the integral, and ν is the frequency. From the Raman gain the imaginary part of the complex Raman refractive index is obtained and using the Kramers-Krönig relations the real part of the complex Raman refractive index is calculated. The setup for

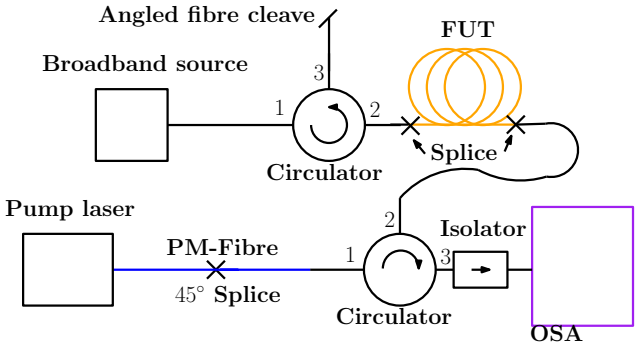

Figure 3.5: Sketch of the setup for the Raman gain measurement.

measuring the Raman gain is seen in Fig. 3.5. The pump laser has a centre wavelength of 1453 nm and a full-width at half-maximum (FWHM) of 0.1 nm. An example of the measured Raman gain from the on/off gain measurement is shown in Fig. 3.6. In Fig. 3.7 an example of a calculated complex Raman index of refraction is shown for the Raman gain measurement in Fig. 3.6. It was utilised that the response function in the time domain has to be real and obey causality, which makes the real part of the complex index symmetric and the imaginary part asymmetric. The contribution of the Raman effect to the intensity-dependent index of refraction and thereby also the SPM effect is the real part of the complex Raman refractive index at a frequency detuning of 0 THz. The Raman contribution to the intensity-dependent refractive index is

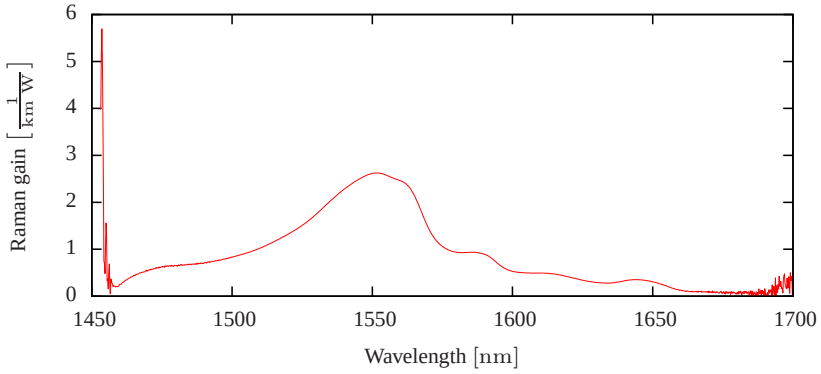

Figure 3.6: Example of a Raman gain measurement.

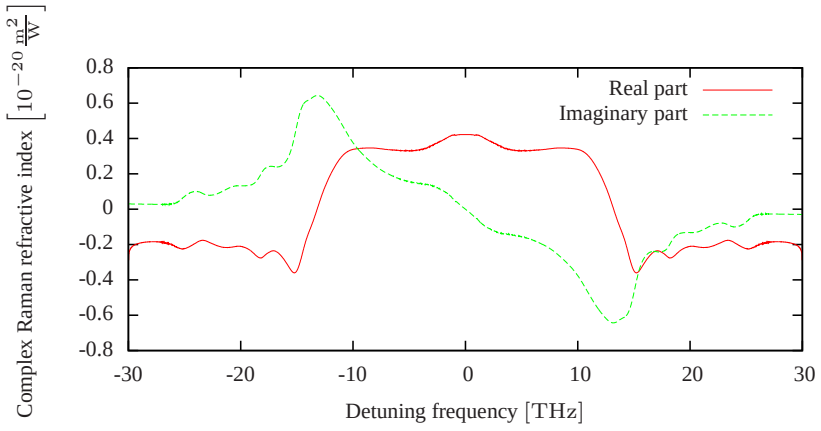

Figure 3.7: Example of the retrieved complex Raman index of refraction.

shown as a function of the weighted germanium concentration as described in Sec. 3.1 in Fig. 3.8. By comparing Figs. 3.4 and 3.8 it is

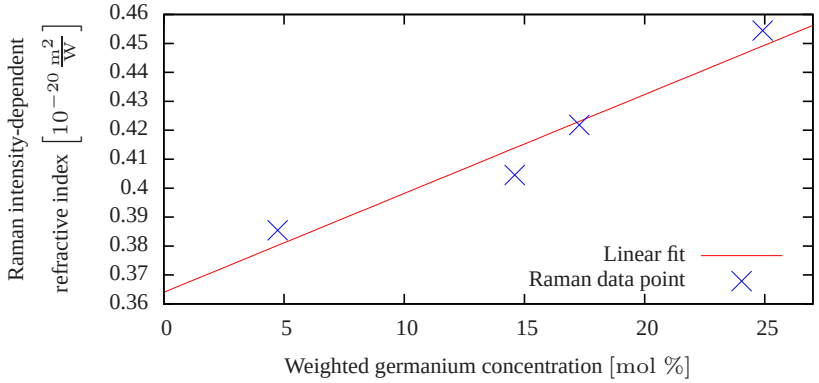

Figure 3.8: The intensity-dependent refractive index from the vibrational/ rotational contributions plotted as a function of the weighted germanium concentration.

observed that there is an additional data point in the measurement for the intensity-dependent refractive index. The corresponding data point has been removed in the measurement for the Raman contribution to the intensity-dependent refractive index as it was suspected to be influenced by multi-mode (MM) effects. By performing a linear regression of the data points, the following expression for the Raman contribution to the intensity-dependent refractive index is obtained

$$n_{2,R}^{I}\left(C_{ge}\right) = 0.00342 \times 10^{-20} \frac{\mathrm{m}^2}{\mathrm{mol}\,\%\,\mathrm{W}}\, C_{ge} + 0.364 \times 10^{-20} \frac{\mathrm{m}^2}{\mathrm{W}} \quad (3.2.5)$$

3.3 Raman Fraction of the Intensity-Dependent Refractive Index

In the two previous sections the intensity-dependent refractive index and the Raman contribution to the intensity-dependent refractive were obtained. The Raman fraction of the intensity-dependent refractive index is given by

$$f_R = \frac{n_{2,R}^{I}}{n_2^{I}}. \quad (3.3.1)$$

The Raman fraction, f_R, as a function of the weighted germanium concentration is shown in Fig. 3.9. It should be noted that the intensity-dependent refractive index is measured at a wavelength of 1550 nm, whereas the Raman contribution to the intensity-dependent refractive index is measured at a wavelength of 1453 nm. However, it is assumed that the intensity-dependent refractive index is independent of the wavelength within the considered wavelength region [37]. The dashed line

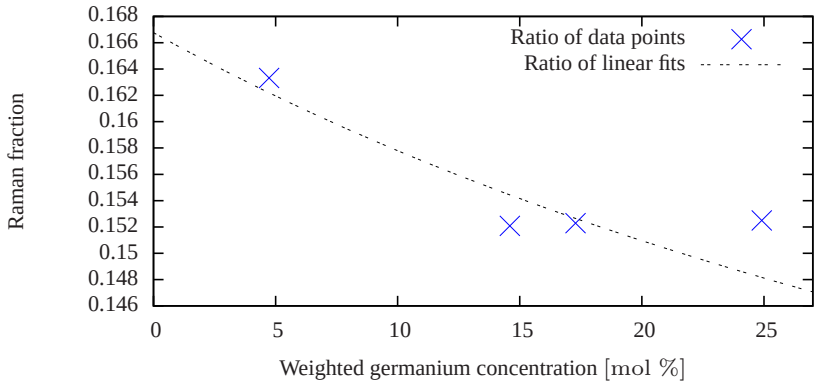

Figure 3.9: The resulting Raman fraction, f_R, from the values of Figs. 3.4 and 3.8. The Raman fraction is plotted as a function of the weighted germanium concentration.

shown in Fig. 3.9 is the ratio between the two linear regressions Eq. 3.2.5 and Eq. 3.1.4, whereas the points are a point-wise calculation using the points from the two data sets. For the point-wise calculation of the Raman fraction the value seems to converge towards a constant value when the weighted germanium concentration is increased, this attributed to the small variations in the two data sets. The small variations become greater in the calculation of the Raman fraction. By calculating the Raman fraction from the two linear regressions the variations in the two data sets are reduced. The dashed line in Fig. 3.9 is smoothly degreasing from 0.167 to 0.148 with an increasing weighted germanium concentration. In the case of a high weighted germanium concentration the Raman fraction is approximately 0.15, hence the error introduced by using the commonly used Raman fraction of 0.18, which is reported for a pure silica fibre to be 20%. This has a significant impact in any application where the Raman effect plays a key role as the Raman fraction, f_R, is directly proportional with the strength of the Raman gain

in the model of the material response given in Eq. 2.2.27 and therefore also with the predicted SSFS.

Chapter 4

Few-Moded Fibres

The soliton energy in a few-moded fibre (FMF) is potentially well matched to a multi-photon microscopy application, as it was motivated in Sec. 1.1. In [30] an experimentally demonstration of a shifted soliton in FMF was performed. The soliton had a pulse energy of 0.8 nJ and a temporal pulse duration of 49 fs. The input to the FMF was a pulse with a temporal duration of 200 fs and a pulse energy of 1.39 nJ. The largest shift of the soliton was from the input wavelength of 1064 nm to a wavelength of 1200 nm. This was obtained with an input pulse energy of 1.63 nJ. The fibre-lase system, which is the main focus of this Ph.D. project is to design and construct a fibre-based laser system, which is able to deliver a wavelength-tunable femtosecond pulse with a pulse energy of 5 nJ. The laser system is to be pumped by an ytterbium-based source and shift the pulses to a wavelength of 1280 nm. The tuning of the pulses is facilitated by the soliton self-frequency shift (SSFS).

In order to satisfy the requirement of the high soliton pulse-energy in a FMF and the large tunable bandwidth, it was realised that this could not be accomplished by using only one fibre. The limitation is set by a mode-crossing between the mode of the soliton and another mode in the fibre. The mode-crossing issue is explained in more detail later on, as this is very significant for the operation of the laser system, but also as the mode-crossing provides a novel simultaneous mode and wavelength-coupling phenomenon. A mode-crossing is generally undesirable for a stable single-mode operation. The mode diagrams shown in this chapter are valid for a straight fibre with perfect cylindrical symmetry. Any imperfection in the fabrication process or deformation of the drawn fibre will break the orthogonality between the modes in the

modes-crossing and create a strong coupling between the two modes. Therefore, the mode-crossing limits the wavelength range in which the soliton can be formed and shifted without any significant loss. To satisfy the pulse energy and bandwidth requirement of the tunable laser system, it was chosen to attempt a two-fibre approach for the SSFS. A schematic representation of the two-fibre approach is shown in Fig. 4.1. The purpose of the LSF is to form a high-energy soliton. The shift of

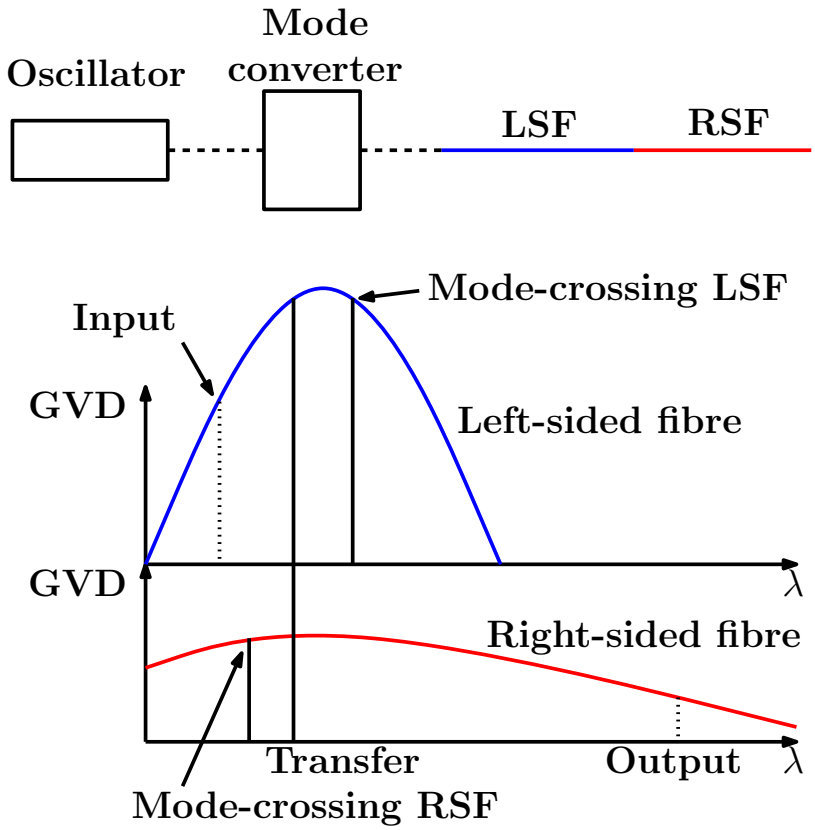

Figure 4.1: A schematic representation of the cascade solution. The source is a mode-lock oscillator, which provides femtosecond pulses. The light is converted to the $LP_{0,2}$ mode before entering the LSF. In the LSF a soliton is generated and shifted to the transfer wavelength. The soliton pulse is coupled to the RSF where the soliton continues to shift to the output wavelength. The transfer wavelength is located between the mode-crossings in the LSF and the RSF.

the soliton in the LSF is limited by the mode-crossing. The soliton-shift condition should be controlled in such a manner that the soliton

is coupled from the LSF to the RSF before the soliton is shifted into the mode-crossing in the LSF. The possible SSFS is much larger in the RSF compared to the LSF. The RSF has a mode-crossing on the lower wavelength side and this sets a requirement of the transfer wavelength between the LSF and the RSF. The mode-crossings in the LSF and the RSF form a wavelength transfer window between the two fibres, if the soliton is to shift to longer wavelengths without entering the mode-crossing. The LSF and RSF are the project names and the names indicate which side of the dispersion curve the use of the fibre is intended for with respect to the mode-crossing.

The design criterion for the fibre-based short pulse laser was devised together with *Chris Xu's* group at *Cornell University*. The initial concept was to use a femtosecond pulse at a wavelength of 1060 nm as the input pulse to the LSF. For the experiments performed at *OFS Fitel Denmark* the centre wavelength of the oscillator was located at a wavelength of 1030 nm. The wavelength shift of the input pulse could be compensated by an increase in the pulse energy according to the simulations performed.

In the following the design and optimisation process of the LSF and the RSF is presented together with the characterisations of the two fibres. This is followed by considerations regarding the excitation of the $LP_{0,2}$ mode. The $LP_{0,2}$ mode is the intended mode of operation in the LSF and the RSF. The chapter is rounded off with a section where it is attempted to splice two different FMFs together.

4.1 Design

The first important step in the design process was to optimise the energy of the soliton pulse from the previously reported soliton energy of 1 nJ [30]. The energy of the soliton pulse is given as

$$E_{\text{sol}} = \frac{N^2 \lambda^3 D A_{\text{eff}}}{2\pi^2 c n_2^I T_0} \propto D A_{\text{eff}}, \tag{4.1.1}$$

where N is the soliton order, λ is the wavelength, D is the group-velocity dispersion, A_{eff} is the effective mode area, c is the speed of light in vacuum, n_2^I is the intensity-dependent refractive index, and T_0 is the pulse duration. From a design perspective using silica glass, the significant parameters related to the energy of the soliton are the group-velocity dispersion, D, and the effective area, A_{eff}, because these

are direct attributes of the wave-guide design. The wave-guide design also influences the value of the intensity-dependent refractive index, however, the change in value is relatively small compared to the possible changes in the values of group-velocity dispersion and effective area. From Eq. 4.1.1 it is given that the soliton energy is directly proportional to the product of the group-velocity dispersion and the effective area. Therefore, to increase the soliton energy, it is a matter of designing a fibre with a very large anomalous dispersion and/or a large effective mode area for the mode of the soliton. The mode of choice of the LSF and the RSF is the $LP_{0,2}$ mode. In order to enhance the wave-guide dispersion of the $LP_{0,2}$ mode, both fibres have a triple-clad design. The triple-clad design was chosen to enhance the features of the $LP_{0,2}$, which is described in more details in the following section. The $LP_{0,2}$ mode was chosen to keep the complexity of the design to a minimum, as a mode of higher-order would introduce several mode-crossings, which should be accounted for.

4.1.1 Left-Sided Fibre

The work in this section is based upon [60, 61]. There is an intuitive explanation regarding the tailoring of the group-velocity dispersion for the $LP_{0,1}$ mode for a triple-clad design in [62], which also applies for the $LP_{0,2}$ mode. The triple-clad design can be viewed as a superposition of two wave-guides, a core wave-guide and a ring wave-guide, as shown in Fig 4.2. To illustrate the decomposition of the triple-clad design

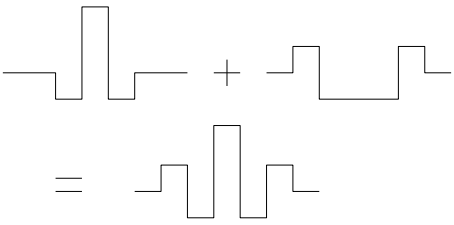

Figure 4.2: Sketch of the refractive index profile for the core, the ring, and the triple-clad wave-guides. The triple-clad design can be viewed as a superposition of two wave-guides, a core wave-guide and a ring wave-guide.

into a core and a ring wave-guide, the effective indices as a function of wavelength are shown for the core, the ring, and the triple-clad wave-guides in Fig. 4.3 for the first couple of modes. The effective indices for

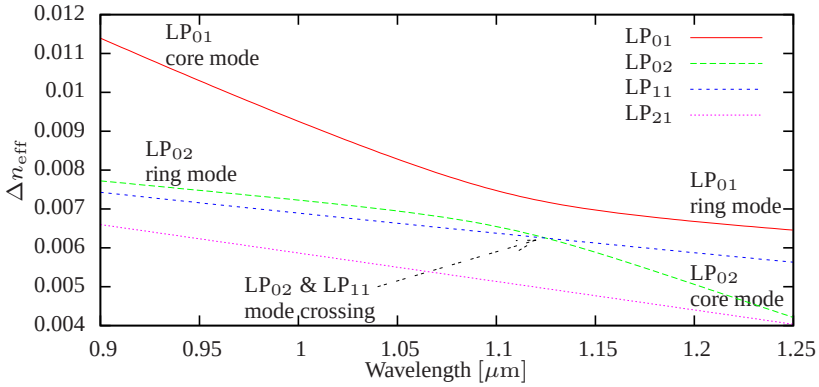

(a) The effective indices of the first four LP modes in the triple-clad fibre, LSF, with respect to pure silica.

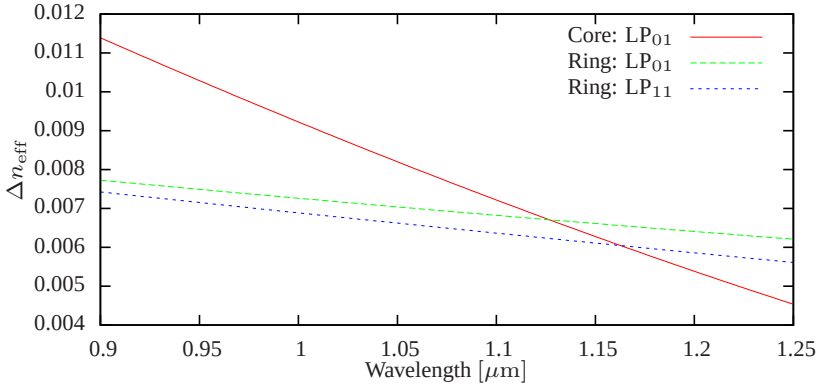

(b) The effective index for the LP$_{0,1}$ mode in the core wave-guide and the effective indices for the LP$_{0,1}$ and LP$_{1,1}$ in the ring wave-guide. All the effective indices are shown with respect to pure silica.

Figure 4.3: The effective index shown as a function of the wavelength for the core, the ring, and the triple-clad wave-guide design.

the individual $LP_{0,1}$ modes in the core and ring wave-guides cross at a wavelength of approximately 1120 nm. Because the core and ring wave-guides are coupled wave-guides in the triple-clad design and they have the same angular symmetry, the two $LP_{0,1}$ modes from the isolated core and ring wave-guides are forced to make an avoided crossing to satisfy the orthogonality requirement. This is seen by comparing Fig. 4.3a and Fig. 4.3b. The $LP_{0,2}$ mode in the triple-clad design starts out as the $LP_{0,1}$ mode of the isolated ring wave-guide at the shorter wavelengths and ends up as the $LP_{0,1}$ mode of the isolated core wave-guide at the longer wavelengths. Therefore, the mode-crossing between the $LP_{0,2}$ and $LP_{1,1}$ modes in the triple-clad design is a consequence of the avoided crossing between the $LP_{0,1}$ and $LP_{0,2}$ modes. The curvature of the avoided crossing increases the closer the intersect angle between the two $LP_{0,1}$ modes from the isolated core and ring wave-guides are to 90°. The curvature of the effective index is directly related to the dispersion value as

$$D = -\frac{\lambda}{c}\frac{d^2 n_{\text{eff}}}{d\lambda^2}. \tag{4.1.2}$$

However, as it is observed from Fig. 4.3b, the closer the intersect angle is to 90°, the closer in wavelength the mode-crossing between the core $LP_{0,1}$ mode and the ring $LP_{1,1}$ mode is to the mode-crossing between the core $LP_{0,1}$ mode and the ring $LP_{0,1}$ mode. Therefore, with the triple-clad design there is a natural trade-off between a high anomalous group-velocity dispersion value for the $LP_{0,2}$ mode and how close the mode-crossing wavelength between the $LP_{0,2}$ and $LP_{1,1}$ modes is to the wavelength of peak value of the group-velocity dispersion.

The optimisation of the peak value of the group-velocity dispersion is performed as explained above while ensuring a relative large effective area, as the $LP_{0,2}$ mode is located mostly in the ring structure of the wave-guide for the wavelengths below the avoided crossing. The optimised design is a compromise of soliton energy and the wavelength range for SSFS in the LSF as explained above. This was verified numerically as the design-parameter space of the LSF was thoroughly investigated by running numerous computations of different configurations to find the optimum design with the highest soliton energy. The different configurations were perturbations of the triple-clad design. The result of the optimisation process is shown in Fig. 4.4. The product of the group-velocity dispersion and the effective area, i.e. the energy of the soliton see Eq. 4.1.1, at the wavelength of 1060 nm is shown as a function of

the mode-crossing wavelength for different wave-guide designs. Fig. 4.4

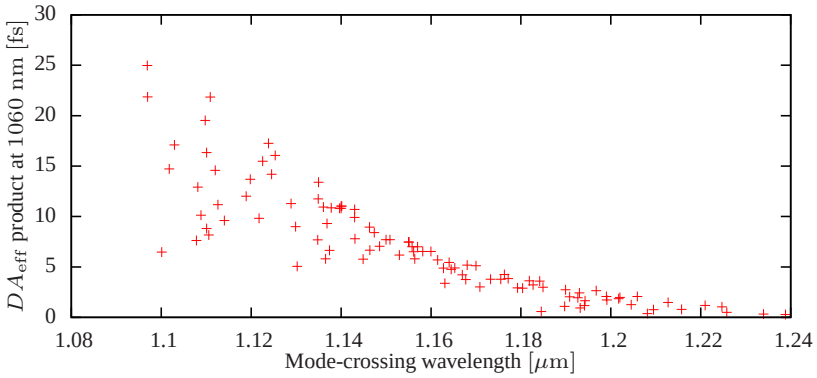

Figure 4.4: The product of the group-velocity dispersion and the effective area at the wavelength of 1060 nm is shown as a function of the mode-crossing wavelength for different wave-guide designs.

shows that the mode-crossing wavelength moves closer to the input wavelength of 1060 nm, as the product of the group-velocity dispersion and the effective area increases. As a compromise between the soliton energy and the stability, the optimised design of the LSF has a mode-crossing between the $LP_{0,2}$ and $LP_{1,1}$ modes at approximately 1120 nm. Fig. 4.3a shows the effective indices as a function of wavelength for the first four LP modes of the final version of the LSF. Fig. 4.5 shows the group-velocity dispersion and effective area of the $LP_{0,2}$ mode as well as the product of the group-velocity dispersion and the effective area. Figs. 4.3a and 4.5a show that the mode-crossing wavelength is close to the wavelength at the peak of the group-velocity dispersion curve. In this optimisation process we have focused on the $LP_{0,2}$ mode, however, other higher-order-modes (HOMs) could also be utilised. In general, the process would become more complex because more mode-crossings should be considered, but by using a mode of higher-order the effective area is increased and thereby also the soliton energy.

4.1.2 Right-Sided Fibre

The LSF and the RSF are to be used in a cascaded configuration. Therefore, the design parameters of the RSF are dependent on the final LSF design. The mode-crossing in the LSF is located approximately around 1120 nm. The longest wavelength intended for coupling the soliton pulse from the LSF to the RSF is 1100 nm, as this will provide some

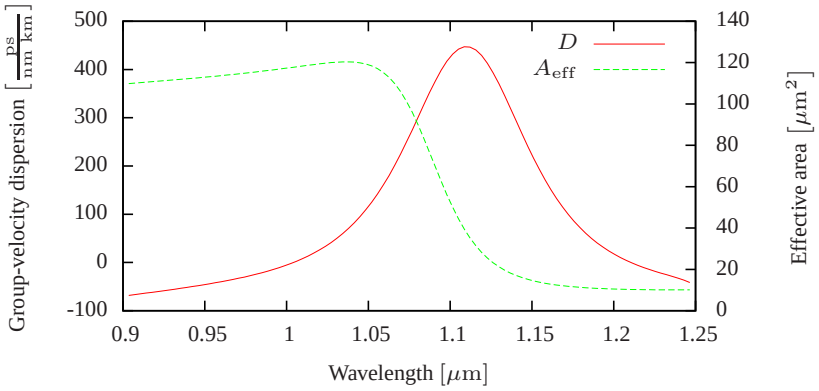

(a) The group-velocity dispersion and the effective area of the $LP_{0,2}$ mode.

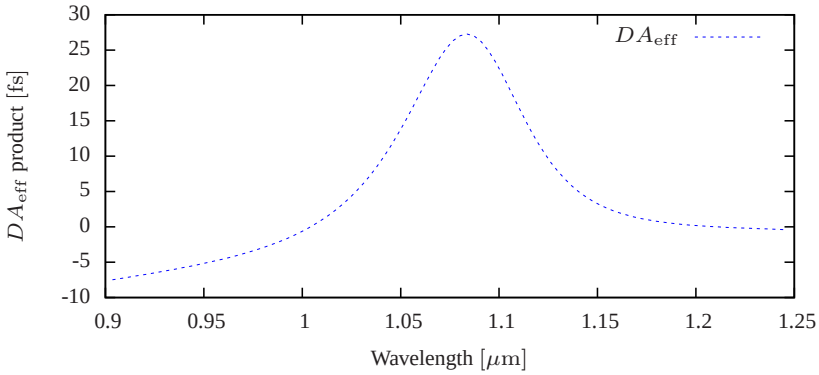

(b) The product of the group-velocity dispersion and the effective area curves of the $LP_{0,2}$ mode.

Figure 4.5: The group-velocity dispersion and the effective area of the $LP_{0,2}$ mode as well as the product of the group-velocity dispersion and the effective area.

distance in wavelength to the mode-crossing in the LSF for the shifted soliton. The shifted soliton will have a temporal duration in the sub-picosecond range. As the soliton pulse is required to shift to a wavelength of 1280 nm, this sets a requirement for the anomalous region in the RSF. Another requirement is that the single-soliton condition continues to be satisfied in the RSF. This includes the splice loss between the LSF and the RSF. Basically, by comparing the soliton pulse energy as given in Eq. 4.1.1 for the LSF and the RSF the following expression is obtained

$$N_{\mathrm{RS3}} = \sqrt{\frac{D_{\mathrm{LS5}} A_{\mathrm{eff,LS5}}}{D_{\mathrm{RS3}} A_{\mathrm{eff,RS3}}}}. \tag{4.1.3}$$

If the soliton number of the RSF is less than one, then the pulse will broaden as a dispersive wave until the pulse duration matches the soliton requirement. If the pulse duration enters the picosecond range, the SSFS will be greatly reduced [26]. Therefore, it is not desirable to have a soliton number less than one for the RSF. However, if the soliton number of the RSF is much larger than one, then the soliton pulse will generate a super-continuum, which is undesirable. A soliton of order N will undergo soliton fission and split up into N fundamental soliton provided there is a sufficient length of fibre [63]. Therefore is it difficult to set a strict upper limit on the ratio between the product of the group-velocity dispersion and the effective area in the RSF and in the LSF. More details about coupling a soliton between two fibres can be found in [64].

For the RSF the issue with the mode-crossing between the $\mathrm{LP}_{0,2}$ mode and the $\mathrm{LP}_{1,1}$ mode is present as this is generic to the triple-clad design as explained in Sec. 4.1.1. To facilitate the long wavelength shift of the soliton, the mode-crossing is designed to be at a shorter wavelength than the transfer wavelength between the LSF and the RSF. In Fig. 4.6 the effective indices for the first four LP modes are shown for the RSF. The corresponding group-velocity dispersion and effective area of the $\mathrm{LP}_{0,2}$ mode as well as the product of the group-velocity dispersion and the effective area are shown in Fig. 4.7. Another limiting factor for the RSF design is a consequence of the requirement of the broad anomalous region as there is a potential mode-crossing between the $\mathrm{LP}_{0,2}$ mode and the $\mathrm{LP}_{2,1}$ mode at the longer wavelengths for the triple-clad design. This is not shown in Fig. 4.6, however, it can be indicated if the effective indices for the $\mathrm{LP}_{0,2}$ mode and the $\mathrm{LP}_{2,1}$ mode

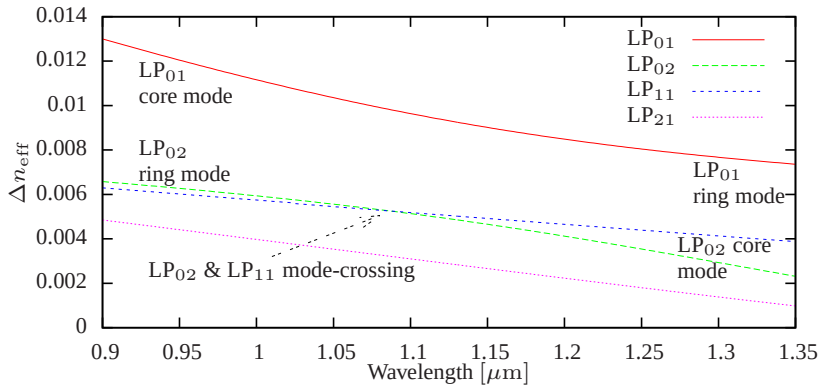

Figure 4.6: The effective indices of the first four LP modes in the RSF, with respect to pure silica.

are extrapolated towards longer wavelengths. In summary, the peak value of the group-velocity dispersion curve for the RSF design is limited by the requirement of a broad anomalous region, the mode-crossing between the $LP_{0,2}$ mode and the $LP_{1,1}$ mode, and the mode-crossing between the $LP_{0,2}$ mode and the $LP_{2,1}$ mode.

The anomalous region of the RSF extends to a longer wavelength than the design target of 1280 nm to anticipate the cancellation of the SSFS due to the coupling of light from the soliton pulse to a dispersive wave in the normal dispersion region generated by the Čerenkov process [65, 66].

The ratio of the product of the group-velocity dispersion and the effective area between the LSF and the RSF at the transfer wavelength of 1100 nm is 4.2. This means that the splice loss between the LSF and the RSF can be up to 6.2 dB and the soliton condition in the RSF would still be satisfied. If the splice loss between the LSF and the RSF is negligible, a soliton of order 2 would be formed in the RSF, which at maximum should give two solitons during the soliton fission process [63]. Two solitons are hardly enough for the generation of a super-continuum over the considered bandwidth.

4.2 Characterisation

The LSF has undergone the most extensive characterisation, as this fibre was the first fabricated and the design of the RSF depended on the properties of the drawn LSF. Both fibres were characterised by analysing the

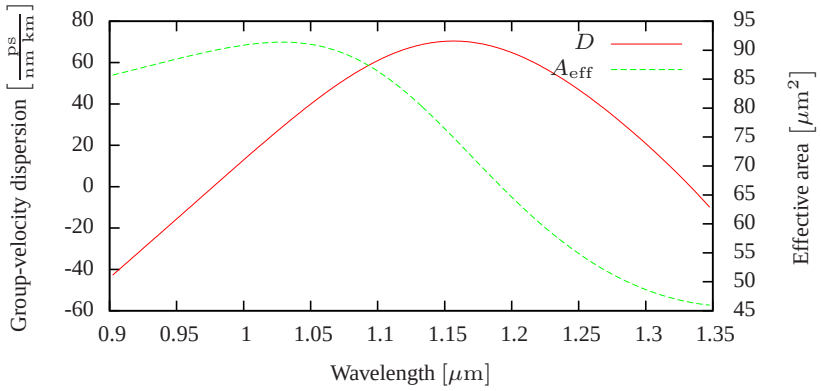

(a) The group-velocity dispersion and the effective area of the $LP_{0,2}$ mode.

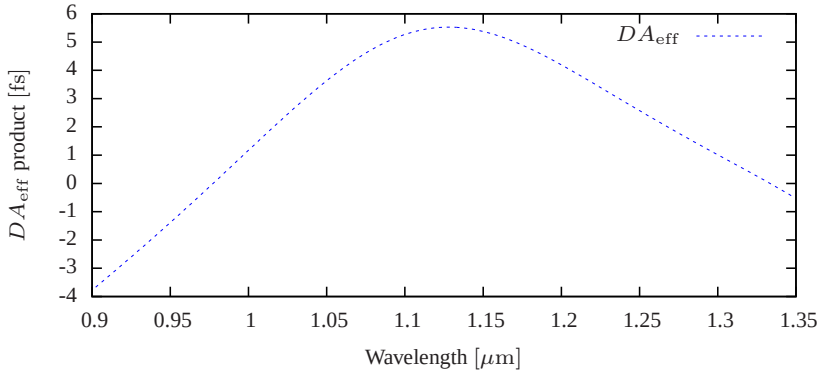

(b) The product of the group-velocity dispersion and the effective area curves of the $LP_{0,2}$ mode.

Figure 4.7: The group-velocity dispersion and the effective area of the $LP_{0,2}$ mode as well as the product of the group-velocity dispersion and the effective area.

interferometric beat pattern with a sliding Fourier-transform-window. The dispersion of multiple modes in LSF was measured in the time domain and the dispersion of the $LP_{0,1}$ mode was measured in the spectral domain. Each method is treated separately in the following.

4.2.1 Sliding Fourier-Transform-Window

For the sliding Fourier-transform-window method the interferometric beat patterns between several modes are recorded by an optical-spectrum analyser (OSA). The measurement is similar to the one presented in [67]. A sketch of the measurement setup is shown in Fig. 4.8; a

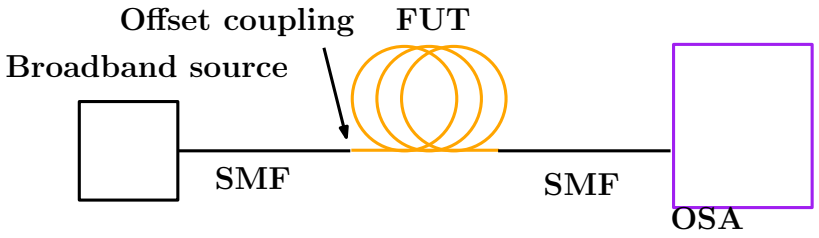

Figure 4.8: The setup for the interferometric measurement.

single-mode broadband source, which is off-set coupled to the fibre-under-test (FUT) in order to excite a multiple number of modes. The light out of the FUT is collected with a single-mode fibre (SMF) and recorded on an OSA. As the modes will have experienced different group delays through the FUT and they are forced to interfere in the collecting SMF, the recorded spectrum will exhibit beat patterns corresponding to the difference in the group-velocity between the modes. The choice of source should depend on where the fibre has noticeable features in the beat pattern.

The sliding Fourier-transform-window method is however also known as the short-time Fourier-transform. The mathematical description of the operation is given as

$$\tilde{x}\left(\Lambda, K_{\text{freq}}\right) = \int_{-\infty}^{\infty} x\left(\lambda\right) w\left(\lambda - \Lambda\right) \exp\left[-i2\pi K_{\text{freq}}\lambda\right] \mathrm{d}\lambda, \qquad (4.2.1)$$

where x is the measured quantity, which is the transmission spectrum from the interferometric measurement, w is the window function, which is a raised cosine, λ is the wavelength, Λ is the tuning wavelength of the window function, and K_{freq} is the inverse Fourier-transform variable of

the wavelength. The K_{freq} is be equal to

$$K_{\text{freq}} = \frac{L}{\lambda^2} \left| \Delta n_g \right|, \tag{4.2.2}$$

where L is the length of the FUT, λ is the wavelength, and Δn_g is the difference in group index between the two modes interacting.

Left-Sided Fibre

In this section the result of the interferometric measurement on the LSF is presented. The length of the FUT was 1.949 m. The light source is an ytterbium-based amplified spontaneous emission (ASE) source. In order to clearly resolve all the oscillations in the transmission spectrum the resolution of the OSA was 0.02 nm. Applying the sliding Fourier-transform-window method to the recorded transmission spectrum results in a counter plot, shown in Fig. 4.9. The window size was 3.2 nm and the spacing between the sample points was 6.4 nm. Fig. 4.9 is a close-up on the region of interest, where the limits of the colour-bar have been rescaled to remove some of the noise. The original contour plot and the measured spectra are found in App. A.2.1. The strongest

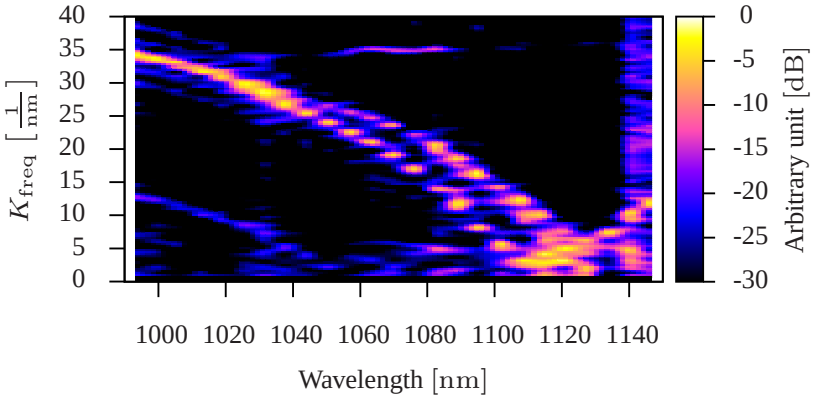

Figure 4.9: The sliding Fourier-transform-window method applied to the interferometric data.

beat frequencies are the two starting at the shorter wavelength just below $K_{\text{freq}} = 40\ \frac{1}{\text{nm}}$ and going to zero at a wavelength approximately at 1120 nm. In Fig. 4.10 the calculated absolute group-index difference between the first LP modes in the LSF are shown together with the retrieved absolute difference in group index from the lower branch of

the two strongest beatings in Fig. 4.9. The value of the lower branch of the two strongest beatings is retrieved by locating the peaks in Fig. 4.9 and storing them of each sample wavelength. The two strong beatings

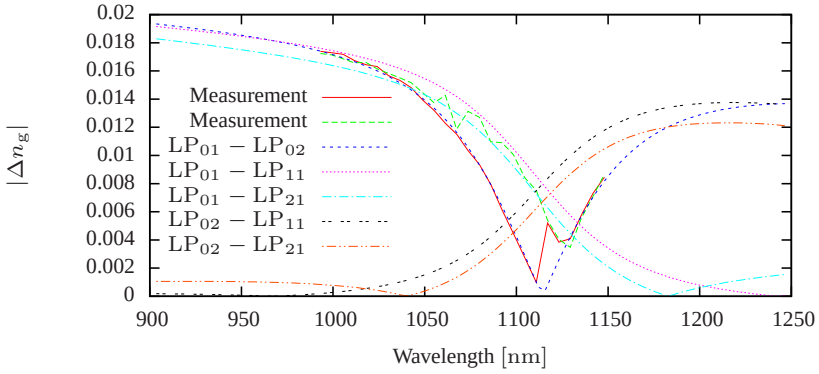

Figure 4.10: Comparison between the retrieved absolute group-index from the measurement and different calculated mode pairs. It is observed that the retrieved peak from the measured data is not correctly located for every data point. This explains the variation in the signal strength in the beat pattern.

in Fig. 4.9 are identified as the beating between the $LP_{0,1}$ mode and the $LP_{0,2}$ mode and a beating between the $LP_{0,1}$ mode and the $LP_{1,1}$ mode. The mode of most interest is the $LP_{0,2}$ mode and it is observed that the $LP_{0,1}$ mode and the $LP_{0,2}$ mode have a turn-around-point (TAP) at the approximate wavelength of 1120 nm. Disregarding a small discrepancy around the TAP, which is caused by a beating between some of the other modes, the agreement is excellent for the measured and calculated difference in the group index between the $LP_{0,1}$ mode and the $LP_{0,2}$ mode.

Right-Sided Fibre

In this section the result of the interferometric measurement on the RSF is presented. The length of the FUT was 7.940 m. The light source consists of four super-luminescent light-emitting-diodes. The resolution of the OSA was 0.05 nm in order to clearly resolve all the oscillations in the transmission spectrum. Applying the sliding Fourier-transform-window method to the recorded transmission spectrum results in a counter plot, shown in Fig. 4.11. The window size was 4 nm and the spacing between the sample points was 5 nm. Fig. 4.11 is a close-up on the region of interest, where the limits of the colour-bar have been rescaled to remove some

of the noise. The original contour plot and the measured spectra are found in App. A.2.1. In Fig. 4.12 the calculated absolute group-index

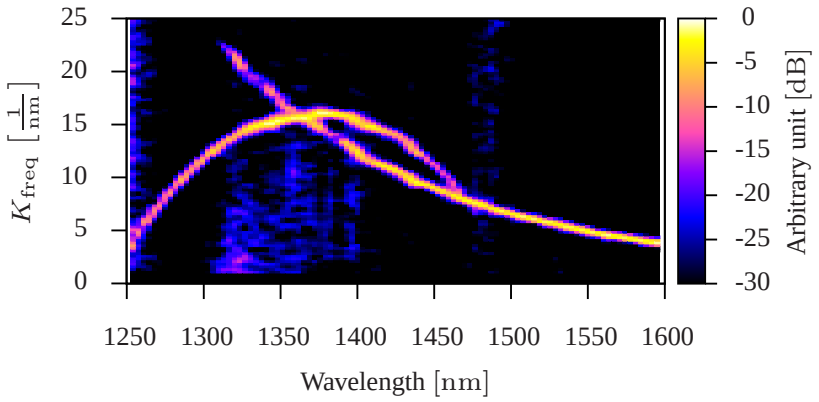

Figure 4.11: The sliding Fourier-transform-window method applied to the interferometric data.

difference between the $\mathrm{LP}_{0,1}$ mode and the $\mathrm{LP}_{0,2}$ mode and between the $\mathrm{LP}_{0,1}$ mode and the $\mathrm{LP}_{1,1}$ mode in the RSF are shown together with the retrieved absolute difference in group index from Fig. 4.11. The value of the two branches of beatings is retrieved by locating the peaks in Fig. 4.11 and storing them of each sample wavelength. The agreement

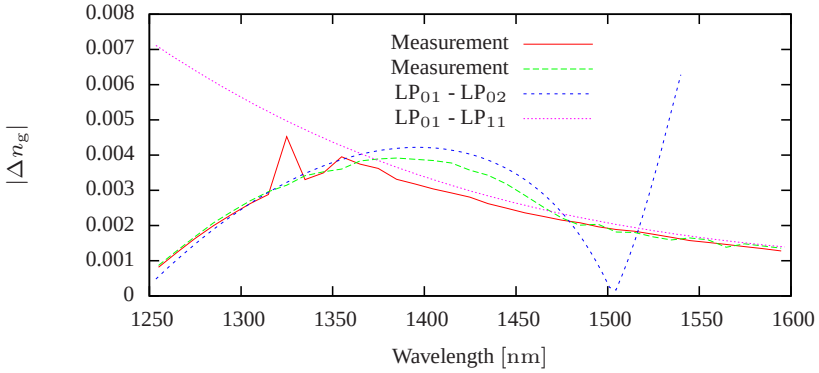

Figure 4.12: Comparison between the retrieved absolute group-index from the measurement and the calculated difference between the $\mathrm{LP}_{0,1}$ mode and the $\mathrm{LP}_{0,2}$ mode and between the $\mathrm{LP}_{0,1}$ mode and the $\mathrm{LP}_{1,1}$ mode. It is observed that the retrieved peak from the measured data is not correctly located for every data point. This explains the variation in the signal strength in the beat pattern.

between the measurement and the calculation is not as excellent as for

the LSF, however, it is quite reasonable. The cut-off wavelength for the $LP_{0,2}$ mode is approximately at a wavelength of 1540 nm, which is why the curve for the absolute group-index difference between the $LP_{0,1}$ mode and the $LP_{0,2}$ mode stops at this wavelength in Fig. 4.12.

4.2.2 Temporal Dispersion Measurement

The work in this section is based upon [68]. The interferometric measurement in the previous section, Sec. 4.2.1, was an indirect measurement of the dispersive properties of the FUT, whereas the temporal dispersion measurement, described in this section, is a direct measurement of the dispersive properties of the FUT. The general concept of the measurement is to use the output from a mode-locked laser to excite multiple modes when coupling into the FUT, after which the output from the FUT is measured on a fast oscilloscope. This is performed for a number of discrete wavelengths and thereby the relative group delay for each excited mode can be recorded as a function of wavelength. The experimental setup is shown in Fig. 4.13. An 80 MHz

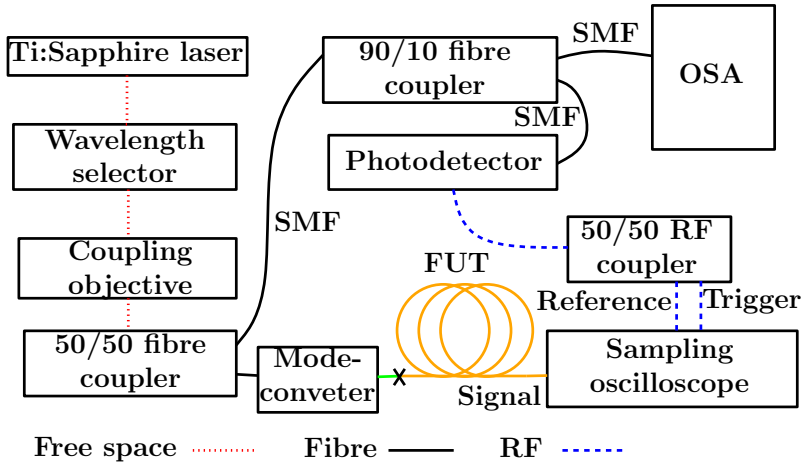

Figure 4.13: Sketch of the dispersion measurement.

mode-locked Ti:Sapphire laser is used as the input source. The initial input wavelength is continuously tuned between 1010 nm and 1070 nm, with a spectral bandwidth in the range of 10 nm to 20 nm. The input bandwidth is then spatially filtered to 1 nm by a tunable wavelength selector. The incident beam is split by a 50/50 fibre coupler, which splits the light into the FUT and the reference arm. The total input

pulse energy is maintained below 1 pJ to avoid fibre non-linearities. In the FUT multiple modes are simultaneously excited after launch, this is done with an off-set splice. The output from the FUT is measured by a 30 GHz sampling oscilloscope with a fast photo detector module (*Agilent 86100A Infiniium DCA sampling oscilloscope*). The incident pulses on the detector have a duration of approximately 2 ps or less, which is well below the impulse response time of the detector. The recorded pulses are therefore determined by the impulse response of the detector, however, the oscilloscope has a temporal precision of 250 fs, which means that a delay shift of 1 ps can be measured. In the reference arm, the optical power is split by a 90/10 fibre coupler. The 90% arm is detected by a 20 GHz detector. The electrical pulse train is then split by a 50/50 RF coupler to trigger the oscilloscope and provide a reference signal. The 10% arm is coupled into an OSA to measure the input wavelength.

As the mode of most interest is the $LP_{0,2}$ mode, a mode-converter is used to excite the light to the $LP_{0,2}$ mode. The mode-converter is off-set spliced to the FUT, which is the LSF and as a consequence both the $LP_{0,1}$ mode and $LP_{1,1}$ mode are excited together with the $LP_{0,2}$ mode. In Fig. 4.14 an example of the recorded temporal trace is shown for a wavelength of 1064 nm. The three peaks in the trace

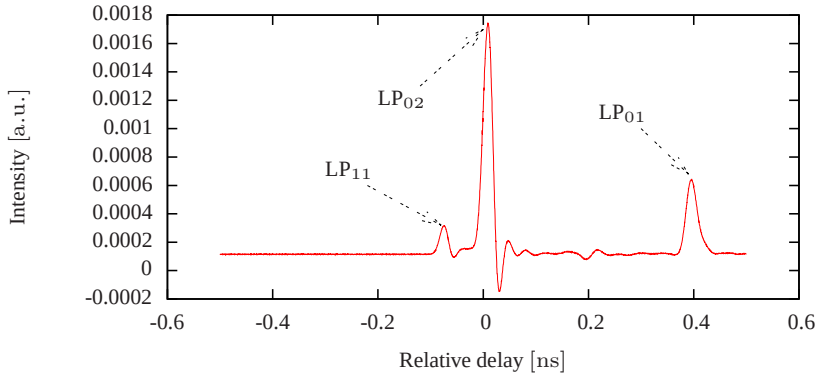

Figure 4.14: An example of the recorded temporal trace at a wavelength of 1064 nm.

correspond to the $LP_{1,1}$ mode, the $LP_{0,2}$ mode, and the $LP_{0,1}$ mode. Each peak is continuously tracked to ensure that it represents the same mode during the wavelength-tuning process. The amplitudes of the peaks represent the relative optical power in each excited mode, and

the temporal positions of the peaks indicate the relative delay of each mode with respect to the reference pulse from the reference arm. At each input wavelength, the relative delay of each mode is measured and the relative delay can be expressed as

$$\tau = \tau_X - \tau_{Ref} + C_{RF} = \frac{L_X}{v_{g,X}} - \frac{L_{Ref}}{v_{g,Ref}} + C_{RF}, \tag{4.2.3}$$

where τ is the relative delay between mode X and the reference pulse. τ_X represents the group delay of mode X after the mode has propagated through the LSF, and τ_{Ref} represents the group delay of the reference pulse. $v_{g,X}$ and $v_{g,Ref}$ are, respectively, the group velocities of mode X in the LSF and the fundamental mode in the SMF of the reference arm. L_X and L_{Ref} represent, respectively, the lengths of the LSF and the SMF. C_{RF} is the constant delay introduced by the RF devices in the system. The length of the LSF in the measurement was 10.2 m. The length of SMF in the reference arm has been adjusted to account for the SMF in the signal arm and the resulting length was 1.7 m. The only part which is not accounted for is the small length of FMF in the mode-converter, however, as this length is less than 10 cm, this contribution is neglected. Both the calculated and measured relative group delays as a function of wavelength for the $LP_{0,1}$ mode, the $LP_{0,2}$ mode, and the $LP_{1,1}$ mode are shown in Fig. 4.15 . The agreement between the

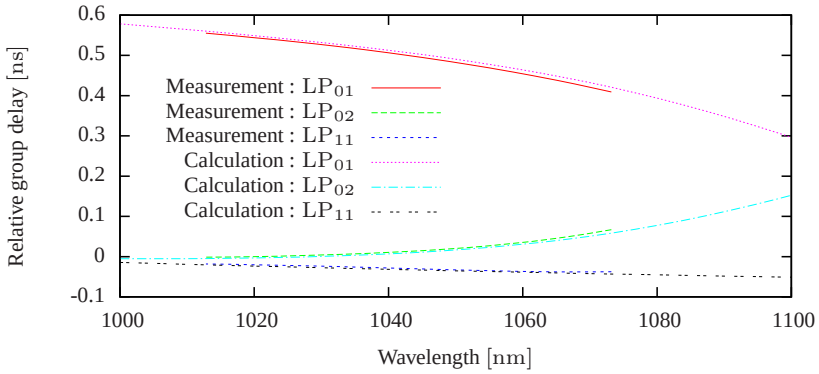

Figure 4.15: The measured and calculated relative group delays as a function of wavelength for the $LP_{0,1}$ mode, the $LP_{0,2}$ mode, and the $LP_{1,1}$ mode.

calculated and measured relative group delay is excellent. The relative precision of the measured delay can be further improved by using longer lengths of LSF. However, the relative delay between two modes in the fibre must be shorter than the periodicity of the pulse train.

As this is a direct measurement of the dispersive properties of the fibre the group-velocity dispersion can be calculated from the measured relative group-delay. In Fig. 4.16 both the measured and calculated group-velocity dispersion are shown for the $LP_{0,1}$ mode, the $LP_{0,2}$ mode, and the $LP_{1,1}$ mode. The relative group delay is fitted with a third-

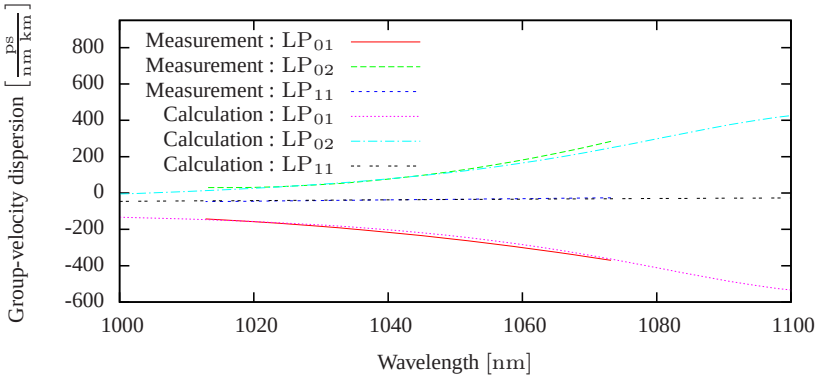

Figure 4.16: The measured and calculated group-velocity dispersion as a function of wavelength for the $LP_{0,1}$ mode, the $LP_{0,2}$ mode, and the $LP_{1,1}$ mode.

order polynomial for the $LP_{0,1}$ mode and the $LP_{0,2}$ mode and a second-order polynomial is used for the $LP_{1,1}$ mode. Once again the agreement between the measurement and calculation is excellent.

4.2.3 Group-Velocity-Dispersion Measurement

A commercial group-velocity-dispersion measurement setup used for characterising single-mode telecommunication fibres can be used to measure the dispersive properties of a FMF if care is taken only to excite a single mode. This is achieved by stripping the fibre of all but a single mode, e.g. if the input of the FUT is tapering down to a fibre diameter where all the HOMs are unguided. The main disadvantage with this is that it is only possible to measure the group-velocity dispersion of the fundamental mode. An alternative could be to measure the group-velocity dispersion with a broadband mode-converter before the FUT. This is not trivial for the LSF as will be described later on in Sec. 4.3. The LSF was tapered using a similar method to the one described in [69]. Index oil was applied to the taper before the measurement was carried out. The measurement was performed with a *Photon Kinetic 2800 Dispersion/Stain* unit. The length of LSF was

468 m. When the fibre is tapered, the dispersive properties are altered. However, as the taper region is only a couple of centimetres the error is negligible. In Fig. 4.17 the measured and calculated group-velocity dispersion are shown for the $LP_{0,1}$ mode. The agreement between the

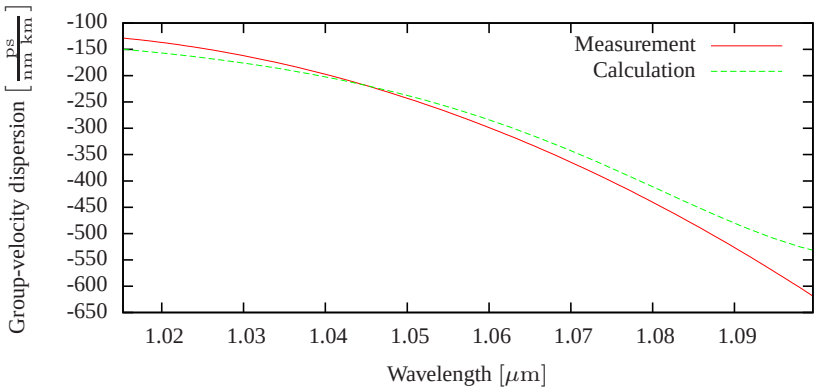

Figure 4.17: The measured and calculated group-velocity dispersion as a function of wavelength for the $LP_{0,1}$ mode.

measurement and calculation does not match as well as the previous comparisons, however, it is still good. The polynomial fit used for the measured group delay is a third-order polynomial. As for this measurement and the temporal dispersion measurement there will always be some artefacts in the end interval of the measured values due to the polynomial fit.

4.3 Excitation of the $LP_{0,2}$ Mode

For utilising the anomalous dispersion properties of the $LP_{0,2}$ mode in the LSF and later on in the RSF a method for successful excitation of the mode is needed. One commonly used method is to induce a long-period grating (LPG) to the fibre. There are various different techniques for inducing a LPG to a given fibre. The grating could be a micro-bend grating [70, 71], which is only ideal for the coupling between symmetric and asymmetric modes. Writing of LPGs with a CO_2 laser is also possible [72], or with high-powered femtosecond-pulses, which induce damage in the silica lattice [73]. Another possibility is to utilise that germanium-doped silica produces a refractive index change due to a photosensitive process [74] to write an ultraviolet (UV) LPG. Other

mode-conversion techniques involve phase plates [75] or spatial light modulators [76]. As the design criterion for the final laser system is an all-fibre system, it is the UV LPG method, which is of interest.

The resonance condition for the LPG can be found when the detuning parameter equals zero. The detuning parameter, δ, is given as [77]

$$\delta(\lambda) = \frac{1}{2}\left(\frac{2\pi}{\Lambda} - \Delta\beta(\lambda)\right), \tag{4.3.1}$$

where λ is the wavelength, Λ is the grating period, and $\Delta\beta$ is the difference in propagation constants between the two modes. The resonance condition can be written as

$$\lambda_{res} = \Delta n_{neff}\Lambda, \tag{4.3.2}$$

where Δn_{neff} is the difference in effective index between the two modes. To a first approximation the following expression is valid

$$\frac{\mathrm{d}\Lambda}{\mathrm{d}\lambda_{res}} = \frac{\Delta n_g}{n_{eff}^2}, \tag{4.3.3}$$

where Δn_g is the difference in group index between the two modes. From Eq. 4.3.3 it is realised that the bandwidth of the LPG is broadest where the group-index difference equals zero. This is also referred to as the TAP. In Fig. 4.10 it is observed that the $LP_{0,1}$ mode and $LP_{0,2}$ mode experience a TAP at a wavelength of approximately 1110 nm, which is also almost the same wavelength as the mode-crossing between the $LP_{0,2}$ mode and $LP_{1,1}$ mode, which is at a wavelength of 1120 nm. This complicates the mode conversion in the LSF, since a LPG with a significant bandwidth has to be close to the mode-crossing. This is also a consequence of the requirement of a high soliton-pulse energy. Therefore, another approach is required. The chosen solution was to write the LPG in another FMF where it was possible to have the grating resonance wavelength within the ytterbium gain band. However, this of course requires a splice between two different FMFs with low loss and with the correct coupling of the modes. Furthermore, a splice between the LSF and the RSF is also required for the cascade idea to work in an all-fibre solution.

4.3.1 Mode-Converter Fibre

The mode-converter fibre shown in this section is optimised for a mode conversion at 1030 nm and used to convert the output of the HOM

dispersion balanced laser, which is presented in Sec. 5.1. The mode-converter fibre was originally fabricated as part of the OFS *Femto-Comp* product line. For various reasons the availability of pre-fabricated mode-converters was non-existent. To fabricate broadband LPGs the resonance wavelength should be located at the wavelength of the TAP. In Fig. 4.18 the difference in group index between the $LP_{0,1}$ mode and the $LP_{0,2}$ mode in the mode-converter fibre is shown. The TAP is observed to be ideal for a broadband mode conversion at approximately 1030 nm. In Fig. 4.19 the group-velocity dispersion and the effective

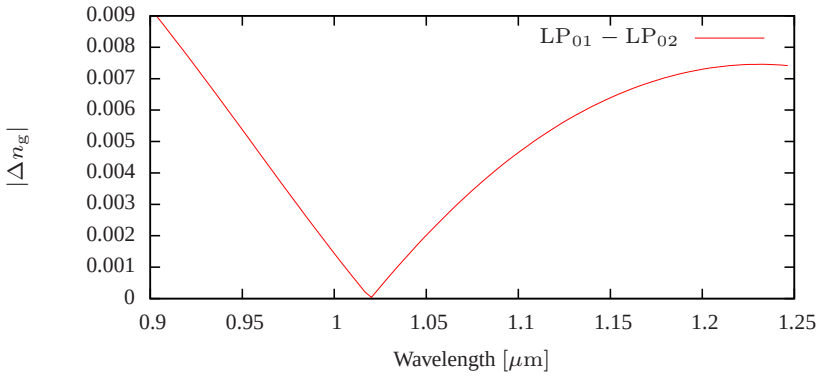

Figure 4.18: The calculated group-index difference between the $LP_{0,1}$ mode and the $LP_{0,2}$ mode as a function of wavelength in the mode-converter fibre.

area are shown for the $LP_{0,2}$ mode. The values are small when com-

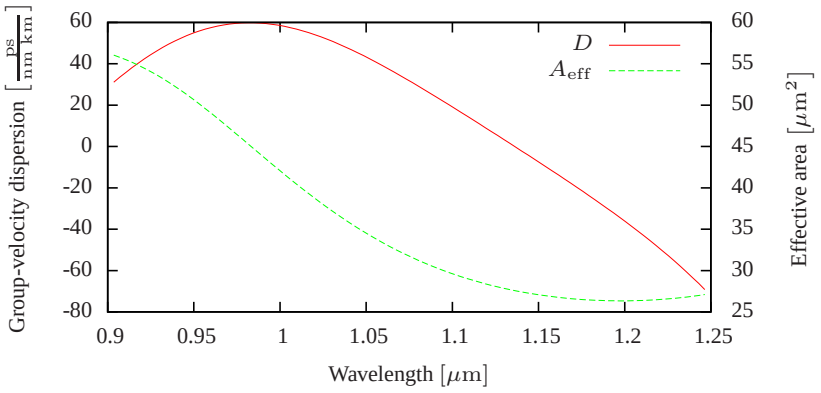

Figure 4.19: The group-velocity dispersion and the effective area of the LP_{02} mode in the mode-converter fibre.

pared to the values of the LSF. Therefore the soliton threshold is lower

in the mode-converter fibre compared to the LSF. This could potentially have an influence on the soliton pulse formation depending on the length of the mode-converter fibre.

UV LPGs were written in the mode-converter fibre with an amplitude-mask placed after the fibre had been loaded with hydrogen in a high-pressure chamber [78]. A typical grating transmission is shown in Fig 4.20, where the fibre was tapered on either side of the grating. The first taper is to have a pure $LP_{0,1}$ mode before the grating, the second taper is to remove the converted $LP_{0,2}$ mode after the grating and record the residual $LP_{0,1}$ mode, which has not been converted by the grating.

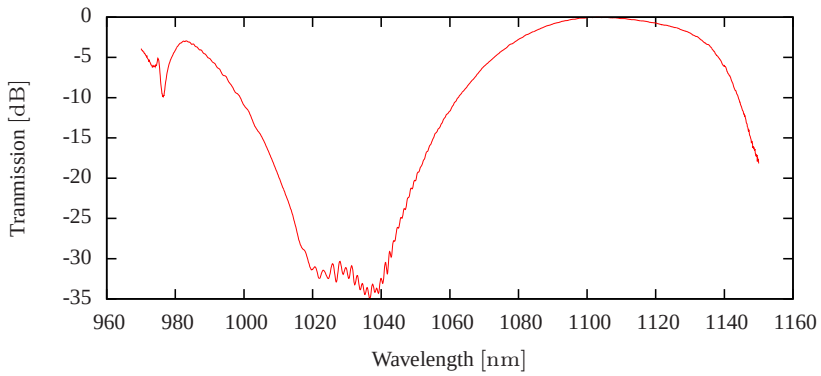

Figure 4.20: A typical transmission characteristic through one of the LPGs written during the project. The transmission is a measure for the amount of residual $LP_{0,1}$, which has not been converted.

4.3.2 Splicing of Few-Moded Fibres

The splice loss between two identical FMFs is in general quite low, in [79] it was reported to be 0.3 dB. However, this is in general not the case for two different FMFs. The potential for splicing one mode from the first fibre to a different mode in the second fibre is significant as the modes in the two fibres have different transverse field distributions.

To investigate the possibility of splicing two different FMFs together, a simulation of the splice-loss evolution was performed. The programme to simulate the splice loss was written by *Torben Veng* from *OFS Fitel Denmark*. The programme solves the diffusion equation for the refractive index profile of the two fibres. Afterwards the diffused index profiles are used to calculate the field overlap between the mode from

the first and second fibres. The simulated fusion splice loss for the mode-converter fibre and the LSF at a wavelength of 1030 nm is shown in Fig. 4.21. The splice loss increases rapidly in the beginning until it

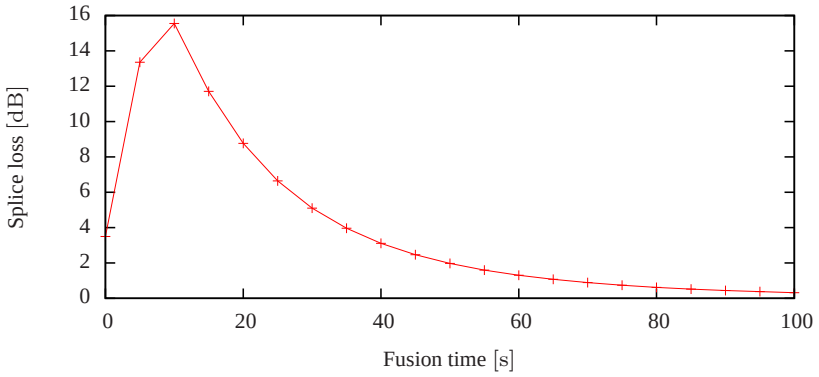

Figure 4.21: Simulated fusion splice-loss between the mode-converter fibre and the LSF for the $LP_{0,2}$ mode.

reaches a maximum. Afterwards it gradually decreases and slowly reduces towards zero. Unfortunately, it is not possible to splice two fibres for such a long period of time in a fusion splicer. Instead a two-step process was performed, where the first step consists of splicing the fibres together in a fusion splicer and in the second step defusing the material over a gas-line burner. The gas-line burner works at a much lower temperature than the fusion splicer, however, as diffusion is a product of time and heat, it should be possible to obtain the same effect just over a longer time. Of course there is an underlying assumption that the diffusion coefficients of the different materials in the fibre have the same temperature dependence. The reason that splice loss goes asymptotic towards zero for a long splice time can be understood by comparing the evolution of the refractive index profile over time. In Fig. 4.22 the refractive index profiles for the mode-converter fibre and the LSF are shown for the sampled fusion times in Fig. 4.21. Both fibres seem similar before the splice process due to the fact that they both have a triple-clad structure. However, as soon as the splice process begins, the similarities disappear. The mode-converter fibre diffuses into a very big single core with a small oscillation on top, whereas the LSF diffuses into a sinusoidal profile. This explains the rapid increase in the splice loss in the beginning of the process. As the splice process continues, the material in both fibres diffuse even more and towards the end both fibres have

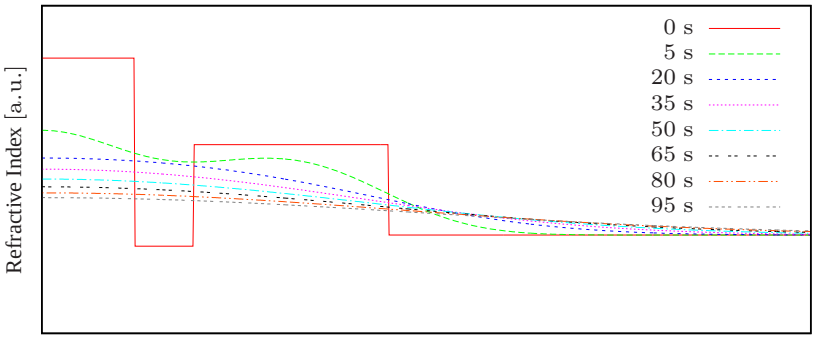

(a) Mode converter fibre.

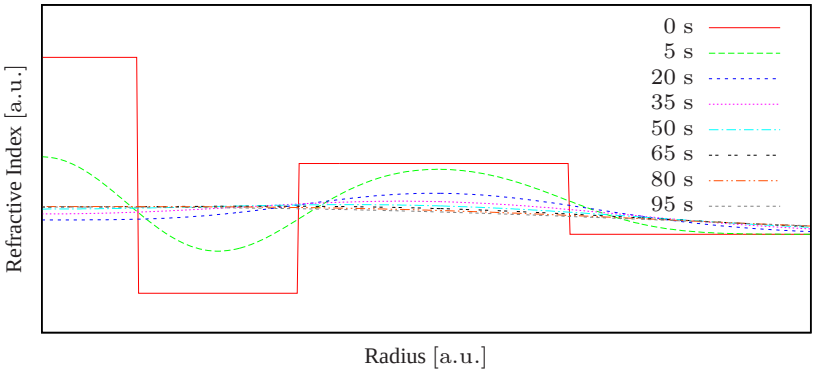

(b) LSF.

Figure 4.22: The refractive index-profiles of the mode-converter fibre and the LSF at selected sample points of the diffusion process. The input refractive index-profile is approximated by the step equivalent to ease the computational load.

a very broad core, however, the transverse field overlap for the $LP_{0,2}$ mode is almost identical in both fibres, which results in the low splice loss at the end of the splice process. The splice evolution shown for the mode-converter fibre and the LSF at a wavelength of 1030 nm is generic for all the combinations of wavelengths and triple-clad structured fibres considered in this project.

There are several experimental challenges for the combine fusion and gas-line-burner splice to work. The fibres cannot be stripped by a mechanical process as this would damage the surface of the fibre [80]. Water by-product from the propane-gas burner would enter the fibres and reduce the strength of the fibres in the splice point, which makes the fibres fragile in the splice point. Therefore, the fibres were heat-stripped and cleaned in an ultra-sonic ethanol bath. It was found that the cleave-angle of the fibres should not exceed 0.5°. The initial alignment in the fusion splicer is critical as a slight off-set would increase the coupling of a symmetric mode, as the $LP_{0,2}$ mode, to a asymmetric mode, as the $LP_{1,1}$ mode. For the best result and to achieve a symmetrical heat zone around the splice point when using the gas-line burner, it is important to precisely align the splice point over the gas-line burner. When suspending the splice point over the gas-line burner, the tension load must not be too high or too low as this could increase the splice loss. Too much tension would cause a tapering of the splice point and too low tension would cause the fibres to deform and bend at the splice point.

The splicing of the mode-converter fibre to the LSF was carried out with an automated splicing-station for the gas-line-burner splice. This reduced the complexity in the splice process as the splicing-station controlled the alignment of the splice point over the flame and the tension load on the fibres. A sketch for the setup for the gas-line burner splice is shown in Fig. 4.23. For the setup a broadband ASE source is used as input. The single-moded output is spliced to the mode-converter fibre with a high coupling efficiency to the fundamental mode. The light is coupled to the LSF. After the light has travelled through the LSF, the light is coupled into the mode-converter fibre, where all the light in the $LP_{0,2}$ is converted into the fundamental mode, which is spliced to a SMF working as a mode-strip for any potential HOMs and therefore this is the only mode detected by the OSA. If some residual $LP_{0,1}$ mode is coupled into the second-mode-converter fibre from the LSF, it will be converted to the $LP_{0,2}$ mode by the LPG and removed by the

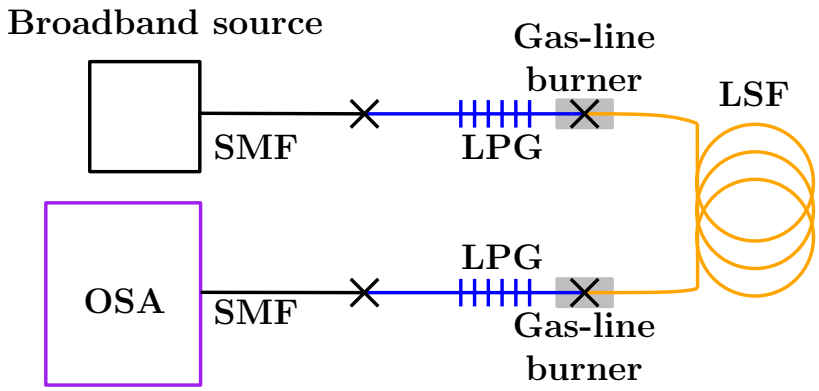

Figure 4.23: A sketch for the setup for the gas-line-burner splice.

mode-strip. As the LPG only converts between the $LP_{0,1}$ mode and the $LP_{0,2}$ mode all other modes are removed by the mode-strip. However, residual light that has not propagated as the $LP_{0,2}$ mode in the LSF can be detected if the light ends up in the $LP_{0,2}$ mode before the final LPG. The source of this is mode coupling at the splice points or distribution along the fibre [81, 82]. The splice points are put over a gas-line burner at the same time and it is assumed that the two splices are identical. Parasitic residual modal content creates a beat pattern on the recorded OSA trace, due to a difference in the optical path length. The residual modal content in a given signal is given by the multi-path interference (MPI) as [62]

$$MPI = 20\log_{10}\left[\frac{1-\sqrt{10^{\frac{-PtP}{10}}}}{1+\sqrt{10^{\frac{-PtP}{10}}}}\right], \tag{4.3.4}$$

where MPI is in dB and PtP is the peak-to-peak difference in the spectrum in units of dB. In Fig. 4.24 the wavelength average transmission and the wavelength average MPI are shown as a function of the experimental run-time. The averaged wavelength interval was from a wavelength of 1025 nm to a wavelength of 1035 nm. The original contour plot of the transmission and the MPI as a function of wavelength and time can be found in App. A.3.1, where the variation with wavelength is observed to be negligible. The first notable difference between the simulated evolution of the loss in Fig. 4.21 and measured transmission in Fig. 4.24 is that the measured transmission oscillates. The simulated splice loss considers only the fraction of light coupled

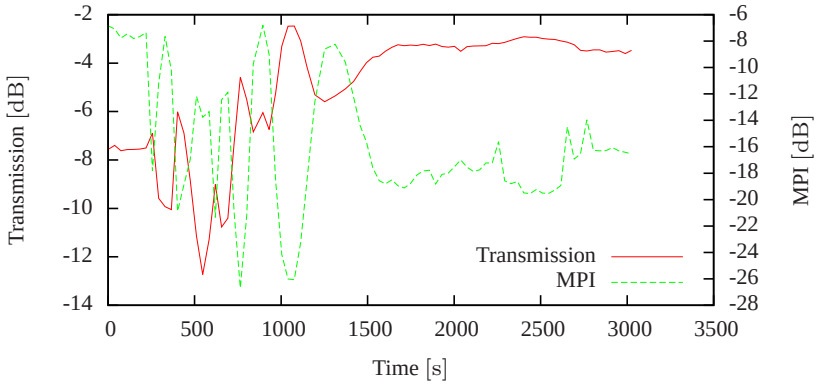

Figure 4.24: The gas-line burner splice evolution for the wavelength average transmission and the wavelength average MPI as a function of the experimental run-time. The length of LSF was 50 m and the resolution of the OSA was 0.02 nm.

from the $LP_{0,2}$ mode in the first fibre to the $LP_{0,2}$ mode in the second fibre. The oscillation in the measurement can be explained by the fact that different mode couplings take place during diffusion of the index profiles and when the light is coupled to the $LP_{0,2}$ mode in the second-mode-converter fibre at the splice point, the light is detected by the OSA, even though that light might not have travelled through the LSF as the $LP_{0,2}$ mode. In Fig. 4.24 it is observed that the minimum loss is reached after an experimental run-time of a 1000 s, however, if the gas-line burners continue to burn, the loss is observed to stabilise at a value of 3.2 dB, which is 0.7 dB larger than the minimum loss. The MPI calculated in a 2 nm bandwidth window is shown in Fig. 4.24. It is observed that the MPI oscillates in the same manner as the transmission and that when there is a low loss, there is also a low MPI. This means that the improvement in the loss is due to better coupling to a single LP mode.

The evolution in the transmission is quite reproducible and it is possible to stop the gas-line-burner splice at the minimum loss region after an experimental run-time of a 1000 s, if the speed at which the gas-line burners are moved away from the splice points is sufficiently slow. This was achieved in Fig. 4.25, where the gas-line burners were moved with an initial speed of 10 $\frac{\mu m}{s}$. Fig. 4.25 shows the wavelength average transmission and the wavelength average MPI as a function of the experimental run-time. The averaged wavelength interval was from

a wavelength of 1025 nm to a wavelength of 1035 nm. The original con-

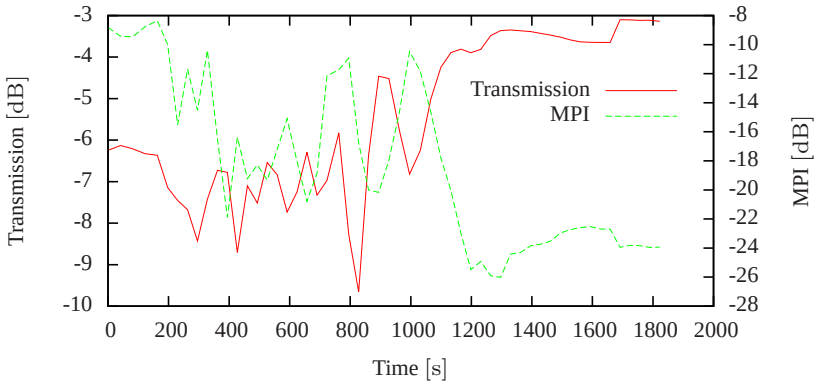

Figure 4.25: The gas-line-burner splice evolution. The splice process is stopped shortly after an experimental run-time of 1000 s and the gas-line burners are moved away. The length of LSF was 70 m and the resolution of the OSA was 0.02 nm.

tour plot of the transmission and the MPI as a function of wavelength and time can be found in App. A.3.1, where the variation with wavelength is observed to be negligible. Comparing Fig. 4.24 and Fig. 4.25 it is observed that the minimum splice of 2.5 dB recorded in Fig. 4.24 is not realised when the splice process is stopped after an experimental run-time of a 1000 s as the recorded loss is 3.1 dB. The gas-line burners have to be lowered, such that the change in the heat zone across the splice point is not abrupt, however, to stop the splice process at the point of minimum loss there is only a relative short time window to lower the gas-line burners. A total loss of 3.1 dB would make each splice loss equal to 1.6 dB if the splices are assumed to be identical. A loss of 1.6 dB is equal to a transmission of 69%. The mode-conversion is to take place just after the amplification of the seed pulse and therefore it should be possible to compensate the splice loss by higher amplification.

There are a lot of parameters that can be varied in this splice process, including the above-mentioned, there is also the initial fusion-splice time, fusion-splice current, and the temperature of the gas-line-burner splice, which can be controlled by adjusting the height of the splice point above the propane flame and also the amount of oxygen added to the combustion process. Another possible parameter is the length of the gas-line burner. With this in mind the applied splice process is hardly optimised. However, due to the complicated required optimisa-

tion process, this was not pursued further in this Ph.D. project.

There are of course alternative approaches by which a low loss might be accomplished. Potentially, the use of one or more bridge fibres could be applied to have a discrete, but gradual change of the transverse field distribution of the considered mode. In line with this another idea could also be to apply a taper to one of the two FMFs to make a slow and adiabatic change of the transverse field distribution of the considered mode, such that it would match the transverse field distribution in the second fibre after which the two fibres are fusion spliced together. A different approach could also be to use free space optics in between the two FMFs to focus the mode to the correct dimension, however, this would compromise the all-fibre integrated laser system.

Chapter 5

Fibre-Based Oscillators

In this chapter two fibre-based oscillators, which both use an ytterbium-doped fibre as the gain medium, are presented. Common for both of the two fibre-based oscillators is that they have been assembled prior to the involvement in this project. The fibre-based oscillator, which is of most importance is the higher-order-mode (HOM) dispersion-balanced laser as this laser is used for the soliton experiments in the left-sided fibre (LSF) and the right-sided fibre (RSF). The second fibre-based oscillator is the all-normal dispersive (ANDi) polarisation-maintaining (PM) laser, which has been the focus of an extensive work regarding modelling mode-lock lasers during the visit to the *Femtosecond Optics Group* at *Imperial College London*. As the ANDi PM laser has no direct relation with what is described in the coming chapters, the laser is placed in the last section of this chapter and can be skipped without any loss of continuity regarding the constructions of the widely tunable femtosecond pulse fibre-based laser system.

5.1 Higher-Order-Mode Dispersion-Balanced Laser

The HOM dispersion-balanced laser was intended to supply the required seed pulses for the experimental soliton self-frequency shift (SSFS) in the LSF and the RSF. To obtain dispersion compensation in a laser operating below the zero dispersion wavelength of silica, it is often accomplished with bulk components. It is also possible to have dispersion compensation by using micro-structure photonic-crystal fibre (PCF),

however, an alternative is to use a HOM module. The HOM module would consist of two mode-converters and an adequate amount of few-moded fibre (FMF) to provide the dispersion compensation. In Fig. 5.1 a sketch is shown of the HOM dispersion-balanced fibre oscillator. The oscillator was originally built by *Kim Giessmann Jespersen* from *OFS Fitel Denmark*. Therefore, the contribution to what is described in this section has been the characterisation of the oscillator and the construction of the amplification chain after the oscillator. The mode-

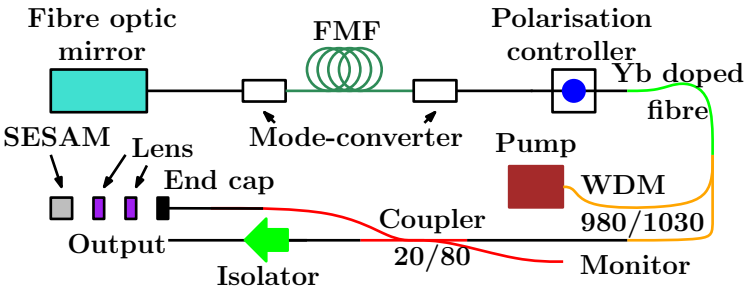

Figure 5.1: Sketch of the HOM dispersion-balanced fibre laser.

locking mechanism is provided by a semiconductor-saturable-absorber mirror (SESAM), which has a centre at a wavelength of 1040 nm, an absorbance of 40%, and a recovery time of approximately 500 fs. The cavity is a linear cavity, where the anomalous dispersion compensation is provided by the HOM module. At the coupler, 20% is coupled out for monitoring and the other 20% arm is used as the output. The laser mode-locks at a repetition rate of 20 MHz. In App. A.4.1 the recorded radio frequency (RF) trace is shown. The total length of the single-mode fibre (SMF) is 2.45 m, which has a group-velocity dispersion value of $-43\ \frac{\text{ps}}{\text{nm km}}$ at a wavelength of 1030 nm. The length of the HOM module is 2.31 m, wherein the mode propagates as the $\text{LP}_{0,2}$ mode, which has a group-velocity dispersion of $54\ \frac{\text{ps}}{\text{nm km}}$ at a wavelength of 1030 nm. The ytterbium-doped gain fibre has a peak absorption of $350\ \frac{\text{dB}}{\text{m}}$ at a wavelength of 980 nm. The length of the fibre is 0.29 m and the group-velocity dispersion is $-70\ \frac{\text{ps}}{\text{nm km}}$ at a wavelength of 1030 nm. Therefore, the total dispersion of the cavity is slightly normal. This is also observed on the recorded spectrum, which is shown in Fig. 5.2. Interferometric ripples are observed on the edges of the spectrum, which is due to the fact that the mode-converters only work in a finite bandwidth region. The spectral full-width at half-maximum (FWHM) is

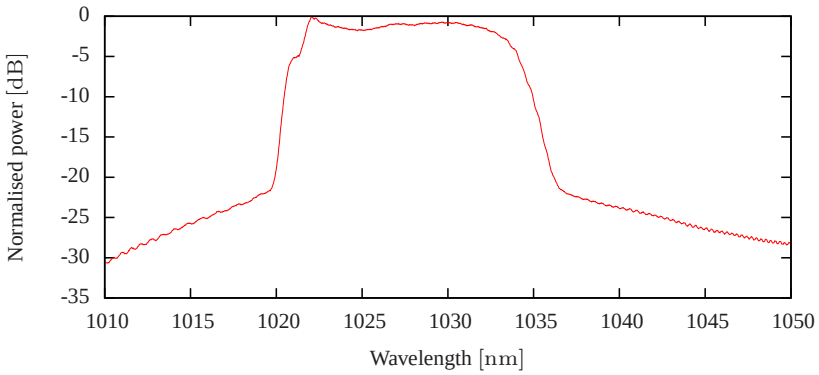

Figure 5.2: Output spectrum of the HOM dispersion-balanced fibre laser.

12.5 nm. The output power of the laser is too low to measure a second-harmonic generation (SHG) intensity autocorrelation. The measured SHG intensity autocorrelation of the amplified seed pulse, which was not unchirped after the amplification process, is shown in Fig. 5.3. The

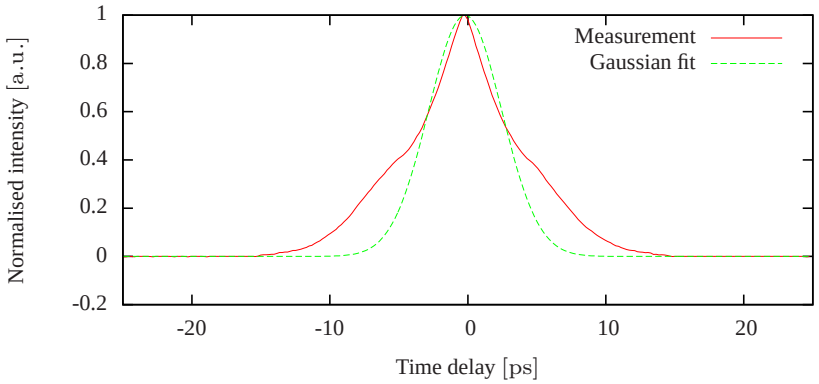

Figure 5.3: Intensity autocorrelation for the HOM dispersion-balanced fibre laser. The output was amplified with a single amplifier to have a detectable SHG signal in the autocorrelator.

retrieved temporal FWHM of the intensity pulse is 4.68 ps from the fitted autocorrelation. From the fitted autocorrelation it is seen that there is some satellite structure in the pulse causing the broadening of the lower part of the autocorrelation. The original seed pulse from the oscillator is assumed to be smaller since the pulse is broadened by the SMF and the ytterbium-doped gain fibre in the amplifier. Fig. 5.4 shows a sketch of the amplification stage for the seed pulse. There are

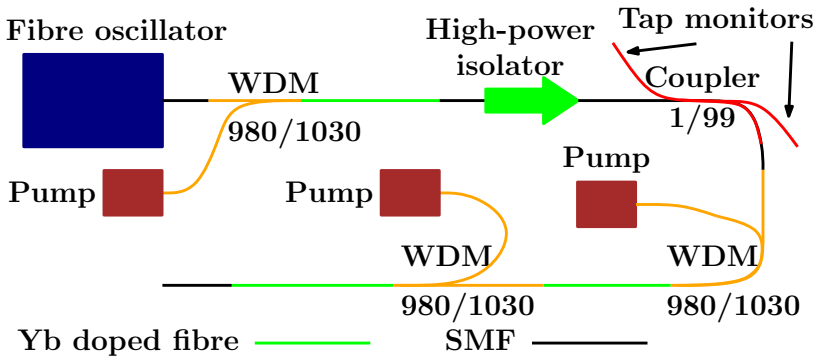

Figure 5.4: Sketch of the amplifier chain to boost the seed pulse from the HOM dispersion-balanced fibre laser.

4.43 m of SMF, including the wavelength-division multiplexer (WDM), between the output coupler and the ytterbium-doped gain fibre in the first amplifier, which has a length of 1.44 m. This is followed by 5.31 m of SMF, which includes the high-power isolator and the tap coupler. The high-power isolator can handle up to 3 W, however, the centre wavelength is at 1064 nm and therefore the isolator has a high insertion loss at a wavelength of 1030 nm. The tap coupler is used to monitor the transmitted and reflected spectra. The second amplifier has an ytterbium-doped gain fibre of 0.50 m. This is followed by 3.32 m of SMF and the third amplifier, which has an ytterbium-doped gain fibre of 0.61 m. The three pumps used in the amplification stage for the seed pulse can each deliver 450 mW of optical power. In Fig. 5.5 the spectrum after each amplifier stage is shown, together with the spectrum from the monitor tap inside the oscillator. The output power after the first amplifier is 19.2 dBm and after the second amplifier the output power is 24.4 dBm. This could have been higher, if the high-power isolator had been centred at 1030 nm. The output power after the third amplifier is 27.7 dBm. All the power measurements were performed at a wavelength of 1030 nm and with a long pass filter with a cut-off edge at 1000 nm in order to remove any residual pump. Under the assumption that the measured average power is contributed only to the pulse, the pulse energy would be 29.4 nJ. However, this assumption might not be valid, considering the measured output spectrum in Fig. 5.5, where outer-band amplified spontaneous emission (ASE) is observed and it is suspected that this is accompanied with ASE generated in-between pulses. The measured SHG intensity autocorrelation after the third

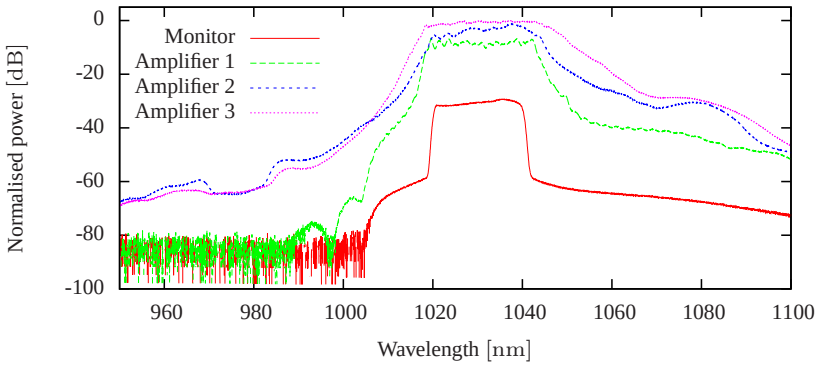

Figure 5.5: The measured spectra after each amplification stage.

amplifier is shown in Fig. 5.6. The output from the amplifier stage was

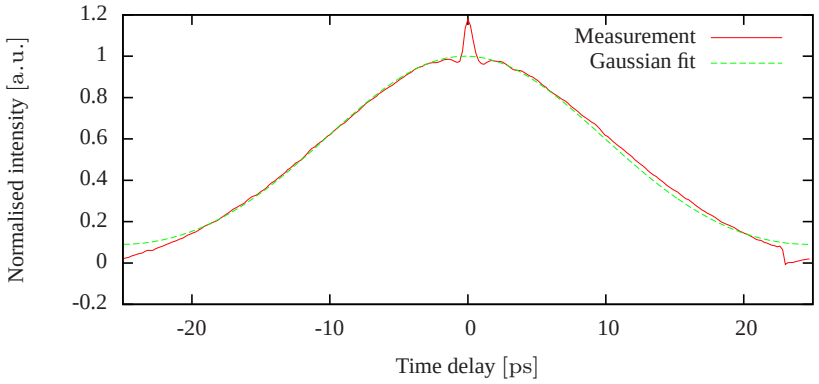

Figure 5.6: Intensity autocorrelation for the HOM dispersion-balanced fibre laser after the third amplifier.

passed through a 20% coupler to reduce power and through a 3 W polarisation sensitive isolator to avoid feedback. The retrieved temporal FWHM of the intensity pulse is 16.8 ps from the fitted autocorrelation. It is observed that the autocorrelation trace has what appears to be a coherence spike on top of the real pulse [83]. This indicates that there is a significant portion of noise in the amplified signal. A more detailed inspection of the autocorrelation trace is shown in Fig. 5.6, where it is observed that the baseline is askew. This is suspected to be either a consequence of the high input-power to the autocorrelator or that the autocorrelation trace is spanning the maximum measurement-time-window of the autocorrelator as this is not apparent in Fig. 5.3.

The amplification is not optimal, due to lack of available components. Ideally, the different amplifier stages should have been separated with isolators and band-pass filters to reduce the ASE. The second and third amplifier stages could also have been placed in a forward and backward configuration if the necessary pump isolators had been available. The third amplifier stage could also have been excluded to give a more optimal amplification, but at a lower average power. However, a more powerful output was preferred over a less noisy output with the anticipation of potential high loss in the splices between the FMFs and the desire to power tune the soliton and thereby the final output of the RSF.

5.2 All-Normal Dispersive Polarisation-Maintaining Laser

The work in this section is based upon [84]. The ANDi PM laser has not been used in any soliton-propagation scheme. However, a more in-depth theoretical understanding of the mode-locking and pulse formation has been obtained for this particular laser. The work regarding this laser was carried out during an external visit to the *Femtosecond Optics Group* at *Imperial College London*. The oscillator was originally built by *Edmund J. R. Kelleher*. Therefore, the contribution to what is described in this section has been the characterisation of the oscillator and the numerical investigation of the mode-locking dynamic of the oscillator. In Fig. 5.7 a sketch is shown of the ANDi PM fibre oscillator. The laser is a standard ring cavity with a single-wall carbon-

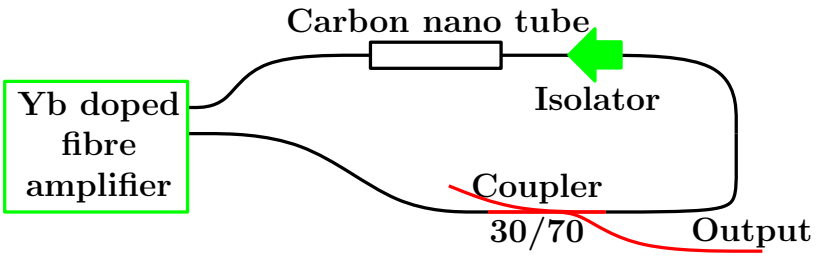

Figure 5.7: Sketch of the ANDi PM fibre laser.

nano-tube as the saturable absorber. Two angle fibre-connectors are mechanically joined in a fibre-mating-sleeve. The carbon-nano-tube is adhered onto with index matching gel on the end-facet of one of the an-

gle fibre-connectors. The absorption and transmission spectra for the carbon-nano-tube are found in App. A.4.2. The ytterbium-doped fibre amplifier is a commercial system. The fibre in the amplifier is a 0.9 m PM double-clad ytterbium gain-fibre, which is pumped by a 4 W multi-mode diode laser at 980 nm. A 30/70 coupler is used to provide the output, where the output is passed through the 70% arm, leaving only 30% inside the cavity. The coupler has a 3 dB transmission bandwidth greater than 150 nm. The isolator enforces a unidirectional cavity. The total length of the passive fibre in the cavity is 5.35 m.

A lot of development on ANDi lasers has been carried out by the group of *Frank Wise* at *Cornell University* and as their emphasis has been on shorter pulse and more energetic lasers, there is often a filter inside in the cavity to confine the spectral broadening generated by the pulses on each round trip [85–88]. However, this is not necessarily a strict requirement if the non-linear phase-shift is kept sufficiently small, i.e. the peak power of the pulse. The ytterbium gain-medium is sufficient for providing the spectral filtering, even though the FWHM gain bandwidth is approximately 55 nm. This leads to formation of so-called "gain-guided" solitons, which previously was demonstrated in the erbium gain-region [89]. Even through the erbium gain-region is smaller than the gain-region of ytterbium, it is still possible to obtain mode-locking, which will be shown in the following.

The measured output spectrum of the laser is shown in Fig. 5.8. The spectrum has a FWHM of 0.15 nm, which indicates that the non-

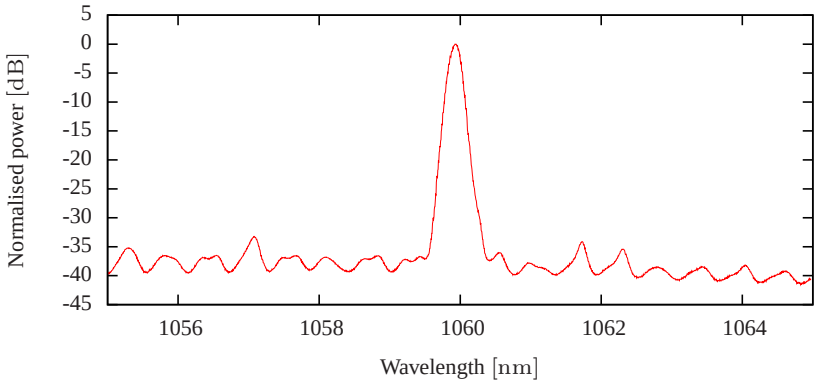

Figure 5.8: Output spectrum, measured with a 0.01 nm resolution.

linear phase-shift around the cavity is small. The output power of the laser was −1.4 dBm. The cavity mode-locks with a repetition rate of

33 MHz. The recorded relative-intensity noise (RIN) measurements are found in App. A.4.2. The measured SHG intensity autocorrelation is shown in Fig. 5.9. The output was amplified to achieve a measurable

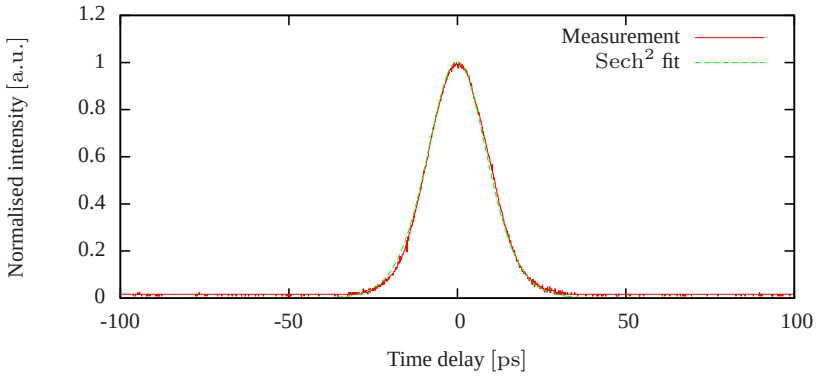

Figure 5.9: Intensity autocorrelation for the ANDi PM laser.

autocorrelation trace. The FWHM of the pulse was 13.9 ps under the assumption of sech^2 intensity profile.

The numerical simulation of the mode-locking dynamics is solved by progression of a pulse around each element of the cavity. This is known as the general round-trip model [83]. The element lay-out of the model is shown in Fig. 5.10. The model shows two possible paths around

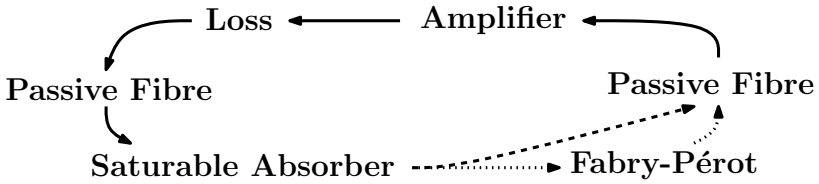

Figure 5.10: Overview of the numerical model, which is based upon the general round-trip model. The path around the cavity without the Fabry-Pérot element is referred to as the path around the standard ring cavity, whereas the other path is referred to as the path around the Fabry-Pérot ring cavity.

the cavity, where the longer path includes a Fabry-Pérot element. The path around the cavity without the Fabry-Pérot element is referred to as the path around the standard ring cavity, whereas the other path is referred to as the path around the Fabry-Pérot ring cavity. The Fabry-Pérot element was introduced later in the process to give an explanation for the small spectral bandwidth of the output pulse and explain the ripples in the background shown in Fig. 5.8.

The numerical scheme is as follows: In each fibre section the Non-Linear Schrödinger Equation (NLSE) is solved and the resulting pulse shape is transferred to the input in the next element. The other elements are represented by transfer functions. The simulation is started from noise. A stable pulse can be obtained after some thousand iterations if the parameters are correct for this type of solution. The Raman effect is disregarded due to the small pulse bandwidth [9]. The simulated pulse is centred at 1060 nm and with a time window of 200 ps divided into 2^{12} points. The parameters for the ytterbium-doped fibre are: length 0.9 m, group-velocity dispersion $\beta_2 = 0.018\ \frac{\mathrm{ps}^2}{\mathrm{m}}$, a parabolic gain with a FWHM bandwidth of 56.8 nm, a small signal gain of 20 dB, an energy saturation of 90 pJ when the Fabry-Pérot element is included, and 60 pJ without the Fabry-Pérot element. The amplifier energy-saturation is related to controlling the pump current in the laboratory. The amplifier has as a non-linear coefficient of $0.003\ \frac{1}{\mathrm{Wm}}$. The loss element includes contributions from the output coupler and the additional losses in the cavity and has a value of 7 dB. The two passive fibre components are identical, with a length of 2.675 m, a group-velocity dispersion $\beta_2 = 0.018\ \frac{\mathrm{ps}^2}{\mathrm{m}}$, and a non-linear coefficient of $0.003\ \frac{1}{\mathrm{Wm}}$. The carbon-nano-tube saturable-absorber is modelled in the limit where the pulse duration is much longer than the phase relaxation time. The modulation depth is 0.10 and the saturation power is 4.2 W when the Fabry-Pérot element is included and 2.3 W without the Fabry-Pérot element. The linear transmission loss of the carbon-nano-tube is 50%, which is based on measurements of a similar carbon-nano-tube saturable-absorber [90]. The Fabry-Pérot element has a reflectivity of 4% and a wavelength spacing between peaks of 1.2 nm. The simulated autocorrelations for the two cases with and without the Fabry-Pérot element are shown in Fig. 5.11. The simulated output pulse has a temporal FWHM pulse duration of 13.9 ps and 14.1 ps with and without the Fabry-Pérot element, respectively. The temporal difference is quite small. The simulated spectra of the two cases are shown in Fig. 5.12. The simulated output pulse has a FWHM spectral bandwidth of 0.60 nm and 0.19 nm for the case without and with the Fabry-Pérot element, respectively. Compared to the temporal difference between the two cases with and without the Fabry-Pérot element, the spectral difference is relatively significantly larger. The simulation with the Fabry-Pérot element is able to reproduce the spectral ripples, which is observed in Fig 5.8. The influence obtained by adding the

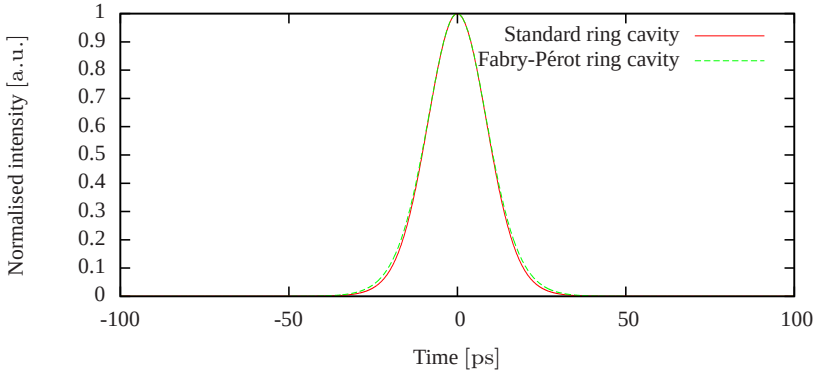

Figure 5.11: The simulated autocorrelations of the cases with and without the Fabry-Pérot element.

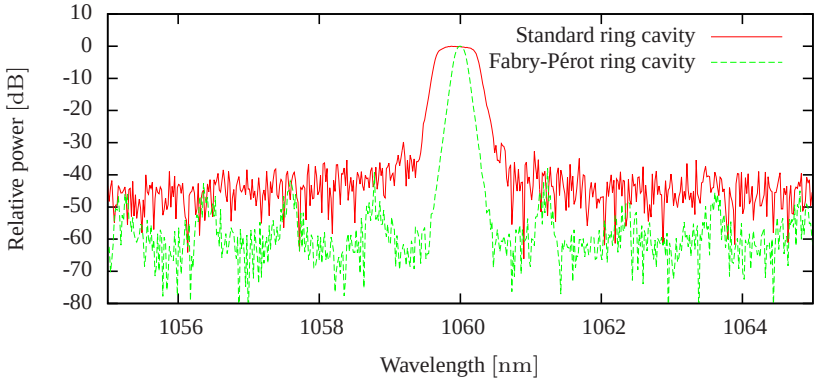

Figure 5.12: The simulated spectrum of the cases with and without the Fabry-Pérot element.

Fabry-Pérot element to the cavity might be small, however, it yields a more accurate numerical representation. In Fig. 5.13 the temporal and the spectral FWHM of the pulse are shown after each element for the converged pulse. The spectral FWHM remains unchanged in the

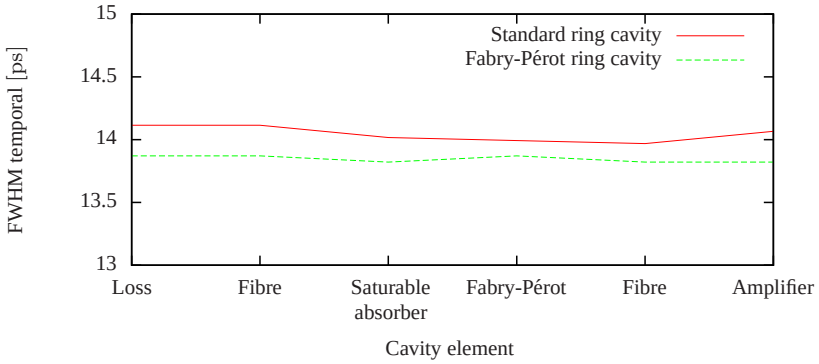

(a) The temporal FWHM of the pulse for both the cases with and without the Fabry-Pérot element.

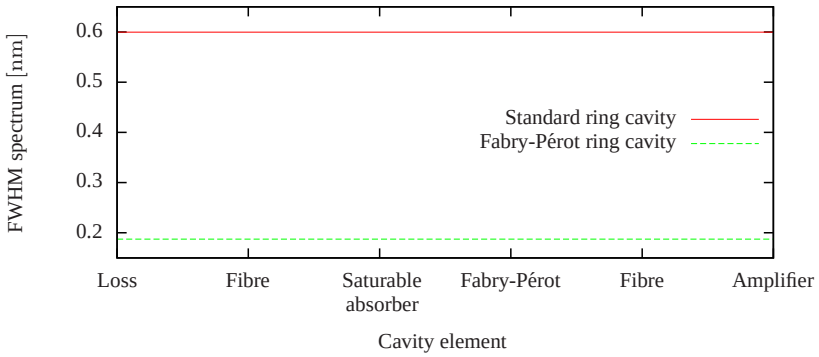

(b) The spectral FWHM of the pulse for both the cases with and without the Fabry-Pérot element.

Figure 5.13: The temporal and spectral FWHM of the pulse after each element at the point where the pulse has converged to a steady state solution.

steady state regime and there are only small variations in the temporal FWHM, which indicates that the pulses are temporal dissipative solitons, which experience only a low non-linear phase-shift.

In the following it is only the standard ring cavity that is considered. The mode of operation for the simulated cavity is presented as the different parameters of the cavity are altered. The resulting outputs from the simulations have been classified numerically to generate a map of the mode of operation of the laser. In Fig. 5.14 there are examples

of the four different classifications, which have been defined. As the

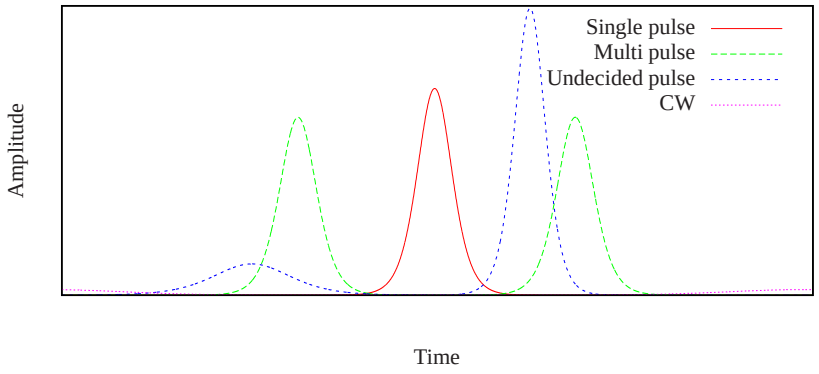

Figure 5.14: Examples of the different pulse type classification used.

classification is performed numerically there are possible errors in the classification scheme, as the classification is based on a simple characteristic of the different pulse types. Another potential error is that the simulation might not have converged to a steady state solution within the maximum allocated number of iterations. In Fig. 5.15 the effect of a filter in the cavity on the mode-locking dynamics is shown. The filter bandwidth is varied along with the amplifier energy-saturation. From Fig. 5.15 it is observed that a narrow band-pass filter has a more distinctive effect on mode-locking dynamics. The filter forces the energy transferred from the amplifier to be limited to a small bandwidth region. The threshold for a multi-pulse solution is lowered. If the filter becomes too narrow, i.e. narrower than approximately 2 nm, more energy is lost in the filter and the multi-pulse threshold increases. As the filter bandwidth is increased, the filter influence becomes less significant as the gain material provides the dominating filter effect, when the filter bandwidth is approximately above 30 nm. In App. A.4.2 more details on the simulation are given in the form of an example of the temporal and spectral FWHM evolution for a converging simulation, together with the final temporal and spectral FWHM values for the filter bandwidth variation. There is also an example where the dispersion of the passive fibres is varied.

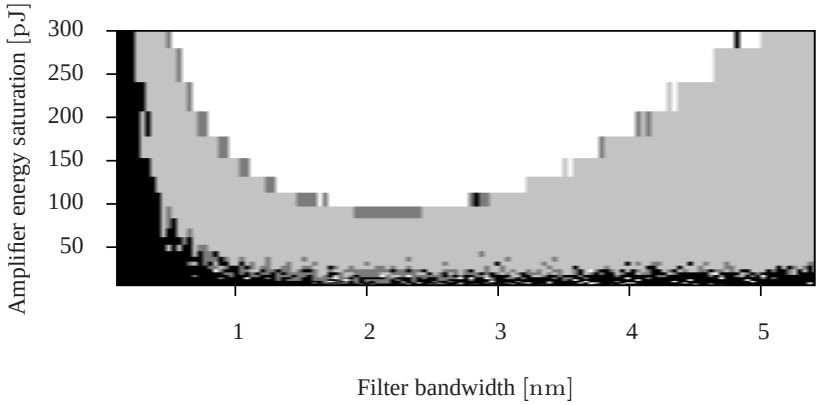

(a) Pulse-type map for a narrow band-pass filter.

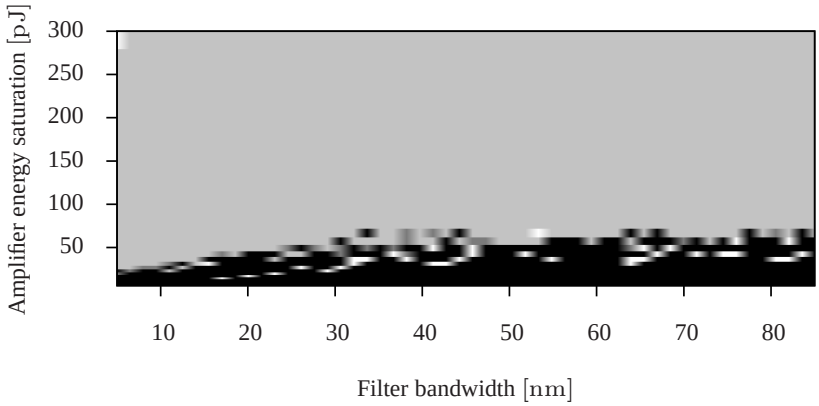

(b) Pulse-type map for a wide band-pass filter.

Figure 5.15: Pulse-type map for a varying filter bandwidth. Examples of the different pulse types are shown in Fig. 5.14. The relation to the grey-scale map is as follows: Black is a CW solution, dark grey is an undecided pulse solution, light grey is single-pulse solution, and white is a multi-pulse solution. The spacing between the steps in the amplifier energy saturation is logarithmic.

Chapter 6

Soliton Self-Frequency Shift

In this chapter the simulated and experimentally observed soliton self-frequency shift (SSFS) in the left-sided fibre (LSF) and the right-sided fibre (RSF) are presented. The chapter is divided into two main sections regarding the input pulse to the LSF, which has a significant impact on the experimental outcome of the widely tunable femtosecond fibre laser. For the experiments conducted at *Cornell University* the seed source provided an unchirp femtosecond pulse. In the design process of the LSF and the RSF it was also an unchirp femtosecond pulse that was used as the input pulse. In the experiments conducted at *OFS Fitel Denmark* the seed pulse from the oscillator needed amplification prior to being coupled to the LSF as described in Sec. 5.1. Therefore, the input pulse to the LSF in the experiments at *OFS Fitel Denmark* was a chirped picosecond pulse. It was assumed that the chirped picosecond pulse could be unchirped in the LSF before forming a soliton and therefore the significant difference between the experiments with the unchirped femtosecond pulse and the chirped picosecond pulse would be a longer required length of LSF and a higher input pulse energy in the experiment with the chirped picosecond pulse.

In the following it is an advantage to be familiar with the basic principal of SSFS process and the coupling of light from the soliton to a dispersive wave in the normal dispersion region via the intramodal Čerenkov process. As an option for the reader an introduction to these concepts are presented for a single-moded highly non-linear fibre (HNLF) in App. B.

6.1 Femtosecond Input Pulse

In this section the simulated and experimentally observed SSFS in the LSF and the RSF are presented for an unchirped femtosecond input pulse. First the simulated SSFS in the LSF and the RSF is presented for the initial design concept, where the input pulse to the LSF is an unchirped femtosecond pulse with a centre wavelength of 1064 nm. Thereafter, the experimentally observed SSFS with an unchirped femtosecond pulse is presented.

6.1.1 Simulated Soliton Self-Frequency Shift

During the design of the LSF and the RSF a femtosecond pulse centred at a wavelength of 1064 nm was used as the input pulse to the LSF. For the simulation presented in this section the following parameters were used. The numerical simulation is started with a pump pulse in the $LP_{0,2}$ mode at a centre wavelength of 1064 nm and vacuum noise in all the other frequency bins. The number of points used on the time/frequency grid is 2^{14}, the time discretisation is 5 fs, the centre wavelength of the simulation window is 950 nm, the shape of the input pulse intensity is a sech^2, the temporal full-width at half-maximum (FWHM) of the pulse intensity is 400 fs, the input peak power of the pulse is 24.5 kW, the intensity-dependent refractive index of the fibre is $2.55 \times 10^{-20}\ \frac{\text{m}^2}{\text{W}}$, the f_R ratio is 0.18 and the loss is neglected. The simulation is done with the Fourth-Order Runge-Kutta in the Interaction-Picture (RK4IP) method [42] and the efficient adaptive step size method [91], with a local error limit of 10^{-7} for the conserved quantity, which is proportionally to the photon number. The length of the LSF and the RSF in the simulation was 19 cm and 8.5 cm, respectively. The simulation is only considering intramodal non-linear effects. The simulation through the section of LSF is shown in Fig. 6.1. The output from the LSF is used as input for the RSF. In this case there is no added splice loss between the LSF and the RSF. The simulation through the section of RSF is shown in Fig. 6.2. The soliton pulse in the output spectrum from the RSF has a pulse energy of 5.1 nJ at a centre wavelength of 1277 nm and the temporal FWHM of the intensity pulse is 15 fs. This is corresponding with the design criteria for the widely tunable femtosecond fibre laser.

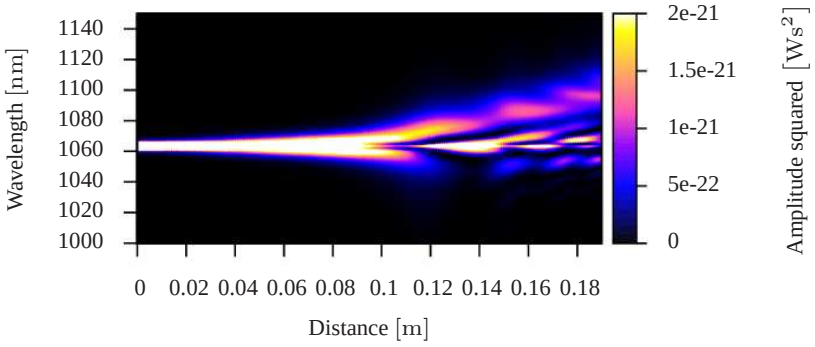

(a) The spectral evolution is shown as a contour plot of wavelength and longitudinal position in the fibre. The soliton is observed to SSFS to the transfer wavelength of 1100 nm.

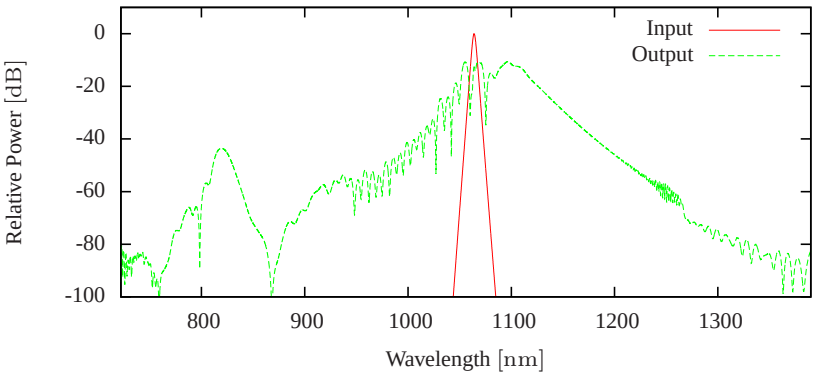

(b) Comparison of the input and the output spectra. In the output spectrum the soliton has shifted to the transfer wavelength of 1100 nm. Light generated by the intramodal Čerenkov process is observed at a wavelength of approximately 820 nm in the output spectrum.

Figure 6.1: Simulated pulse propagation in the LSF with an unchirped femtosecond pulse as the input pulse. The corresponding temporal evolution is shown in App. A.5.1.

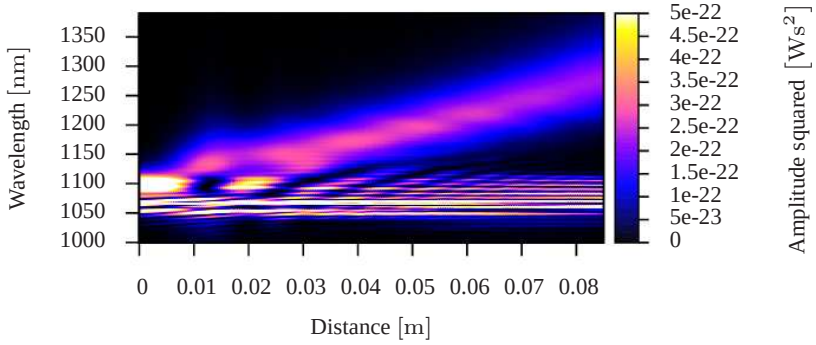

(a) The spectral evolution is shown as a contour plot of wavelength and longitudinal position in the fibre. The soliton is observed to SSFS to a wavelength of 1280 nm.

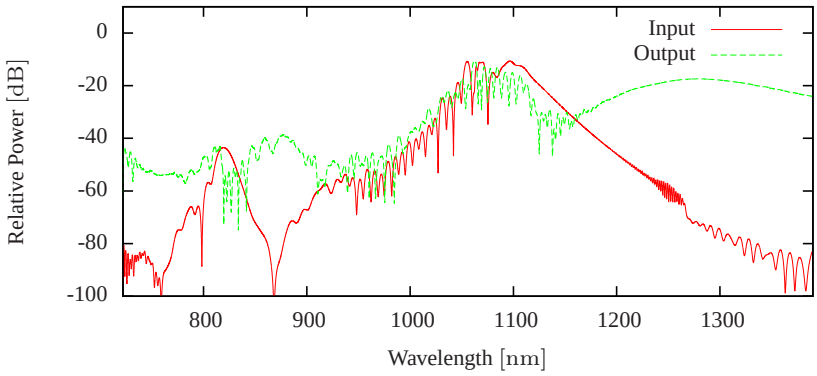

(b) Comparison of the input and the output spectra.

Figure 6.2: Simulated pulse propagation in the RSF with an unchirped femtosecond pulse as the input pulse to the LSF. The corresponding temporal evolution is shown in App. A.5.1.

6.1.2 Experimentally Observed Soliton Self-Frequency Shift

The work in this section is based upon [60, 61]. In the experiments conducted at *Cornell University* the LSF was pumped with a femtosecond pulse. The results presented in this section are performed with a laser system centred at wavelength of 1045 nm.

The laser system with a centre wavelength of 1045 nm is an *IMRA FCPA μJewel* laser system. The temporal FWHM of the input pulse intensity is approximately 400 fs. The repetition rate of the laser is 1 MHz. The free-space output of the laser is attenuated before being coupled into the LSF. The input pulse energy into the LSF was 23 nJ and the length of the LSF was 25 cm. The measured output spectrum is shown in Fig. 6.3. As the LSF supports multiple modes

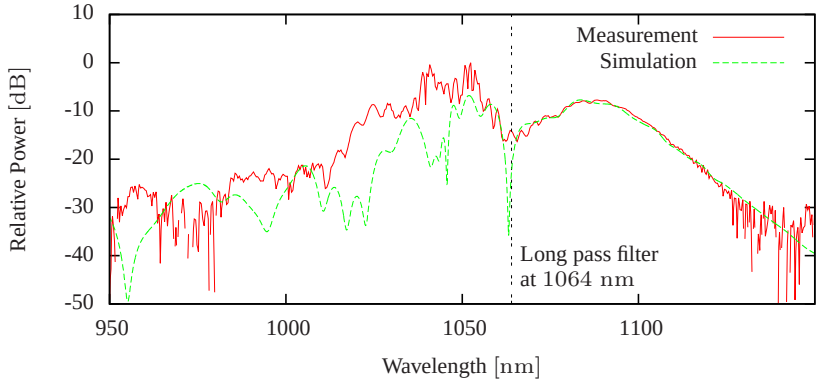

Figure 6.3: The measured and simulated spectra for 25 cm of LSF, with a femtosecond source. The input pulse energy is 23 nJ into the fibre, however, not all of the energy is coupled into the $LP_{0,2}$ mode.

and the pulse is coupled in from free space, only a fraction of the pulse energy is coupled into the $LP_{0,2}$ mode. In Fig. 6.3 the spectrum from an intramodal simulation of the soliton propagation in the $LP_{0,2}$ mode is shown together with the measured spectrum. The pulse energy of the input pulse was used to fit the simulated spectrum of the soliton to the experimental spectrum. The fraction of pulse energy in the $LP_{0,2}$ is determined from the ratio between the simulated pulse energy and the measured total pulse energy, which is 48%. The $LP_{0,2}$ mode is the only propagating mode with anomalous dispersion and therefore the only mode that supports a soliton pulse and the subsequent SSFS. From Fig. 6.3, it is observed that the soliton has red-shifted to a centre wave-

length of 1085 nm. The energy of the soliton is retrieved by measuring the power out of the fibre through a long-pass filter with a band edge at 1064 nm. This results in a soliton energy of 6.3 nJ, which is approximately 6 times higher than the previous record in a solid-core fibre at wavelengths below 1300 nm [30]. Even though this originally was not intended in the design application, the LSF in this experiment provided a higher pulse energy for the considered tuning range with femtosecond pulse operation than current ytterbium fibre-laser systems [92, 93].

The laser system centred at wavelength of 1045 nm had to undergo repair before any consolidating experimental verification of the cascade experiment with the LSF and the RSF was obtained. However, at the moment of writing this thesis promising results for the cascade experiment with the LSF and the RSF using a femtosecond laser system centred at a wavelength of 1030 nm has been achieved, however, this in not included in this thesis.

6.2 Picosecond Input Pulse

In this section the simulated and experimentally observed SSFS in the LSF and the RSF are presented for a chirped picosecond input pulse. First the simulated SSFS in the LSF and the RSF is presented, where the input pulse to the LSF is a chirped picosecond pulse with a centre wavelength of 1030 nm. Thereafter, the experimentally observed SSFS with a chirped picosecond pulse is presented.

6.2.1 Simulated Soliton Self-Frequency Shift

The simulation parameters used for the chirped picosecond input to the LSF are the same as presented in Sec. 6.1.1 expect for the following parameters. The number of points used on the time/frequency grid is 2^{15}. The initial pulse has a centre wavelength of 1030 nm, the temporal FWHM of the pulse intensity is 800 fs, and the input peak power of the pulse is 250 W. Vacuum noise is added to all the other frequency bins. In an attempt to recreate the chirp of the pulse used in the experiment, the initial pulse is propagated through a numerical amplification stage, which is similar to the amplification stage presented in Sec. 5.1. The initial pulse is propagated through 4.4 m of single-mode fibre (SMF), then the output is point-amplified with a factor of 10 in power, before the pulse is propagated through 6.7 m of SMF, after which the output

is point-amplified with a factor of 4 in power, before the pulse is propagated through 3.8 m of SMF, after which the output is point-amplified with a factor of 2 in power, before the is propagated through 0.6 m and finally the pulse is propagated through a numerical representation of the mode-converter fibre. The final pulse energy after the amplification process is 18.2 nJ. The length of the LSF and the RSF in the simulation is 5.5 m and 19 cm, respectively. The simulation through the section of LSF is shown in Fig. 6.4. The output from the LSF is used as input for the RSF. In this case there is no added splice loss between the LSF and the RSF. The simulation through the section of RSF is shown in Fig. 6.5. The soliton pulse in the output spectrum from the RSF has a pulse energy of 3.5 nJ at a centre wavelength of 1288 nm and the temporal FWHM of the intensity pulse is 17 fs. The energy transfer the to soliton pulse in the LSF is less efficient in the case of a chirped picosecond pulse input than compared to the case of an unchirped femtosecond pulse. With increased amplification of the pulse energy, it should be possible to obtain similar results with the chirped picosecond pulse compared to the unchirped femtosecond pulse used in the design process.

6.2.2 Experimentally Observed Soliton Self-Frequency Shift

The simulation with a chirped picosecond pulse indicates that the required length of the LSF should be longer for the chirped picosecond pulse case to de-chirp the pulse before forming a soliton, when compared to the length of the LSF in the case of an unchirped femtosecond pulse.

The LSF was spliced to the mode-converter fibre as described in Sec 4.3.2, with an assumed splice loss of 1.6 dB. The mode-converter fibre was spliced to the output of the amplification stage with negligible loss. In Fig. 6.6a the recorded spectrum with 100 m of LSF is shown as a function of amplifier-current to the third amplifier. The currents of the two other amplifier pumps were kept fixed. The soliton is observed to slowly shift as the amplifier current is increased toward the maximum value. However, the SSFS seems to halt before the soliton has clearly split of the input pulse and light is generated approximately at a wavelength of 1150 nm. This is shown in more details in Fig. 6.6b, where the spectra for three selected amplifier-currents from Fig. 6.6a are presented. There is a striking similarity to the cancellation of the

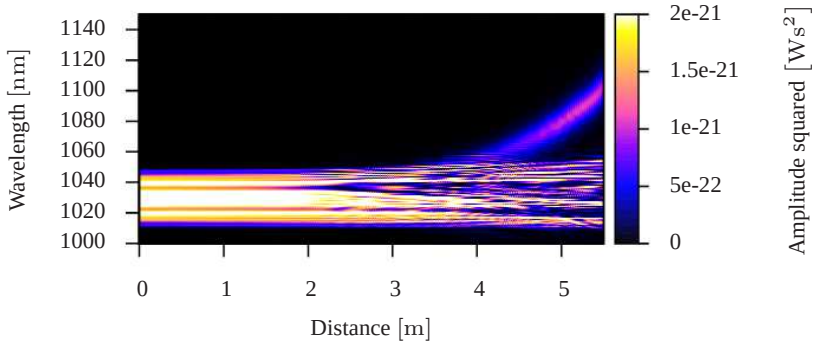

(a) The spectral evolution is shown as a contour plot of wavelength and longitudinal position in the fibre. The soliton is observed to SSFS to the transfer wavelength of 1100 nm. To compensate for the chirped before forming a soliton pulse the length of the LSF is longer than for the case with an unchirped femtosecond pulse.

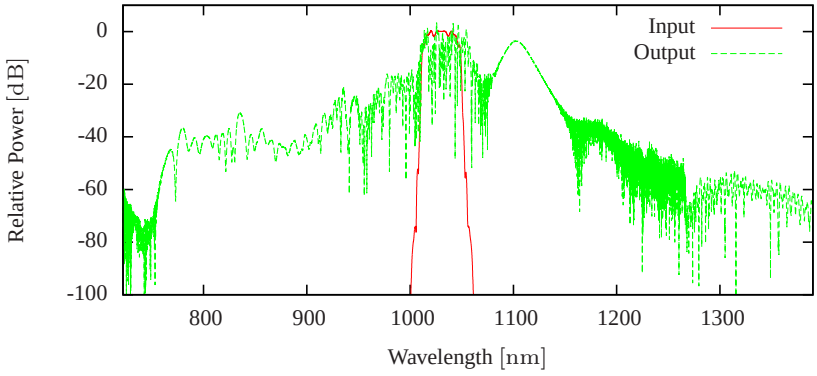

(b) Comparison of the input and the output spectra. The input spectrum resembles the measured spectrum without the outer-band ASE in Fig. 5.5.

Figure 6.4: Simulated pulse propagation in the LSF with a chirped picosecond pulse as the input pulse. The corresponding temporal evolution is shown in App. A.5.2.

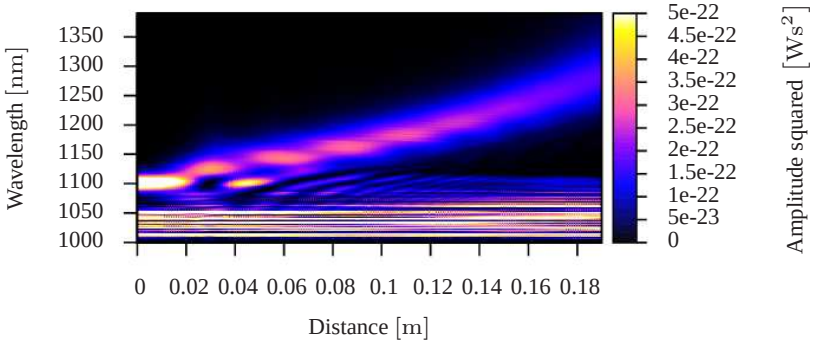

(a) The spectral evolution is shown as a contour plot of wavelength and longitudinal position in the fibre. The soliton is observed to SSFS to a wavelength of 1280 nm.

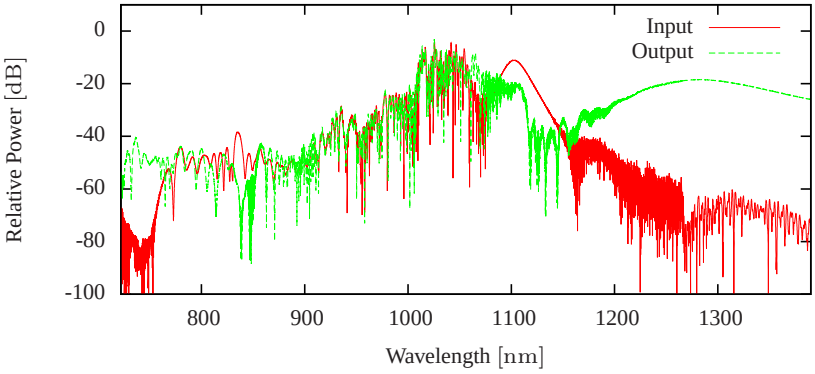

(b) Comparison of the input and the output spectra.

Figure 6.5: Simulated pulse propagation in the RSF with a chirped picosecond pulse as the input pulse to the LSF. The corresponding temporal evolution is shown in App. A.5.2.

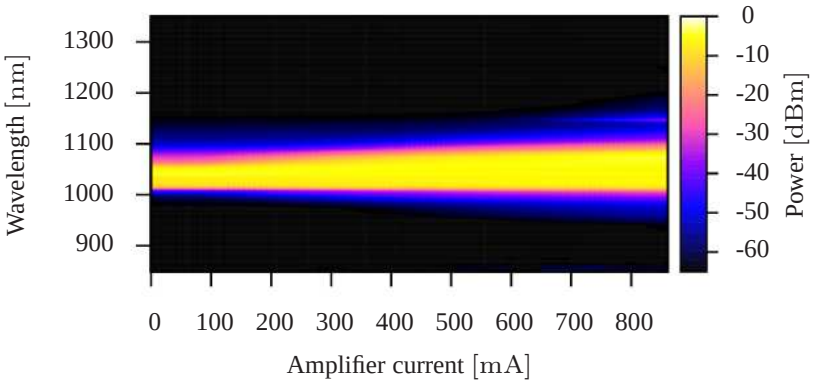

(a) The spectral evolution is shown as a contour plot of wavelength and current to the third amplifier pump in the fibre.

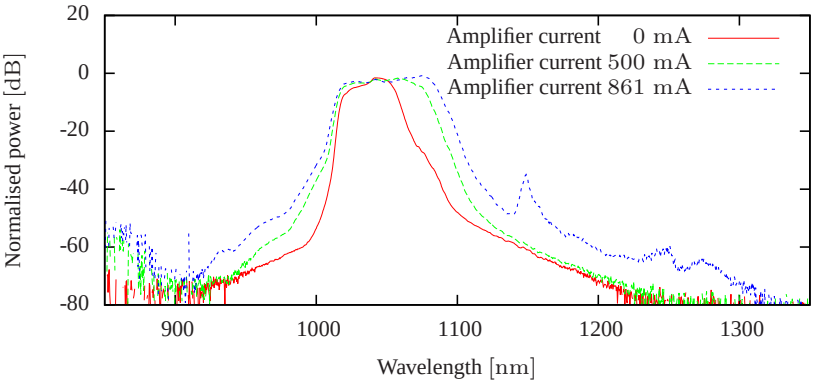

(b) The spectra for three amplifier-currents emphasising the halt of SSFS.

Figure 6.6: The measured SSFS in 100 m of LSF with the HOM dispersion-balanced seed laser.

SSFS and the generation of dispersive wave in the normal dispersion region by the intermodal Čerenkov process, however, as Fig. 4.5a shows the dispersion is anomalous in this region for the $LP_{0,2}$ mode in the LSF. The generation of light at a wavelength of 1150 nm and the halt of the SSFS is in fact an intermodal Čerenkov process. The light of the soliton in the $LP_{0,2}$ mode is coupled to a dispersive wave in the $LP_{1,1}$ mode, when the fibre is bent, this complicates matters as the length of the LSF is 100 m and therefore the fibre is placed on a spool. The intermodal Čerenkov process is treated in more detail in Sec. 7.2. If the spectral FWHM of the soliton at a amplifier current of 861 mA is determined by measuring the half-width at half-maximum on the longer wavelength side, a FWHM bandwidth of 16 nm is obtained. If the soliton is assumed Fourier transform limited, then the temporal FWHM of the pulse intensity is 153 fs. In Fig. 6.7 the measured second-harmonic generation (SHG) intensity autocorrelation is shown. In order to record the autocorrelation a core-less fibre serving as an end-cap was spliced to the end of the LSF to reduce the back-reflected power. The core-less fibre was cleaved under a microscope to provide a short length of roughly 100 μm. The trace of the autocorrelation has some structure at the

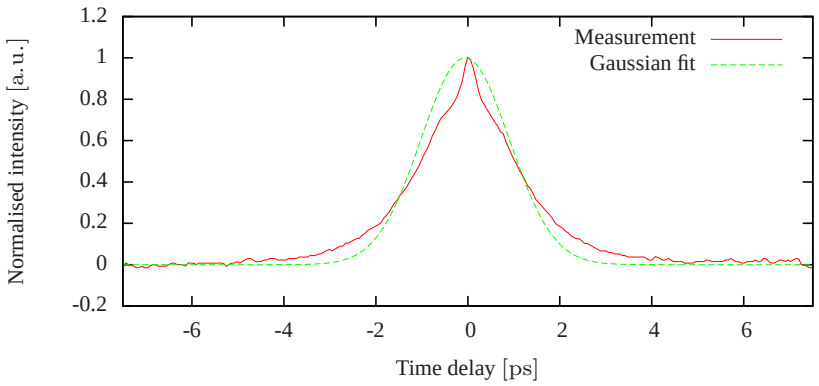

Figure 6.7: Intensity autocorrelation from the output of the 100 m of LSF.

peak. If a Gaussian intensity profile is used to fit the autocorrelation, a temporal FWHM of the pulse intensity of 1.65 ps is obtained. This is a factor of 10.8 larger than the value obtained from the spectrum. This is because the structure on top of the autocorrelation trace is the soliton and the rest of the trace is caused by the dispersive wave. The top of the autocorrelation was measured with a finer time resolution, which is shown in Fig. 6.8. The top structure of the autocorrelation fits a sech^2

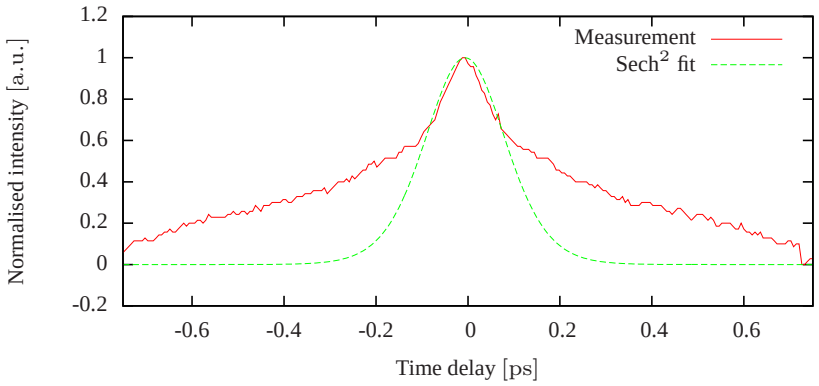

Figure 6.8: Intensity autocorrelation for the output of the 100 m of LSF, with a femtosecond resolution.

intensity profile well, which agrees with the assumption that this is a soliton. From the fit the FWHM of the pulse in the temporal domain is 144 fs, which is almost the same value retrieved from the spectrum. The soliton pulse energy is calculated from the pulse width retrieved from the autocorrelation, a pulse energy of 2.6 nJ is obtained using an intensity-dependent refractive index of $2.55 \times 10^{-20} \frac{\mathrm{m}^2}{\mathrm{W}}$, a product between the group-velocity dispersion and the effective area of 25.8 fs, and a wavelength of 1075 nm. The energy conversion efficiency to the soliton is 13%, this under the assumption that the amplified pulse had a pulse energy of 29.4 nJ before the mode-converter fibre and including the splice loss of 1.6 dB between the mode-converter fibre and the LSF. As shown with the simulation of a chirped picosecond pulse in Sec. 6.2.1 the energy conversion efficiency to the soliton pulse is reduced, when compared to the simulation of an unchirped femtosecond pulse in Sec. 6.1.1. The energy conversion efficiency to the soliton pulse in the LSF in the simulation of a chirped picosecond pulse is 27%. The chirped of the experimental input pulse to the LSF is assumed to be greater then expected chirp from the chirped picosecond pulse simulation, due to the required longer length of LSF fibre in the experiment. The larger chirped of the experimental pulse give the lower energy conversion efficiency to the soliton pulse.

A significant observation about the experiment with the femtosecond pulse as input to the LSF compared to the experiment with the chirped picosecond pulse is that the soliton is able to shift to even longer wavelengths with the femtosecond input pulse. This is possible as the

required length of fibre is much shorter and therefore easier to handle and thereby the bending of the fibre can be avoided. When the fibre is kept straight, the SSFS is not limited by the intermodal Čerenkov process. In the experiment with the chirped picosecond pulse it was attempted to get the soliton to shift further by spooling of approximately 15 m of the LSF from the output end of the fibre and placing the 15 m in a large coil, this had no effect of the measured output spectrum of the fibre. No further attempts were performed to avoid the intermodal Čerenkov process by spooling fibre of the spool. The soliton in the LSF do not reach the designed transfer wavelength of 1100 nm due to the intermodal Čerenkov process. This compromise the initial design as the transfer wavelength was to be situated between the mode-crossing wavelength in the LSF and in the RSF. The mode-crossing in the RSF is at a wavelength of 1086 nm and therefore the soliton in the LSF has not shifted far enough. The mode-crossing wavelength is sensitive to small perturbation in the wave-guide design and as the comparison between the calculated and measured absolute group-index difference in Sec. 4.2.1 is not entirely perfect, the mode-crossing wavelength of the RSF is assigned with some uncertainty. Therefore, even though that the soliton in the LSF is at a wavelength shorter than the mode-crossing in the RSF the cascade experiment is still attempted. The simulated splice evolution between the LSF and the RSF is similar to one shown in Sec. 4.3.2, however, a perfect physical coupling between the fibres should also produce a low splice loss of approximately 0.7 dB at the original design transfer wavelength of 1100 nm. The splice loss reduces slightly at the wavelengths of interest below 1100 nm. The LSF and the RSF was spliced with a fusion process and a combination of a fusion and gas-line-burner process, however, no significant change in the output spectrum was observed. The gas-line-burner process was performed with a no-automated setup. The no-automated automated gas-line-burner setup, opposed to the automated gas-line-burner setup described in Sec. 4.3, could be move to the physical location of the laser setup. The quality of the splice between the LSF and the RSF during the gas-line-burner splice was determine by observing the shift of the soliton of the output spectrum from the RSF while the laser system was on. As a last resort the LSF and the RSF were physically coupled in a fusion splicer with a drop of index matching oil on the end of one of the fibres to avoid a strong Fresnel reflection from a silica-air interface. With the manual alignment control of the fibres the coupling to the

$LP_{0,2}$ mode in the RSF was attempted to be optimised. Once again no soliton shift to longer wavelengths was observed. It is expected that the missing SSFS in the RSF is due to the position of the mode-crossing. As the mode-crossing wavelength is sensitive to small perturbation in the wave-guide design, there is a section of the drawn RSF, which has a mode-crossing located at a wavelength of 1055 nm. This is in the following denoted as the shorter mode-crossing wavelength variation of the right-sided fibre (SMCW-RSF). The effective indices for the first few guided modes in the SMCW-RSF are shown in Fig. 6.9 As the mode-

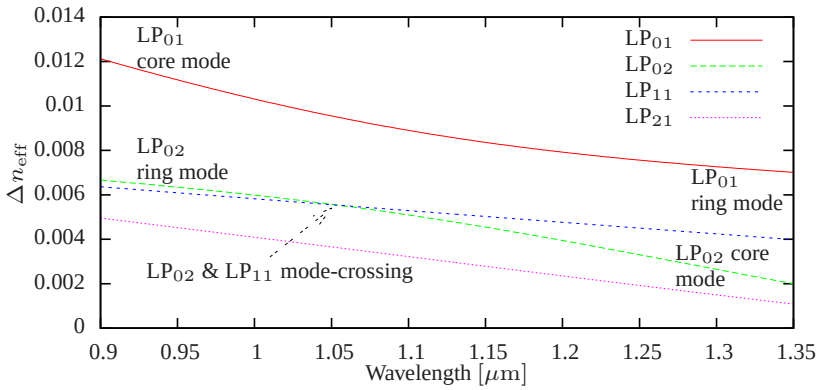

Figure 6.9: The effective indices of the first four LP modes in the SMCW-RSF, with respect to pure silica.

crossing is located at a shorter wavelength in the SMCW-RSF compared to the RSF the anomalous dispersion region is also shifted to shorter wavelength, which limits the bandwidth of the SSFS. In Fig. 6.10a the recorded spectrum with 75 m of LSF fusion spliced with cold splice to 1.5 m of SMCW-RSF is shown as a function of amplifier-current to the third amplifier. The currents of the two other amplifier pumps were kept fixed. The soliton is observed not to shift and remains halted at a centre wavelength of 1075 nm. In Fig. 6.10b the spectra of three selected amplifier-currents are shown. The most significant difference between the recorded spectra out of the LSF and the SMCW-RSF is that the baseline for the longer wavelengths of the output spectrum of the SMCW-RSF has increased. It is difficult to give the exact explanation for this, however, it is speculated that this is caused by four-wave mixing (FWM). The splice between the LSF and the SMCW-RSF was performed with different variations of both the fusion splice process and the combined fusion and gas-line-burner process, however, none of the

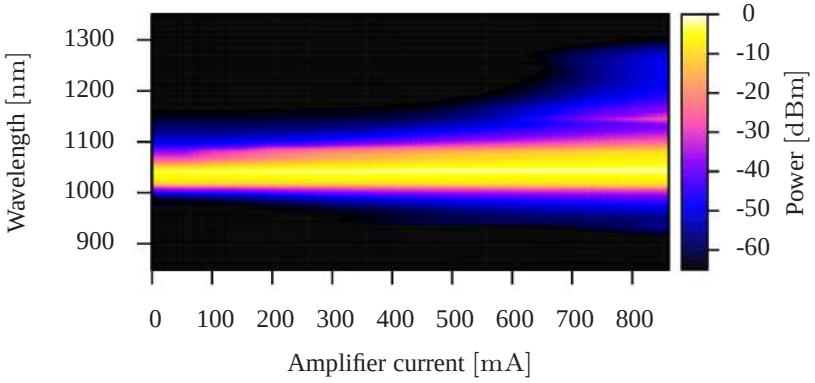

(a) The spectral evolution is shown as a contour plot of wavelength and current to the third amplifier pump in the fibre.

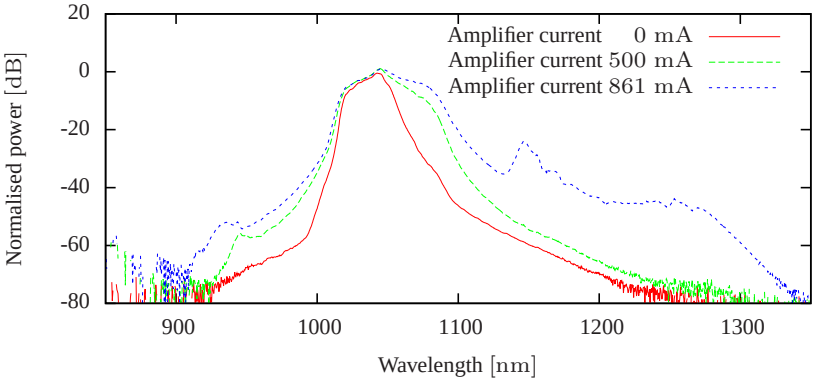

(b) The spectra from three amplifier currents emphasising the missing SSFS to the longer wavelengths.

Figure 6.10: The measured SSFS in 75 m of LSF spliced together with 1.5 m of SMCW-RSF with the HOM dispersion-balanced seed laser.

variations facilitated a shift of the soliton to the longer wavelengths in the SMCW-RSF. A simulation of the expected behaviour for the SSFS in the SMCW-RSF is shown in Fig. 6.11. The input pulse to the 1.5 m of SMCW-RSF is a soliton with a temporal pulse intensity FWHM of 144 fs and centred at a wavelength of 1075 nm, as measured out of the 100 m of LSF. It is assumed that the soliton in the 75 m of LSF and the 100 m of LSF is similar as both solitons are halted by the mode-crossing and the intermodal Čerenkov process at the same wavelength. The pulse energy is varied to anticipate for a unknown splice loss. The

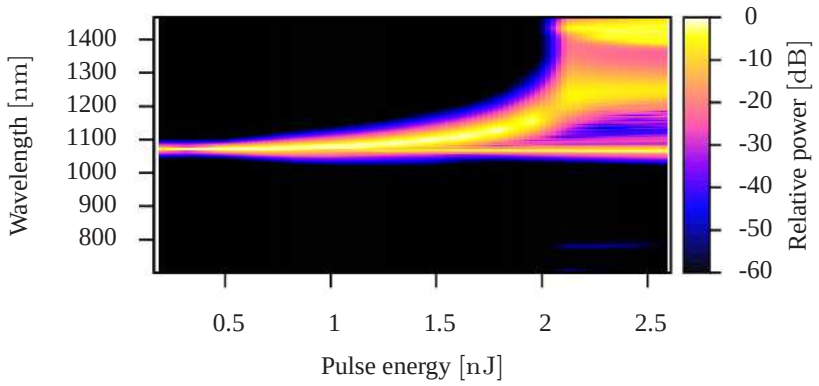

Figure 6.11: The simulated SSFS in 1.5 m of SMCW-RSF. At an input pulse energy of 2 nJ the SSFS is halted by an intramodal Čerenkov process at a wavelength approximately of 1250 nm.

maximum value corresponds to the estimated pulse energy for the soliton in the 100 m of LSF. From the simulation it is observed that even for a reasonable splice loss it should have been possible to observe the SSFS in the SMCW-RSF. However, this was not the case and a possible explanation is that the index difference between the $LP_{0,2}$ mode and the $LP_{1,1}$ mode remains small over a broad wavelength region around the mode-crossing of the $LP_{0,2}$ mode and the $LP_{1,1}$ mode, which is shown in Fig. 6.9. This is another consequence of the limitation of the peak value of the group-velocity dispersion curve in the design process. It is suspected that the shift in the position of the mode-crossing in the SMCW-RSF is not enough.

In a final attempt to demonstrate that is was possible to couple the soliton between two few-moded fibres (FMFs), the SMCW-RSF was re-

placed with the mode-converter fibre to facilitate the shift of soliton to longer wavelength. The mode-converter fibre does not have any mode-crossing close to the transfer wavelength, however, the product of the group-velocity dispersion and the effective area is smaller than in the RSF, hence the soliton energy is lower. The LSF and mode-converter fibre was spliced with a fusion process and a combination of a fusion and gas-line-burner process and again no significant change in the output spectrum was observed. Without monitoring the splice quality the automated gas-line-burner setup was also utilised to splice the LSF and mode-converter fibre with a heat exposure longer than 1000 s. It was a surprise that this splice also failed to couple the soliton from the LSF to the mode-converter fibre, as the splice procedure was identical for the splice of the mode-converter fibre to the LSF at the wavelength of 1030 nm. As described in Sec. 4.3 the index profile after the gas-line-burner process should be a broad core with a small index difference with respect to the cladding for both fibres, which in theory should make the splice loss less dependent of the wavelength. It should be noted that this was only attempted once as this was one of the last experiments performed during the Ph.D. project.

The experimental demonstration of the widely tunable femtosecond fibre laser with the chirped picosecond input pulse to the LSF fails as the soliton shift in the LSF is halted by the intermodal Čerenkov process. The intermodal Čerenkov process occurs as the required length of LSF, to de-chirp the input pulse before the soliton is formed, is too long for the fibre not to be coiled. The SSFS in the LSF is halted by the intermodal Čerenkov process at a wavelength shorter than the intended transfer wavelength of the design and the wavelength of the mode-crossing in the RSF. To compensate for this the SMCW-RSF is used instead of the RSF. The experiments with the SMCW-RSF showed no sign of a soliton shifted to longer wavelengths. This is either an consequence of that the index difference between the $LP_{0,2}$ mode and the $LP_{1,1}$ mode remains small over a broad wavelength region around the mode-crossing of the $LP_{0,2}$ mode and the $LP_{1,1}$ mode, which couples the light of the soliton in the $LP_{0,2}$ mode to the $LP_{1,1}$ mode in the SMCW-RSF or that there is an unresolved problem with the splice process. As it was not possible to substitute the RSF with the mode-converter fibre for achieving the soliton shift to longer wavelengths, it is suspected that there is an unrealised issue with the splice from the LSF the other fibres. As these results were the final experimental

results obtained during the Ph.D. project there was not enough time to investigate the splice problem any further.

Chapter 7

Intermodal Non-Linearities in Few-Moded Fibres

In this chapter the intermodal non-linear effects, which were observed during the Ph.D. project, are described. The intermodal effects were observed in experiments using the left-sided fibre (LSF). The LSF was used to generate intermodal four-wave mixing (FWM) by pumping in the $LP_{0,1}$ mode and generating the idler in the $LP_{0,1}$ mode and signal in the $LP_{0,2}$ mode. Furthermore, an intermodal Čerenkov coupling between a soliton in the $LP_{0,2}$ mode and a dispersive wave in the $LP_{1,1}$ mode was generated, when the LSF was bended.

7.1 Four-Wave Mixing

The work in this section is based upon [94–96]. During experiments with the LSF it was discovered that light in the $LP_{0,1}$ mode was able to generate intermodal FWM with an idler in the $LP_{0,1}$ mode and a signal in the $LP_{0,2}$ mode. The results were obtained by using a home-made all-fibre system to provide input pulses to the LSF. The mode-locked fibre laser consists of a seed oscillator at 1064 nm and two ytterbium-doped fibre amplifiers. The output of the fibre laser was a pulse train with an 18.33 MHz repetition rate and a maximum average power of 470 mW. The pulse width was approximately 6 ps. The fibre laser was directly spliced to 1.75 m of LSF. The measured FWM spectrum for a pulse energy of 21 nJ into the LSF is shown in Fig. 7.1a. The input light is coupled into the $LP_{0,1}$ mode and an idler in the $LP_{0,1}$ mode is generated at a wavelength of approximately 940 nm and a signal in the

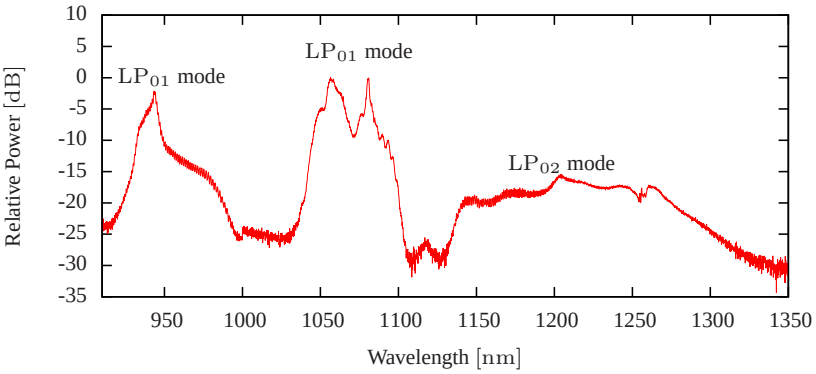

(a) The measured output spectrum.

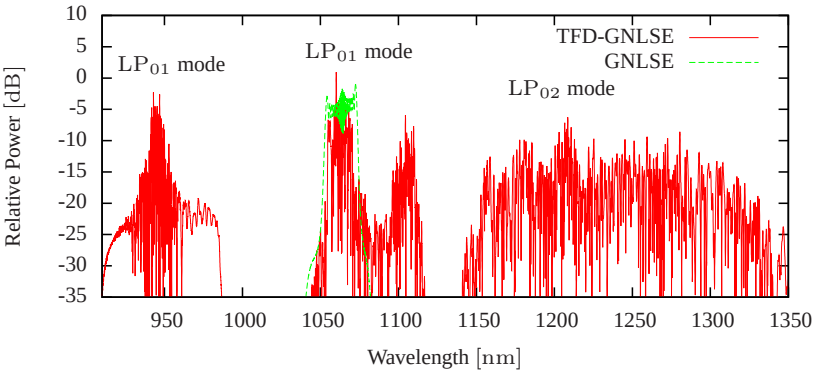

(b) Simulated FWM output spectrum with the TFD-GNLSE and the GNLSE numerical implementations.

Figure 7.1: FWM output spectrum from the experiment in the LSF, with an input pulse energy of 21 nJ.

$LP_{0,2}$ mode is generated at a wavelength of approximately 1200 nm. The theoretical phase-matching curve for the FWM process, where a degenerated pump in the $LP_{0,1}$ mode at a wavelength of 1064 nm is used to generate an idler in the $LP_{0,1}$ mode and a signal in the $LP_{0,2}$ mode is shown in Fig. 7.2, together with the effective area for the FWM process of the four interacting modes. The interaction is phase matched,

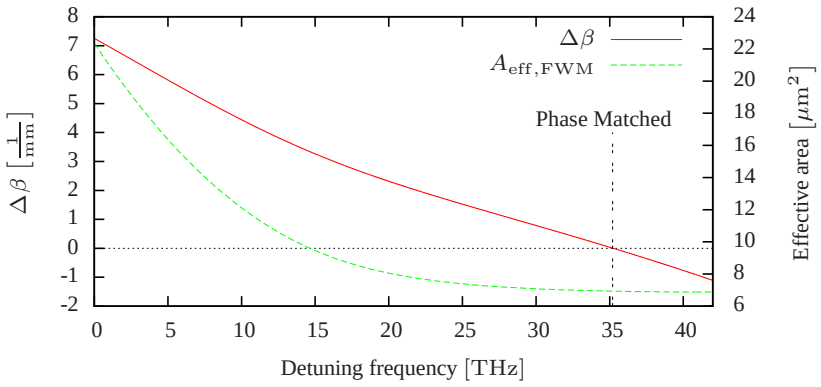

Figure 7.2: The linear phase matching curve together with the effective area for the FWM process with a degenerated pump in the $LP_{0,1}$ mode at a wavelength of 1064 nm and an idler in the $LP_{0,1}$ mode and a signal in the $LP_{0,2}$ mode. The non-linear correction to the phase matching curve is of the order $\frac{1}{\mathrm{m}}$, which make the linear phase matching the dominating part in this case.

when the signal and idler are detuned from the pump by 35.2 THz, which positions the idler and the signal at a wavelength of 945 nm and 1216 nm, respectively. The linear phase mismatch parameter is given as

$$\Delta\beta = 2\beta_{0,1}\left(\omega_\mathrm{p}\right) - \beta_{0,1}\left(\omega_\mathrm{p} + \Delta\omega\right) - \beta_{0,2}\left(\omega_\mathrm{p} - \Delta\omega\right), \tag{7.1.1}$$

where $\beta_{i,j}$ is the propagation constant for the $LP_{i,j}$ mode, ω_p is the angular frequency of the pump, and $\Delta\omega$ is the angular frequency detuning between the idler or signal and the pump. The propagation constant is calculated from the theoretical effective index curves shown in Sec. 4.1.1. The effective area for the FWM process shown in Fig. 7.2 is the inverse of the transverse-field overlap, which is given by

$$\begin{aligned} N = &\frac{1}{A_\mathrm{eff,FWM}} = \int_A \tilde{F}_{N,0,1}\left(\omega_\mathrm{p}\right)\tilde{F}_{N,0,1}\left(\omega_\mathrm{p}\right) \\ &\tilde{F}_{N,0,1}\left(\omega_\mathrm{p} + \Delta\omega\right)\tilde{F}_{N,0,2}\left(\omega_\mathrm{p} - \Delta\omega\right)\mathrm{d}A, \end{aligned} \tag{7.1.2}$$

where $\tilde{F}_{N,i,j}$ is the normalised transverse-field distribution, which in this work is purely real, for the $\mathrm{LP}_{i,j}$ mode, $\mathrm{d}A$ is the differential transverse area. Fig. 7.2 shows that the FWM effective area is approximately 7 $\mu\mathrm{m}^2$ for a FWM process that is detuned 35.2 THz from the pump. This means that the FWM process is strong due to the small effective area, which comparable to a micro-structured photonic-crystal fibre (PCF) [27, 28]. The phase-matching curve and the corresponding FWM effective area are only valid for the specific mode configuration and the wavelength of the pump.

By using the framework of the Generalised Non-Linear Schrödinger Equation (GNLSE) given in Sec. 2.2.1 with the fourth-root method to incorporate the dispersion of the effective area [38], then the intermodal effective areas regarding two modes are given as three different intermodal effective areas. In the case of the $\mathrm{LP}_{0,1}$ mode and the $\mathrm{LP}_{0,2}$ the first intermodal combination is $3\times\mathrm{LP}_{0,1}$ and $1\times\mathrm{LP}_{0,2}$, the second intermodal combination is $2\times\mathrm{LP}_{0,1}$ and $2\times\mathrm{LP}_{0,2}$, and the third intermodal combination is $1\times\mathrm{LP}_{0,1}$ and $3\times\mathrm{LP}_{0,2}$. The effective area is calculated as

$$A_{\mathrm{eff}} = \frac{1}{\int_A \tilde{F}_{N,A}(\omega)\,\tilde{F}_{N,B}(\omega)\,\tilde{F}_{N,C}(\omega)\,\tilde{F}_{N,D}(\omega)\,\mathrm{d}A}, \tag{7.1.3}$$

where the modes of the field distribution are A, B, C, and D. In Fig. 7.3 the effective area is shown for the $\mathrm{LP}_{0,1}$ mode, the $\mathrm{LP}_{0,2}$ mode and the three intermodal effective areas for the LSF. Both the effective area of

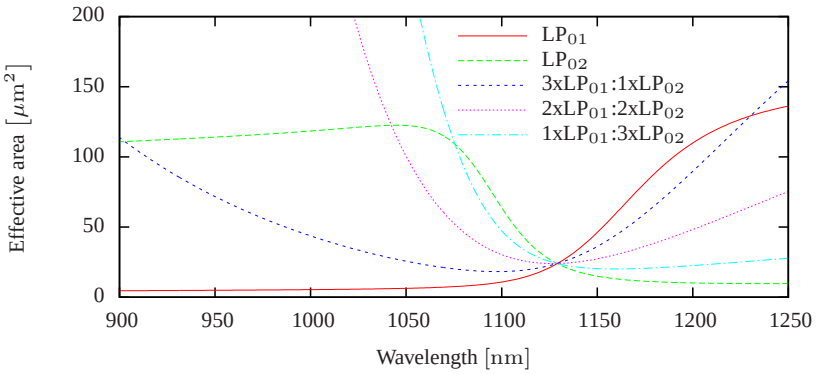

Figure 7.3: The effective areas for the $\mathrm{LP}_{0,1}$ mode, the $\mathrm{LP}_{0,2}$ mode, the intermodal combination of $3\times\mathrm{LP}_{0,1}$ and $1\times\mathrm{LP}_{0,2}$, the intermodal combination of $2\times\mathrm{LP}_{0,1}$ and $2\times\mathrm{LP}_{0,2}$, and the intermodal combination of $1\times\mathrm{LP}_{0,1}$ and $3\times\mathrm{LP}_{0,2}$.

the $LP_{0,1}$ mode and the $LP_{0,2}$ mode has a strong wavelength dependence. This stems from the avoided-crossing between the $LP_{0,1}$ mode and the $LP_{0,2}$ mode. By comparing the effective area of the intermodal combination of $3 \times LP_{01}$ and $1 \times LP_{02}$ in Fig. 7.3 with the effective area for the FWM process shown in Fig. 7.2, it can be realised that it is not valid in this case to approximate the dispersion of the effective area with the fourth-root method. The minimum value of the effective area of the intermodal combination of $3 \times LP_{01}$ and $1 \times LP_{02}$ is approximately 18 μm^2 at a wavelength of 1097 nm. This is compared to the 7 μm^2 at the idler wavelength of 945 nm or the signal wavelength of 1216 nm. Therefore, an implementation with the intermodal effective areas shown in Fig. 7.3 will not capture the features of the FWM process as the non-linear coupling is under estimated. To capture the FWM process in the simulation, the field-overlap calculation needs to be correctly incorporated in the numerical calculation and the framework of the Transverse-Field Dispersion in the Generalised Non-Linear Schrödinger Equation (TFD-GNLSE) from Sec. 2.2.3 should be applied.

As the LSF has a radial symmetric refractive index profile, it is possible to write the transverse-field distributions on a one-dimensional grid with sine or cosine modulation to account for the angular dependence. To reduce the number of radial grid points used, a Gaussian quadrature rule is applied to compute the transverse-field overlap. In Fig. 7.4 the effective areas for the $LP_{0,1}$ mode and the $LP_{0,2}$ mode are calculated with the use of Gauss-Legendre quadrature and 18 radial grid points spanning from 0 μm to 12 μm. It is observed that with 18 grid points it

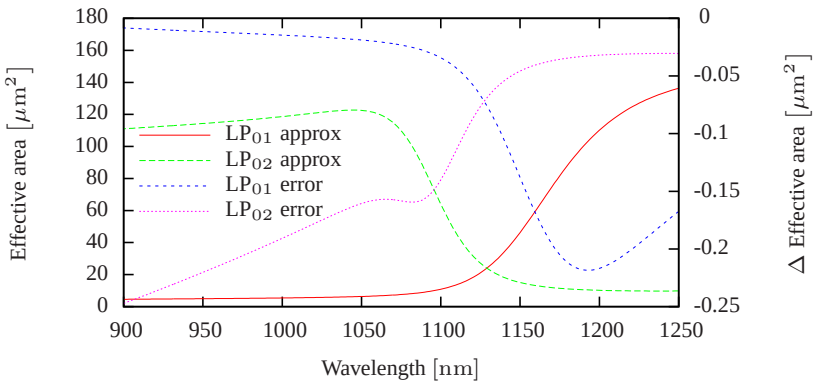

Figure 7.4: The effective area calculated with the Gauss-Legendre quadrature method and 18 radial grid points. The error is with respect to the calculation without using the Gauss-Legendre quadrature method.

is possible to describe the dispersion of the normalised transverse-field-distributions without any significant error. The number of radial grid points is a trade-off between computational accuracy and computation time.

The equations for modelling the FWM process between the $LP_{0,1}$ mode and the $LP_{0,2}$ mode, with the framework of the GNLSE and the framework of the TFD-GNLSE are presented in Sec. 2.2.2 and in Sec. 2.2.3, respectively. To simulate the experimental FWM spectrum in Fig. 7.1a, the numerical simulation is started with a pump pulse in the $LP_{0,1}$ mode at a centre wavelength of 1064 nm and vacuum noise in all the other frequency bins for both modes. The number of points used on the time/frequency grid is 2^{14}, the time discretisation is 8 fs, the centre wavelength of the simulation window is 1064 nm, the shape of the input pulse intensity is a sech^2, the temporal full-width at half-maximum (FWHM) of the pulse intensity is 6 ps, the input peak power of the pulse is 3085.25 W, the intensity-dependent refractive index of the fibre is 2.6×10^{-20} $\frac{\text{m}^2}{\text{W}}$, the f_R ratio is 0.18, the length of the fibre is 1.75 m, and the loss is neglected. The reference for the moving time frame is the $LP_{0,1}$ mode. The simulation is performed using the Fourth-Order Runge-Kutta in the Interaction-Picture (RK4IP) method [42] and the efficient adaptive step size method [91], with a local error limit of 10^{-7} for the conserved quantity, which is proportionally to the photon number. The radial grid is made by using 18 grid points spanning from 0 μm to 12 μm for the TFD-GNLSE implementation. In Fig. 7.1b the simulated output spectrum for the FWM experiment in the LSF is shown both for the standard GNLSE with the fourth-root method and the TFD-GNLSE implementation with the correct dispersion of the transverse field distribution. It is observed that there is no FWM when using the standard GNLSE, however, by comparing Fig. 7.1a and Fig. 7.1b it is observed that the TFD-GNLSE numerical implementation is able to reproduce the features of the FWM experiment. There are minor discrepancies, which could be caused by the fact that the true shape, power and chirp of the input pulse are not known. Also there could be effects from the strength of the non-linear coupling terms as the intensity-dependent refractive index is assigned a constant value, while in principle this should be dependent on the material composition and the field distribution for the specific third order non-linear interaction.

As the TFD-GNLSE is able to reproduce the features of the intermodal FWM experiment, the TFD-GNLSE can be used to gain a

deeper insight in the intermodal FWM process. The temporal evolution for the two modes is shown in Fig. 7.5 as a contour plot of time and longitudinal position in the fibre. The spectral evolution for the two

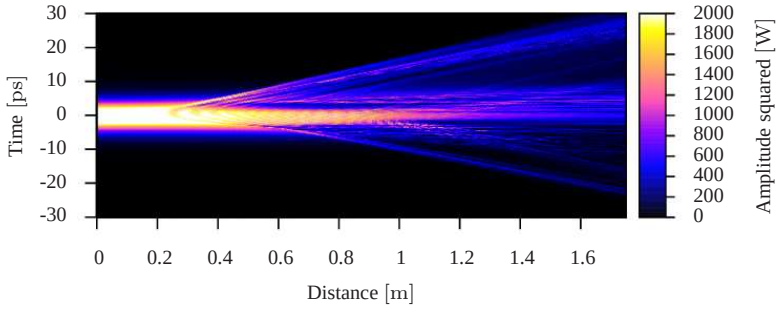

(a) The temporal evolution for the $LP_{0,1}$ mode as a contour plot of time and longitudinal position in the fibre. The idler has gained a significant amount of power just after 0.2 m of propagation and is split off the pump pulse.

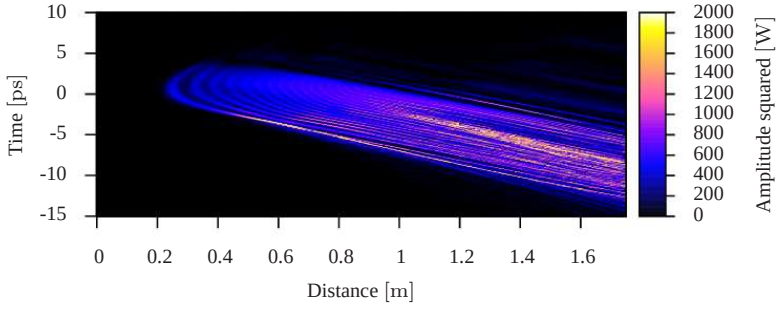

(b) The temporal evolution for the $LP_{0,2}$ mode as a contour plot of time and longitudinal position in the fibre. The signal has gained a significant amount of power just after 0.2 m of propagation.

Figure 7.5: The temporal evolution as a contour plot of time and longitudinal position in the LSF for the FWM process between the $LP_{0,1}$ mode and the $LP_{0,2}$ mode.

modes is shown in Fig. 7.6 as a contour plot of wavelength and longitudinal position in the fibre. From Fig. 7.5 it is observed how the signal pulse and the idler pulse have gained a significant amount of power after they have propagated just 0.2 m. The process is dominated by the non-linear interaction, the length of which is 1.5 cm for the pump,

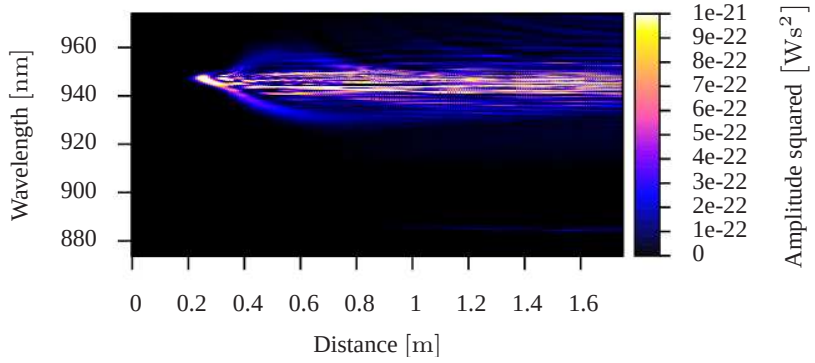

(a) The idler in the FWM process, which is in the $LP_{0,1}$ mode.

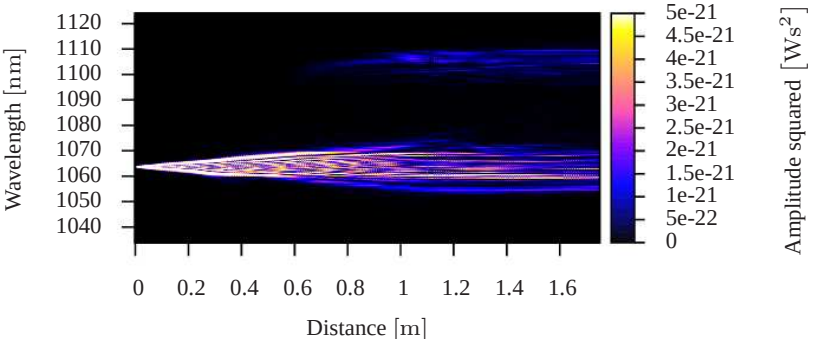

(b) The pump in the FWM process, which is in the $LP_{0,1}$ mode.

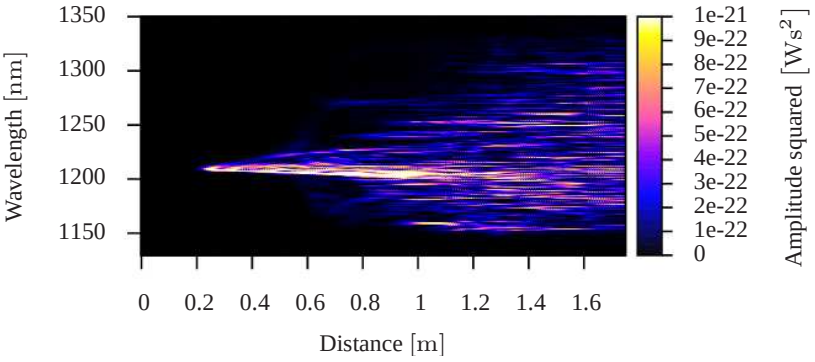

(c) The signal in the FWM process, which is in the $LP_{0,2}$ mode.

Figure 7.6: The spectral evolution as a contour plot of wavelength and longitudinal position in the LSF for the FWM process with a pump and a idler in the $LP_{0,1}$ mode and with a signal in the $LP_{0,2}$ mode.

however, the difference in group delay between the pump, the signal, and idler leads to walk-off and temporal pulse broadening. The walk-off length between the pump and the signal is approximately 82 cm and between the pump and the idler it is approximately 34 cm. In Fig. 7.6 it is observed how the pump pulse undergoes spectral broadening due to self-phase-modulation, which results in a spectral broadening of both the signal and idler as this allows for phase-matching with a pump detuned slightly from 1064 nm. In Fig. 7.7 the simulated output spectra for both the $LP_{0,1}$ mode and the $LP_{0,2}$ mode in the FWM experiment are shown for the TFD-GNLSE implementation. It is observed that

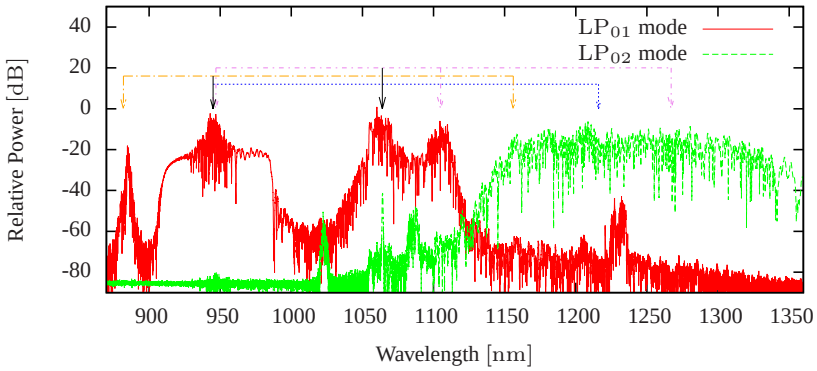

Figure 7.7: Simulated output spectrum for the FWM experiment with the TFD-GNLSE. The three FWM processes listed in Table 7.1 is highlighted. Process 1 is the blue dotted line, Process 2 is the orange long-dash-dotted line, Process 3 is the purple short-dash-dotted line, and the solid arrow indicates a wavelength used in more than one FWM process.

the spectra for the $LP_{0,1}$ mode and the $LP_{0,2}$ mode contain multiple peaks as a result of multiple FWM processes. The three most significant FWM processes listed in the order that FWM processes occur in Table 7.1.

	Idler/$LP_{0,1}$	Pump 1/$LP_{0,1}$	Pump 2/$LP_{0,1}$	Signal/$LP_{0,2}$
Process 1	945 nm	1064 nm	1064 nm	1216 nm
Process 2	882 nm	945 nm	1064 nm	1156 nm
Process 3	947 nm	1064 nm	1105 nm	1267 nm

Table 7.1: The three most significant FWM processes listed in the order that FWM processes occur. The light at 1105 nm in the $LP_{0,1}$ mode and the light at 1267 nm in the $LP_{0,2}$ mode are seeded by Raman amplification from light at 1064 nm in the $LP_{0,1}$ mode and light at 1216 nm in the $LP_{0,2}$ mode, respectively.

7.1.1 Variation of the Dispersion of the Transverse-Field Distribution

In order to probe further into the failure of the GNLSE, when predicting the intermodal FWM in the LSF, the output spectra of the GNLSE and the TFD-GNLSE are compared for different simulations as the dispersion of the transverse field distributions is varied. It is only the dispersive properties of the transverse field distributions and not the dispersion properties for the effective indices that is varied, as this will ensure the same linear phase matching condition for the FWM processes in all the simulation. This investigation is performed to determine to what limit it is possible to use the GNLSE for fibres that exhibit a smaller amount of dispersion than the LSF, i.e. a standard multi-mode fibre (MMF). The initial conditions for the FWM experiment remain the same. The transverse field is synthesised as a combination of the real field and a field of the reference mode, which does not exhibits the same magnitude of dispersion as the real fields. The reference mode is the fundamental mode of the isolated core wave-guide in Fig. 4.3b. The effective areas of the $\mathrm{LP}_{0,1}$ mode and the $\mathrm{LP}_{0,2}$ mode are shown together with the reference mode in Fig. 7.8. The synthesised transverse fields

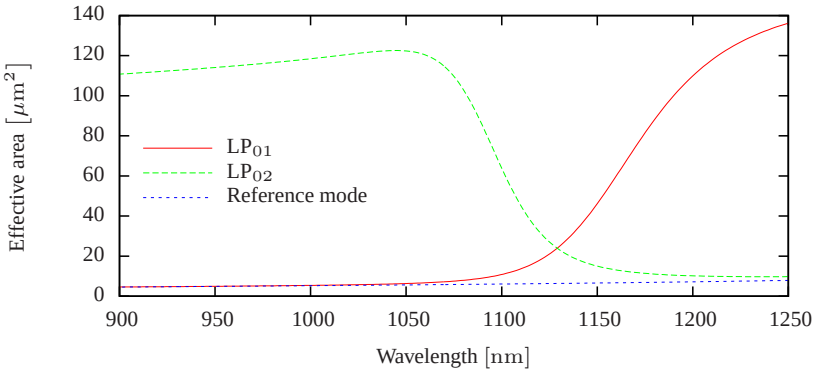

Figure 7.8: The effective areas of the $\mathrm{LP}_{0,1}$ mode and $\mathrm{LP}_{0,2}$ mode in LSF is shown together with the effective area for the reference mode.

are given as

$$\tilde{F}_{01}^{\mathrm{synth}} = \tilde{F}_{0,1} X + (1 - X)\, \tilde{F}_{\mathrm{ref}}, \tag{7.1.4}$$

$$\tilde{F}_{02}^{\mathrm{synth}} = \tilde{F}_{0,2} X + (1 - X)\, \tilde{F}_{\mathrm{ref}}, \tag{7.1.5}$$

where X is the mixing coefficient, $\tilde{F}_{i,j}$ is the real field, and $\tilde{F}_{\text{ref}}$ is the field of the reference mode. The intermodal combination of the synthesised fields for the combination of $3\times\text{LP}_{0,1}$ and $1\times\text{LP}_{0,2}$ is shown in Fig. 7.9 for varying mixing coefficient. The intermodal combination of $3\times\text{LP}_{0,1}$ and $1\times\text{LP}_{0,2}$ is the dominating intermodal combination of the FWM processes as shown in Table 7.1. As the real fields contribute

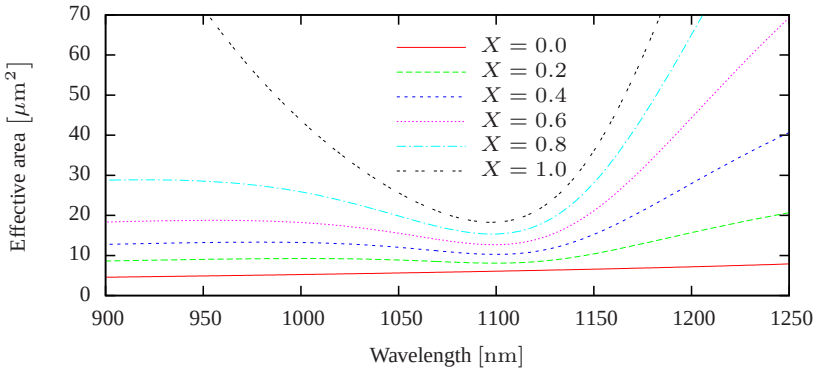

Figure 7.9: The intermodal effective areas for the combination of three $\text{LP}_{0,1}$ mode and one $\text{LP}_{0,2}$ mode for different values of the mixing parameter, X. The behaviour shown is similar to that of the other intermodal effective areas.

an increasing part of the synthesised fields, i.e. as the mixing coefficient X approaches 1, the intermodal effective area increases, which indicates a decrease in the strength of the non-linear interaction.

In Fig. 7.10 the output spectrum of the $\text{LP}_{0,1}$ mode is shown as a function of the mixing coefficient. In Fig. 7.11 the output spectrum of the $\text{LP}_{0,2}$ mode is shown as a function of the mixing coefficient. It is observed that the general features are lost for a mixing coefficient of 0.4 and higher in the GNLSE simulations. At a mixing coefficient of 0.6 and higher the GNLSE is unable to reproduce any FWM, keeping in mind that the linear part of the FWM phase matching criterion is the same for all the simulations. The reduction in the efficiency of the FWM process is therefore directly linked to the transverse overlap integral of the given FWM process, i.e. the inverse of the effective area.

7.2 Čerenkov Radiation

The work in this section is based upon [97, 98]. During experiments with propagation of soliton pulses in the LSF in the $\text{LP}_{0,2}$ mode it was

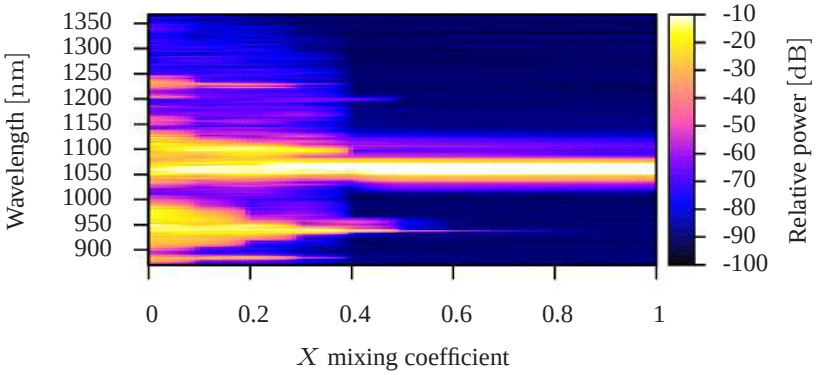

(a) Calculated $LP_{0,1}$ output spectrum with the GNLSE.

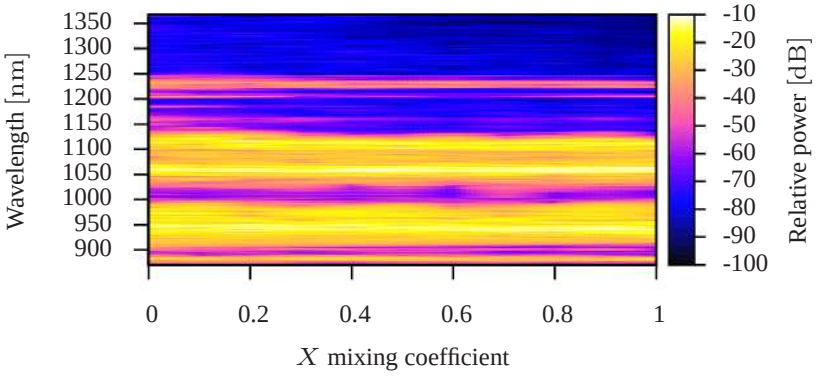

(b) Calculated $LP_{0,1}$ output spectrum with the TFD-GNLSE.

Figure 7.10: Comparison between the output spectra for the $LP_{0,1}$ mode with the GNLSE and TFD-GNLSE.

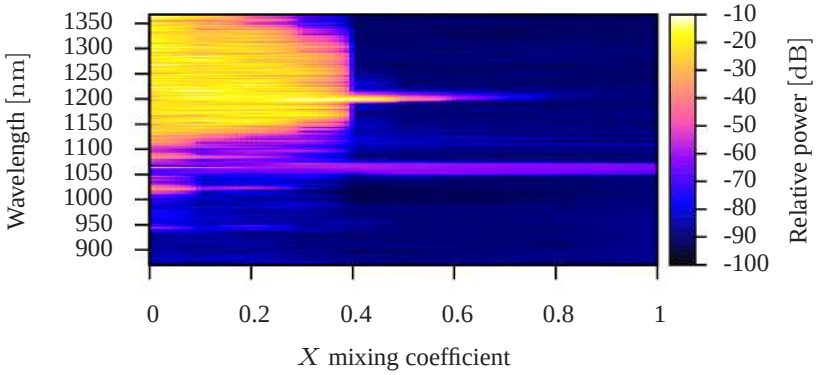

(a) Calculated $LP_{0,2}$ output spectrum with the GNLSE.

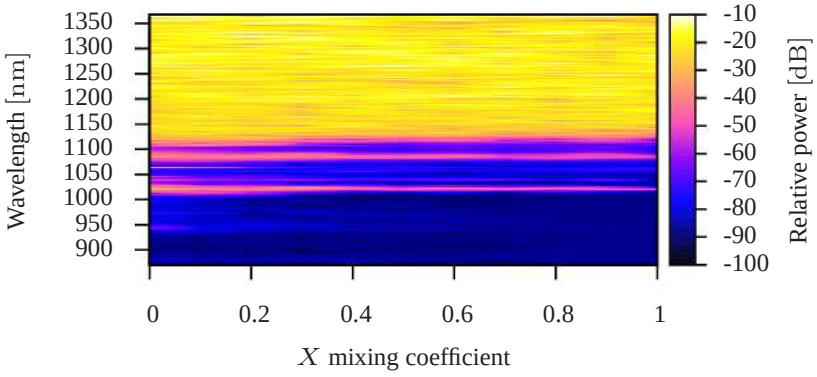

(b) Calculated $LP_{0,2}$ output spectrum with the TFD-GNLSE.

Figure 7.11: Comparison between the output spectra for the $LP_{0,2}$ mode with the GNLSE and TFD-GNLSE.

realised that it was possible to couple light to the longer wavelengths from the soliton in the LSF, as shown by the results in Sec. 6.2.2. The coupling is provided by an intermodal Čerenkov process between the soliton in the $LP_{0,2}$ mode and the dispersive wave in the $LP_{1,1}$ mode. The intermodal Čerenkov process requires the LSF to be perturbed from the ideal perfectly cylindrical symmetric case, e.g. by a bend of the fibre. In the ideal case the $LP_{0,2}$ mode has anomalous dispersion, whereas the $LP_{1,1}$ mode has normal dispersion in the vicinity of the wavelength of the mode-crossing between the two modes. When the LSF is bent the mode classification is altered and the intermodal Čerenkov process observed in the experiment is in fact an intramodal Čerenkov process in the framework of the bend fibre. This is explained in details in the following.

It is possible to calculate the wavelength of the Čerenkov radiation from a solution in the case where the interaction takes place in the same mode [9]. This approach is extended to cover a multi-mode (MM) case. In general the phase of a propagating wave in the z-direction is written as

$$\phi = \beta(\omega)\, z - \omega t + \phi_0, \tag{7.2.1}$$

where β is the propagation constant, ω is the angular frequency, z is the distance, t is the elapsed time, and ϕ_0 is an arbitrary phase constant. The soliton propagates as a wave-package with the speed of the group-velocity of the centre frequency of the soliton. Therefore, the elapsed time is written as

$$t = \frac{z}{v_{\mathrm{g,s}}}, \quad \text{where} \quad v_{\mathrm{g,s}} = \left(\left. \frac{\partial \beta_{0,2}}{\partial \omega} \right|_{\omega_\mathrm{s}} \right)^{-1}. \tag{7.2.2}$$

$v_{\mathrm{g,s}}$ is the group-velocity of the soliton in the $LP_{0,2}$ mode. The phase of the soliton in the $LP_{0,2}$ mode and the dispersive wave in the $LP_{1,1}$ mode is given by

$$\phi_{0,2} = \beta_{0,2}(\omega_\mathrm{s})\, z - \omega_\mathrm{s} \left. \frac{\partial \beta_{0,2}}{\partial \omega} \right|_{\omega_\mathrm{s}} z + \phi_0, \tag{7.2.3}$$

$$\phi_{1,1} = \beta_{1,1}(\omega_\mathrm{d})\, z - \omega_\mathrm{d} \left. \frac{\partial \beta_{0,2}}{\partial \omega} \right|_{\omega_\mathrm{s}} z + \phi_0. \tag{7.2.4}$$

The non-linear contribution to the phase is excluded as this only contributes to a minor correction. The Čerenkov radiation-process occurs

when the soliton and the dispersive wave are phase matched leading to the following expression,

$$\beta_{1,1}\left(\omega_{\mathrm{d}}\right) = \beta_{0,2}\left(\omega_{\mathrm{s}}\right) + \left(\omega_{\mathrm{d}} - \omega_{\mathrm{s}}\right) \left.\frac{\partial \beta_{0,2}}{\partial \omega}\right|_{\omega_{\mathrm{s}}}. \tag{7.2.5}$$

It is possible to solve Eq. 7.2.5 with a graphical method. The angular frequency of the dispersive wave can be found by calculating the tangent to the propagation constant of the soliton and observing where the tangent intersects the propagation constant of the dispersive wave. In Fig. 7.12 this is illustrated for the LSF, where the soliton is centred at a wavelength of 1085 nm and the dispersive wave generated by Čerenkov process is located at a wavelength of 1153 nm. In Fig. 7.12 the material

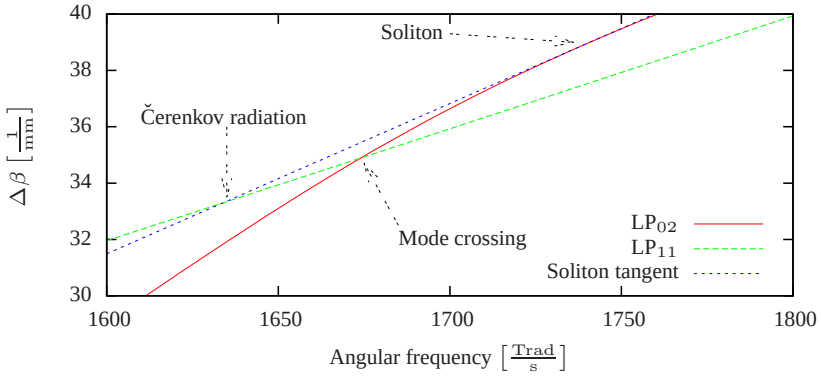

Figure 7.12: Illustration of the graphical solution to find the phase matching between the dispersive wave and the soliton. The $\Delta\beta$ shown on the y-axis is the propagation constant, where the silica material contribution is subtracted in order to give a more clear representation.

contribution of pure silica is subtracted from the propagation constants, Eq. 7.2.5 is still valid as long as

$$\left.\frac{\partial \beta_{\mathrm{silica}}}{\partial \omega}\right|_{\omega_{\mathrm{s}}} \left(\omega_{\mathrm{d}} - \omega_{\mathrm{s}}\right) + \beta_{\mathrm{silica}}\left(\omega_{\mathrm{s}}\right) - \beta_{\mathrm{silica}}\left(\omega_{\mathrm{d}}\right) \approx 0. \tag{7.2.6}$$

This is fulfilled as long as the slope of the material-propagation constant is constant within the considered bandwidth, which is approximately true for this case.

From the graphical solution shown in Fig. 7.12 it is realised that it should be possible to phase match a Čerenkov radiation-process every time there is a mode-crossing, with no consideration of the dispersive

properties of the two modes. However, a mode-crossing indicates that the two modes have the same effective index at the same wavelength, hence the two modes must have a different angular eigenvalue for the modes to fulfil the orthogonality requirement. The coupling to the dispersive wave can be described by the following differential equation

$$\begin{aligned}\frac{\partial}{\partial z}\tilde{A}_{1,1} = &-\frac{\alpha_{1,1}}{2}\tilde{A}_{1,1} + i\left(\beta_{1,1} - \beta^{\mathrm{ref}}(\omega_0) - \beta_1^{\mathrm{ref}}(\omega_0)(\omega-\omega_0)\right)\tilde{A}_{1,1} \\ &+ \tilde{Q}_{1,1:1,1:1,1:1,1} + \tilde{Q}_{1,1:0,2:1,1:1,1} + \tilde{Q}_{1,1:1,1:0,2:1,1} + \tilde{Q}_{1,1:1,1:1,1:0,2} \\ &+ \tilde{Q}_{1,1:0,2:0,2:1,1} + \tilde{Q}_{1,1:0,2:1,1:0,2} + \tilde{Q}_{1,1:1,1:0,2:0,2} + \tilde{Q}_{1,1:0,2:0,2:0,2}.\end{aligned} \tag{7.2.7}$$

The value of $\tilde{Q}_{1,1:0,2:1,1:1,1}$, $\tilde{Q}_{1,1:1,1:0,2:1,1}$, $\tilde{Q}_{1,1:1,1:1,1:0,2}$, and $\tilde{Q}_{1,1:0,2:0,2:0,2}$ should all equal zero in a perfect cylindrical symmetric fibre as the transverse field overlap is zero due to the angular symmetry of the transverse field of the modes. Therefore, the strength of the intermodal Čerenkov radiation is zero for the perfect cylindrical symmetric fibre. However, any perturbation of the fibre, i.e. a bend, will lead to an asymmetric transverse field of the $\mathrm{LP}_{0,2}$ mode and hereby enable the Čerenkov process. To a first-order approximation the sharper the bend is the better the field overlap and the stronger the non-linearity is.

To experimentally verify the control of the strength of the intermodal Čerenkov radiation-process by bending the LSF a soliton was initiated in the $\mathrm{LP}_{0,2}$ mode and three different bend radii were applied to the fibre. The setup for pumping the LSF was described in Sec. 6.1.2. The length of the LSF is 90 cm and the bend is applied to the fibre in such a manner that there is approximately 20 cm of straight fibre at the output end. In Fig. 7.13 the recorded output spectra are shown for different pulse energies and for different bend radii. When the LSF is kept straight and for the applied pulse energies the soliton tunes from a wavelength of 1085 nm to a wavelength of 1120 nm as shown in Fig. 7.13a. The modulation of the spectrum at an input pulse energy of 18 nJ is assumed to be caused by mode coupling, which is induced by fabrication imperfections of the fibre. It is observed that there is no noticeable Čerenkov generated wave in the spectra. This observation is consistent with the theoretical prediction that the field-overlap integral vanishes for the intermodal Čerenkov process in this case. However, by bending the fibre the field-overlap integral no longer vanishes and thereby enables coupling between the soliton in the $\mathrm{LP}_{0,2}$ mode and the dispersive wave in the $\mathrm{LP}_{1,1}$ mode. This is experimentally observed in

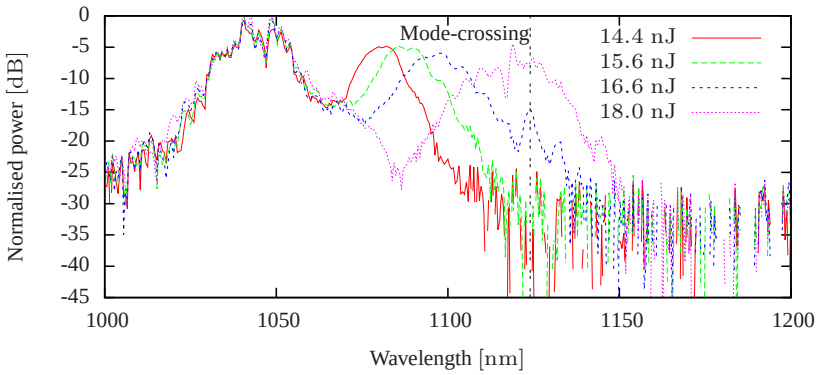

(a) The fibre is kept straight.

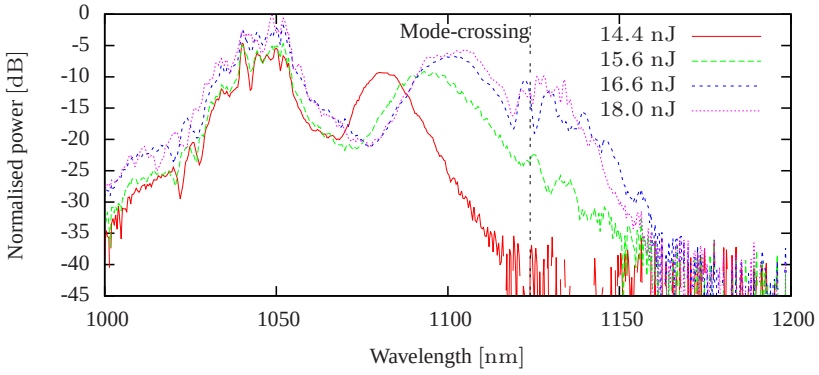

(b) The fibre is bent around an object with a radius of 14.0 cm.

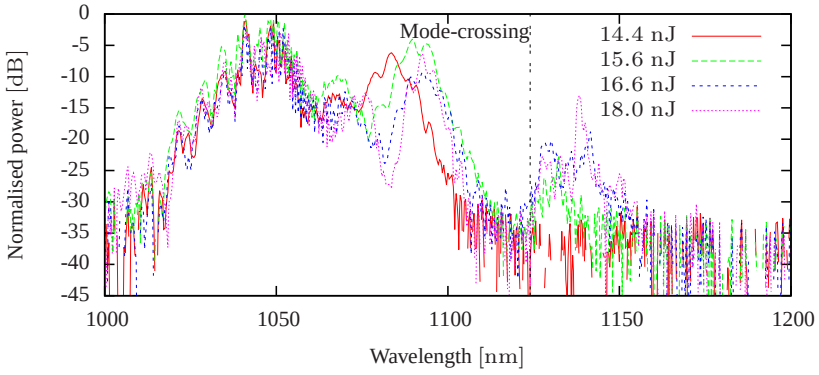

(c) The fibre is bent around an object with a radius of 5.5 cm.

Figure 7.13: The measured output spectra for three different bend radii, which are applied to the LSF for different input pulse energies.

Fig. 7.13b and in Fig. 7.13c at the longer wavelength side of the spectra. The mode image of the soliton and the dispersive wave was measured for a bend radius of 14 cm. The measured mode image is shown in Fig. 7.14. The dispersive wave is imaged with a long-pass filter with a

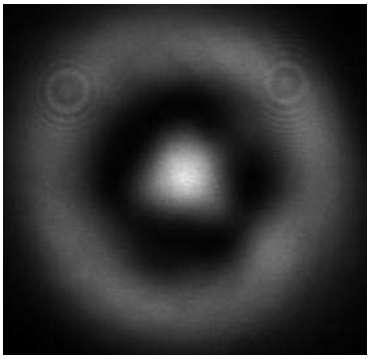

(a) The measured mode image of the soliton.

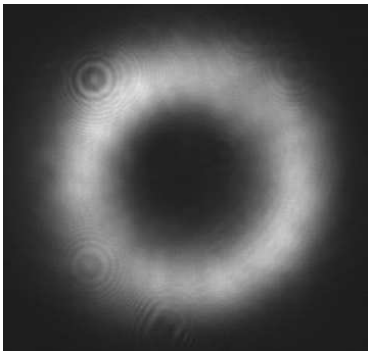

(b) The measured mode image of the dispersive wave.

Figure 7.14: The measured mode image of the soliton and the dispersive wave generated by the intermodal Čerenkov process.

band edge of at 1150 nm. The power is the reduce to a point where the recorded mode image after the long-pass filter with a band edge of at 1150 nm has vanished. This ensures that there is no detectable dispersive wave. Then the soliton is imaged with a long-pass filter with a band edge of at 1064 nm. From the imaged modes it is clear that the soliton is in the $LP_{0,2}$ mode. The mode image of the dispersive wave could be turned into two side-lobes with a zero intensity line in the middle by inserting a polariser before the camera. The zero intensity line could be rotated by adjusting the polariser, which indicates that the dispersive wave is in the $LP_{1,1}$ mode.

In the following a modesolver written by *John Fini* from *OFS Laboratories*, which handles calculations on bend index profiles, is used to understand the intermodal Čerenkov process in the framework of the bend fibre. To reduce the computational problem the modesolver only solves the bend fibre in one half of the domain and assumes a symmetrical boundary condition on the boarder to the other half of the domain. The modesolver is used to calculate the mode properties for the LSF with an applied bend. In Fig. 7.15 the effective indices for the different modes are shown as a function of wavelength. The bend radius in the calculation is 5.5 cm. The mode labelling for the five modes shown in

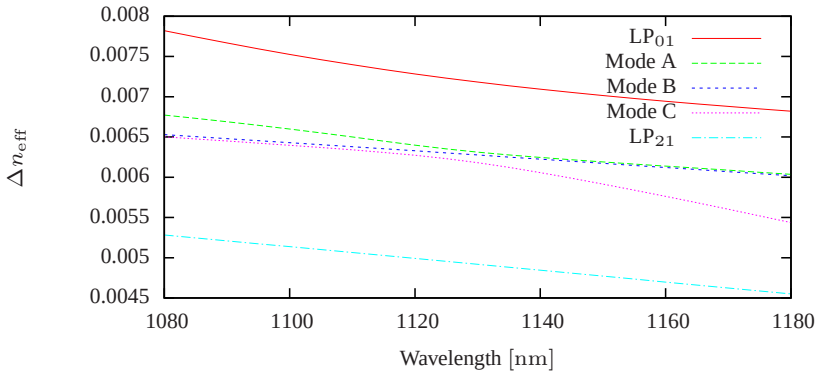

Figure 7.15: The calculated effective indices for the LSF with an applied bend radius of 5.5 cm, where the material contribution from pure silica is subtracted.

Fig. 7.15 is different compared to the convention that has been used so far in the thesis. Two of the modes are identified as the standard LP modes, i.e. the $LP_{0,1}$ mode and the $LP_{2,1}$ mode. The three other modes are assigned the mode labelling A, B, and C as the properties of transverse intensity flow in the longitudinal direction changes with wavelength for these modes. The flow of intensity in the longitudinal direction for the modes A, B, and C is shown in Fig. 7.16. At the shorter wavelength the mode profile of mode A resembles a bend $LP_{0,2}$ mode and as the wavelength increases the mode profile of mode A changes. At the longer wavelengths the mode profile of mode A resembles a bend doughnut mode, which is part of the $LP_{1,1}$ mode group. The opposite is true for the mode C. At the shorter wavelength the mode profile of mode C resembles a bend $LP_{1,1}$ mode and at the longer wavelengths the mode profile of mode C resembles a bend $LP_{0,2}$ mode, which is guided in the core wave-guide and therefore most of all resembles a $LP_{0,1}$ mode. From this it can be realised that when the fibre is bent the mode A and the mode C must make an avoided-crossing to satisfy the orthogonality requirement. The avoided-crossing between the mode A and the mode C in the bend fibre enables the Čerenkov process. The dispersion of mode A on the shorter wavelength side of the avoided-crossing is anomalous, as the $LP_{0,2}$ mode in the straight fibre. The avoided-crossing effects and changes the curvature of the mode A, as the curvature is directly related to the group-velocity dispersion, see Eq. 4.1.2, the dispersion of mode A changes to normal, as the $LP_{1,1}$ mode in the straight fibre, on the longer wavelength side of the avoided-crossing. Therefore in the

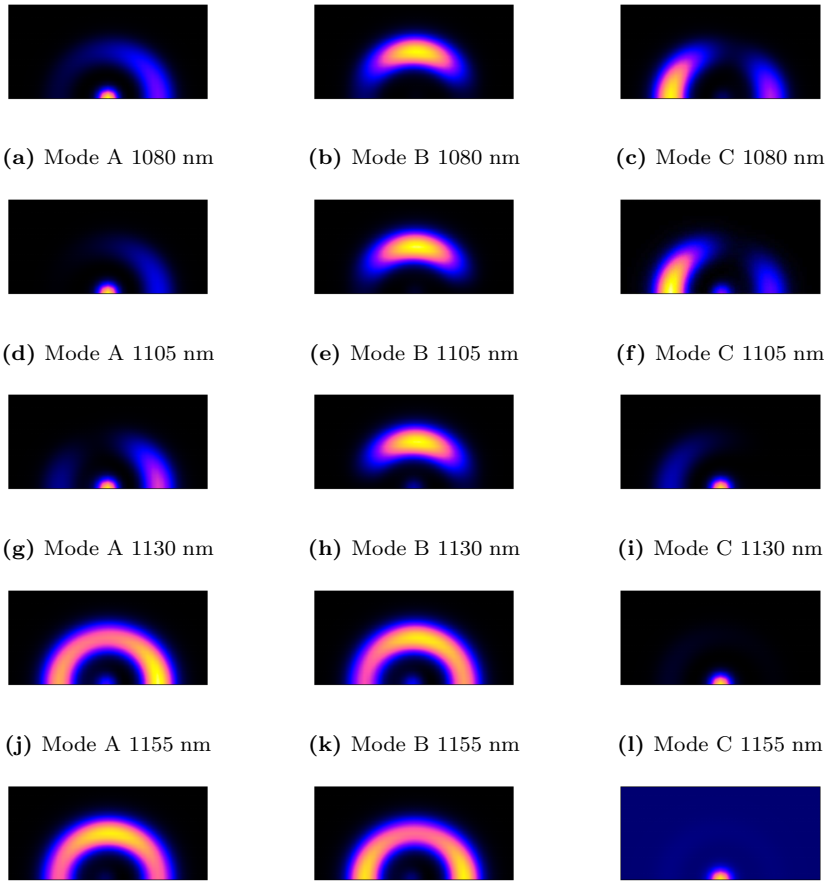

(a) Mode A 1080 nm **(b)** Mode B 1080 nm **(c)** Mode C 1080 nm

(d) Mode A 1105 nm **(e)** Mode B 1105 nm **(f)** Mode C 1105 nm

(g) Mode A 1130 nm **(h)** Mode B 1130 nm **(i)** Mode C 1130 nm

(j) Mode A 1155 nm **(k)** Mode B 1155 nm **(l)** Mode C 1155 nm

(m) Mode A 1180 nm **(n)** Mode B 1180 nm **(o)** Mode C 1180 nm

Figure 7.16: The flow of intensity in the longitudinal direction for the modes A, B, and C in Fig. 7.15 at different wavelengths. The dimensions of the intensity plots are from -10 μm to 10 μm in the x-direction and from 0 μm to 10 μm in the y-direction. The bright colours represent areas of high intensity, whereas the darker represent areas of low intensity on a linear scale.

bend fibre the Čerenkov process is an intramodal process in the mode A, however, when the fibre is straighten the soliton is in the $LP_{0,2}$ mode and the dispersive wave is in the $LP_{1,1}$ mode. Even though that the non-linear coupling is in fact an intramodal process in the bend fibre, it is an effectively intermodal process in the straight fibre. From the effective area of the modes shown in Fig. 7.17, which is valid for a bend radius of 5.5 cm, it is verified that the mode A and the mode C exhibit an avoid-crossing. From the effective area it is confirmed that the mode

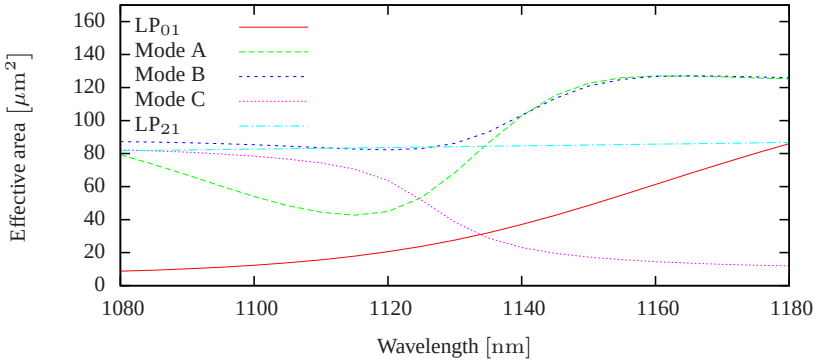

Figure 7.17: The calculated effective area for the LSF with an applied bend radius of 5.5 cm.

A is located in the ring structure of the triple-clad wave-guide at the shorter wavelength and as the mode is trying to transcend to the core structure, the mode is forced back into the ring structure. The effective indices and the effective areas are also calculated for a bend radius of 16 cm and 30 cm, which is found in App. A.6.1. From a comparison of the effective indices for the different bend radii it is realised that the sharper the bend is, the shorter is the wavelength where the effect from avoided-crossing begins. This explains why the soliton self-frequency shift (SSFS) is reduced for smaller bend radii as observed in Fig. 7.13, as the anomalous dispersion region of the mode A is changed to a normal dispersion region with the effect from the avoided-crossing.

Chapter 8

Conclusion

In this chapter the results and conclusion of the thesis are presented.

Two speciality few-moded fibres (FMFs), i.e. the left-sided fibre (LSF) and the right-sided fibre (RSF), were designed and optimised for used in a cascade configuration, where the two fibres can support a shift of a soliton pulse from the ytterbium gain-band to longer wavelengths. The mode of operation in the two speciality FMFs is the $LP_{0,2}$ mode. The two speciality FMFs was characterised and the characterisation was in agreement with the prediction from the design. The two speciality FMFs are designed for an unchirped input pulse centred at a wavelength of 1064 nm with a $sech^2$ intensity profile, a temporal full-width at half-maximum (FWHM) of 400 fs, and a pulse energy of 11.1 nJ. The resulting output pulse after 19 cm of LSF and 8.5 cm of RSF centred at a wavelength of 1277 nm has a pulse energy of 5.1 nJ and a temporal FWHM of 15 fs. The transfer wavelength between the LSF and the RSF was 1100 nm.

It was demonstrated that it was possible to splice two different FMFs together with a splice loss of 1.6 dB using a combination of a fusion-splice process and a gas-line-burner process.

In the practical experiments the length of LSF had a significant impact on the soliton self-frequency shift (SSFS). In the experiments with an unchirped femtosecond input pulse the soliton pulse could be shifted to the transfer wavelength of 1100 nm and beyond, if the few centimetres of LSF was kept straight. In the experiments with a chirped picosecond input pulse the SSFS was halted at a centre wavelength of 1075 nm, where the soliton pulse had a pulse energy of 2.6 nJ and a temporal FWHM of 144 fs. The SSFS was halted by a novel intermodal

Čerenkov process, when the fibre was bent. For the chirped picosecond input the length of LSF was on a tens of metre scale, which required the fibre to be on a spool or in a coil.

A novel non-linear intermodal Čerenkov process was experimentally observed in the LSF, when the fibre was bent. The intermodal Čerenkov process coupled light from a soliton in the $LP_{0,2}$ to a dispersive wave in the $LP_{1,1}$ mode located at longer wavelengths. The theory for the intermodal Čerenkov process was presented and it was described how the coupling in the bend fibre is in fact an intramodal Čerenkov process, but as the fibre is straighten the process appears to be an intermodal Čerenkov process.

The Generalised Non-Linear Schrödinger Equation (GNLSE) was derived and expanded to include multi-mode (MM) non-linear interactions. An alternative variant of the GNLSE, i.e. the Transverse-Field Dispersion in the Generalised Non-Linear Schrödinger Equation (TFD-GNLSE), which included the correct dispersion of the transverse-field distribution was also derived. The TFD-GNLSE was able to reproduce the intermodal four-wave mixing (FWM) experiment in the LSF, while the GNLSE failed to do so. The GNLSE failed to reproduce the intermodal FWM experiment as the modes involved in the FWM process in the LSF exhibits a significance amount of dispersion. For FMFs where the effective area remains approximately constant over the considered bandwidth it would be acceptable to use the GNLSE, as shown with the investigation where the dispersion of the transverse-field distribution was varied.

The intensity-dependent refractive index and the Raman effect was measured for five step-index fibres, which had a germanium-doped core and a cladding of pure silica. A linear relationship between the intensity-dependent refractive index and a weighted germanium concentration was established. A linear relationship between the Raman contribution to the intensity-dependent refractive index and the weighted germanium concentration was also established. From these two linear relationships the Raman fraction of the intensity-dependent refractive index was obtained. For the considered step-index fibres the Raman fraction decreases from 0.16 to 0.15 for an increase in the weighted germanium concentration.

An all-normal dispersive (ANDi) polarisation-maintaining (PM) laser was used as an case example to gain a more theoretical understanding of the mode-locking dynamics in a mode-locked oscillator. Specifically, it

was shown that the bandwidth of the ytterbium gain-band is sufficient to provide the filtering effect in the ANDi laser, when the accumulated non-linear phase-shift per round-trip of the mode-locked pulses is small.

Chapter 9

Outlook

In this chapter the thoughts and recommendations for continuation of the project are presented.

In general and stimulated by the interest in FMFs, a more thorough and fundamental investigation of the intermodal non-linearities is of interest to justify the current model and non-linear strengths. For the investigation of the intensity-dependent refractive index and the Raman contribution to the intensity-dependent refractive index, it would be interesting to establish the dependence of other dopant materials. Here fluorine is the material of most interest. In this case the step-index fibres should have a core of pure silica and a cladding or trench of fluorine-doped silica.

The TFD-GNLSE successfully incorporated the dispersion of the transverse-field distribution and the TFD-GNLSE was able to reproduce the intermodal FWM experiment in the LSF. The complexity of the TFD-GNLSE code is significantly greater than the GNLSE code. There where an assumption in the derivation of the TFD-GNLSE that with no cost in increased complexity could be included in the TFD-GNLSE code. The assumption is made when the unit of the longitudinal complex amplitude is converted to $\sqrt{\mathrm{W}}$. The refractive index should have remained inside the integral over the transverse area together with the transverse-field distribution when going from Eq. A.1.26 to Eq. A.1.27. For future use it is recommended to use Eq. A.1.26 in order to increase the accuracy of the numerical model.

The setup with the chirped picosecond source coupled into the LSF and the RSF did unfortunately not yield the desired widely tunable short-pulse laser. The reason for this is speculated to be contributed

one or more of the following issues: The ratio of amplified spontaneous emission (ASE) in the amplified spectrum, the chirp of the pulse, or the splice process between the different FMFs.

The amount of ASE noise from the amplifier chain after the master oscillator is potentially significant compared to the amplified pulses. The chain of amplifier should be upgraded to include isolators between the amplifier stages and to protect the pump lasers. If this is not sufficient to eliminate the parasitic ASE, then the signal should be time filtered with an acousto-optical modulator or an electro-optic modulator. With the use of additional isolators it is possible to use the two last amplifiers in a backward and forward configuration, hereby increasing the efficiency of the amplification process and reduce the accumulated chirp and self-phase modulation (SPM).

The critical issue with the chirped picosecond source is that the pulse must first be de-chirped in the LSF. This requires a significant length of fibre, which means the fibre needs to be coiled or on a spool. The bending radius of the fibre on the spool or in a coil facilitates the intermodal Čerenkov radiation, which cancels the SSFS process. A systematic variation of the critical coil radius for the entire length of LSF on the spool or in the coil would be in order to determine the radius, where the intermodal Čerenkov process is negligible for the compression process and the subsequently SSFS. A possible solution to this problem is to have a pulse on a femtosecond duration as the input to the LSF or to de-chirp the chirped picosecond pulse. Potential compression methods are hollow bandgap fibres [99, 100], bulk gratings [83], and chirped fibre Bragg gratings [101, 102]. For the current application it is properly the solution with the bulk gratings which is most obvious to test first, as these are widely obtainable commercially. An other advantage with the use of bulk gratings is that the tuning of the SSFS could be controlled by changing the temporal duration of the input pulse to the LSF and not by changing the amplification level. This would ensure a more constant power output. An alternative to dispersion compensation would be to have a mode-locked fibre-based oscillator, which could deliver pulses with temporal duration in the femtosecond range and with a pulse energy of several nanojoules. This would ensure that the required length of LSF is on a centimetre scale and not on a scale of tens of metre and thereby it should be possible to keep the fibre straight and avoid the intermodal Čerenkov process. In this case the accumulated SPM in the mode-converter fibre due to the high peak power of a femtosecond pulse

could be an issue and a more suited form of mode-conversion could be performed with phase plates. If the bulk gratings was used to provide the dispersion compensation, then phase plates could also be considered as the all fibre criterion would already be void.

To reduce the loss of the splice between mode-converter fibre and the LSF and to understand why the splice between the LSF and the fibres for shifting the soliton to longer wavelength failed the parameter space of the combination of the fusion and gas-line-burner splice should be investigated more systematically. However, before undertaking this task it would be advisable to investigate the feasibility of tapering one of the fibres before splicing the fibres together or using one or more bridge fibres. If the tapering approach is chosen, care should be taken if the fibre to be tapered contains a mode-crossing, as this will move in wavelength as the fibre is tapered. For the evaluation of the splice loss between the FMFs and in general for the experimental investigations, the output should have been imaged and analysed with S^2 technique [103].

With the optimisation of the triple-clad fibre design some interesting intermodal non-linear effects was observed, however, the mode-crossing issue turned out to be more complex than first anticipated. Therefore, in retrospect for experimental simplicity a more viable path is perhaps to utilise a fibre which can provide a high soliton pulse energy and anomalous dispersion without any mode-crossing issue. This could potentially be achieved with a double-clad fibre, where the inner core is single-moded and the outer core is large and highly multi-moded. In this type of fibre the dispersion would be anomalous for some of the $LP_{0,x}$ mode and as the outer core is large the effective area would also be large and thereby the soliton pulse energy.

Appendix A

Additional Material to the Chapters

A.1 Theory

A.1.1 Maxwell's Equations

Definition of the Applied Fourier Transform

In Chap. 2 the derivations are carried out with the following definition of the Fourier transform

$$\tilde{E}(\omega) = \int_t E(t) \exp[i\omega t] \, \mathrm{d}t, \tag{A.1.1}$$

$$E(t) = \frac{1}{2\pi} \int_\omega \tilde{E}(\omega) \exp[-i\omega t] \, \mathrm{d}\omega. \tag{A.1.2}$$

Vector Identities

The vector identities are

$$\boldsymbol{\nabla} \times \boldsymbol{\nabla} \times \mathbf{V} = \boldsymbol{\nabla}(\boldsymbol{\nabla} \cdot \mathbf{V}) - \boldsymbol{\nabla}^2 \mathbf{V}, \tag{A.1.3}$$

$$\boldsymbol{\nabla} \cdot (\psi \mathbf{V}) = \psi \boldsymbol{\nabla} \cdot \mathbf{V} + \mathbf{V} \cdot \boldsymbol{\nabla} \psi. \tag{A.1.4}$$

Here $\mathbf{V}$ is a vector and ψ is a scalar both dependent on the position in space.

A.1.2 Pulse-Propagation

Separation of Variables

If Eq. 2.1.19 is considered without any non-linear induced polarisation contributions and Eq. 2.2.2 is inserted, then the following is obtained

$$\begin{aligned}
&- \tilde{F} \exp\left[i\beta\left(\omega_0\right) z\right] \boldsymbol{\nabla}_z^2 \tilde{\mathcal{A}} - \tilde{\mathcal{A}} \exp\left[i\beta\left(\omega_0\right) z\right] \boldsymbol{\nabla}_\perp^2 \tilde{F} \\
&- \left(i\beta\left(\omega_0\right)\right)^2 \tilde{F}\tilde{\mathcal{A}} \exp\left[i\beta\left(\omega_0\right) z\right] - 2\left(i\beta\left(\omega_0\right)\right) \tilde{F} \exp\left[i\beta\left(\omega_0\right) z\right] \frac{\partial}{\partial z}\tilde{\mathcal{A}} \\
&= \frac{\omega^2}{c^2}\varepsilon_r \tilde{F}\tilde{\mathcal{A}} \exp\left[i\beta\left(\omega_0\right) z\right]. \qquad \text{(A.1.5)}
\end{aligned}$$

The variables are seprated by multiplying with $\frac{1}{\tilde{F}\tilde{\mathcal{A}}\exp[i\beta(\omega_0)z]}$, which yields

$$\frac{1}{\tilde{F}}\boldsymbol{\nabla}_\perp^2 \tilde{F} + \frac{\omega^2}{c^2}\varepsilon_r = \left(\beta'\right)^2 = -\frac{1}{\tilde{\mathcal{A}}}\boldsymbol{\nabla}_z^2 \tilde{\mathcal{A}} - \frac{1}{\tilde{\mathcal{A}}} 2i\beta\left(\omega_0\right) \frac{\partial}{\partial z}\tilde{\mathcal{A}} + \beta^2\left(\omega_0\right). \qquad \text{(A.1.6)}$$

The equation is separated into two independent homogeneous differential equations

$$\boldsymbol{\nabla}_\perp^2 \tilde{F} + \left(\frac{\omega^2}{c^2}\varepsilon_r - \left(\beta'\right)^2\right)\tilde{F} = 0, \qquad \text{(A.1.7)}$$

$$\boldsymbol{\nabla}_z^2 \tilde{\mathcal{A}} + 2i\beta\left(\omega_0\right)\frac{\partial}{\partial z}\tilde{\mathcal{A}} + \left(\left(\beta'\right)^2 - \beta^2\left(\omega_0\right)\right)\tilde{\mathcal{A}} = 0. \qquad \text{(A.1.8)}$$

In this case, where the effects from the non-linear contribution to the induced polarisation have been disregarded, β' is given as

$$\beta' = \beta = \frac{\omega}{c} n_{eff}. \qquad \text{(A.1.9)}$$

Perturbation

The third-order induced polarisation is introduced into the equation as a perturbation to the relative dielectric constant as

$$\varepsilon_r = \varepsilon^0 + \eta\Delta\varepsilon, \qquad \text{(A.1.10)}$$

where $\Delta\varepsilon$ is the perturbation and $\eta \in [0;1]$, this results in a perturbation of both $\tilde{F}$ and $\left(\beta'\right)^2$ given as

$$\tilde{F} = \tilde{F}^0 + \eta\Delta\tilde{F}, \qquad \text{(A.1.11)}$$

$$\left(\beta'\right)^2 = \beta^2 + \eta\Delta\beta^2. \qquad \text{(A.1.12)}$$

The homogeneous differential equations in Eq. 2.2.3 are then given as

$$\boldsymbol{\nabla}_\perp^2 \left(\tilde{F}^0 + \eta\Delta\tilde{F}\right) + \left(\frac{\omega^2}{c^2}\left(\varepsilon^0 + \eta\Delta\varepsilon\right) - \left(\beta^2 + \eta\Delta\beta^2\right)\right)\left(\tilde{F}^0 + \eta\Delta\tilde{F}\right) = 0. \tag{A.1.13}$$

Collecting the terms with respect to the order of η, yields

$$\eta^0: \quad \boldsymbol{\nabla}_\perp^2 \tilde{F}^0 + \left(\frac{\omega^2}{c^2}\varepsilon^0 - (\beta)^2\right)\tilde{F}^0 = 0, \tag{A.1.14}$$

$$\eta^1: \quad \boldsymbol{\nabla}_\perp^2 \Delta\tilde{F} + \frac{\omega^2}{c^2}\varepsilon^0\Delta\tilde{F} + \frac{\omega^2}{c^2}\Delta\varepsilon\tilde{F}^0 - \beta^2\Delta\tilde{F} - \Delta\beta^2\tilde{F}^0 = 0. \tag{A.1.15}$$

Eq. A.1.14 is the homogeneous differential equation. Eq. A.1.15 is the first-order correction to the homogeneous differential equation, which is the correction that is considered in the following. Multiplying with $\left(\tilde{F}^0\right)^*$ and integrating results in

$$\begin{aligned}\Delta\beta^2 \int_A \left|\tilde{F}^0\right|^2 \mathrm{d}A =& \frac{\omega^2}{c^2}\int_A \Delta\varepsilon \left|\tilde{F}^0\right|^2 \mathrm{d}A + \int_A \Big[\left(\tilde{F}^0\right)^* \left(\boldsymbol{\nabla}_\perp^2 \Delta\tilde{F}\right) \\ &+ \left(\tilde{F}^0\right)^* \frac{\omega^2}{c^2}\varepsilon^0\Delta\tilde{F} - \left(\tilde{F}^0\right)^* \beta^2\Delta\tilde{F}\Big]\,\mathrm{d}A. \end{aligned} \tag{A.1.16}$$

If A.1.14 is complex conjugated and multiply by $\Delta\tilde{F}$, then this gives

$$\Delta\tilde{F}\boldsymbol{\nabla}_\perp^2 \left(\tilde{F}^0\right)^* + \Delta\tilde{F}\left(\frac{\omega^2}{c^2}\left(\varepsilon^0\right)^* - (\beta^*)^2\right)\left(\tilde{F}^0\right)^* = 0. \tag{A.1.17}$$

This can be integrated over the transverse plane subtracted from A.1.16 to give

$$\begin{aligned}\Delta\beta^2 \int_A \left|\tilde{F}^0\right|^2 \mathrm{d}A =& \frac{\omega^2}{c^2}\int_A \Delta\varepsilon \left|\tilde{F}^0\right|^2 \mathrm{d}A + \int_A \Big[\left(\tilde{F}^0\right)^* \left(\boldsymbol{\nabla}_\perp^2 \Delta\tilde{F}\right) \\ &- \Delta\tilde{F}\left(\boldsymbol{\nabla}_\perp^2 \left(\tilde{F}^0\right)^*\right) + \left(\tilde{F}^0\right)^* \frac{\omega^2}{c^2}\left(\varepsilon^0 - \left(\varepsilon^0\right)^*\right)\Delta\tilde{F} \\ &- \left(\tilde{F}^0\right)^* \left(\beta^2 - (\beta^*)^2\right)\Delta\tilde{F}\Big]\,\mathrm{d}A. \end{aligned} \tag{A.1.18}$$

If ε^0 and β are purely real, the equation reduces to

$$\begin{aligned}\Delta\beta^2 \int_A \left|\tilde{F}^0\right|^2 \mathrm{d}A =& \frac{\omega^2}{c^2}\int_A \Delta\varepsilon \left|\tilde{F}^0\right|^2 \mathrm{d}A + \int_A \Big[\left(\tilde{F}^0\right)^* \left(\boldsymbol{\nabla}_\perp^2 \Delta\tilde{F}\right) \\ &- \Delta\tilde{F}\left(\boldsymbol{\nabla}_\perp^2 \left(\tilde{F}^0\right)^*\right)\Big]\,\mathrm{d}A. \end{aligned} \tag{A.1.19}$$

By applying Green's theorem it is realised that

$$\int_A \left[\left(\tilde{F}^0 \right)^* \left(\boldsymbol{\nabla}_\perp^2 \Delta\tilde{F} \right) - \Delta\tilde{F} \left(\boldsymbol{\nabla}_\perp^2 \left(\tilde{F}^0 \right)^* \right) \right] \mathrm{d}A = 0. \tag{A.1.20}$$

Therefore, the correction to β^2 is given as

$$\Delta\beta^2 = \frac{\omega^2}{c^2} \frac{\int_A \Delta\varepsilon \left| \tilde{F} \right|^2 \mathrm{d}A}{\int_A \left| \tilde{F} \right|^2 \mathrm{d}A}. \tag{A.1.21}$$

Unit of the Complex Amplitude

The unit of W is related to the optical power and is defined as

$$\tilde{P} = \int_A \tilde{I} \mathrm{d}A, \tag{A.1.22}$$

where $\tilde{I}$ is the intensity, which is integrated over the detection area. The power flow of a time-average signal is determined by the real value of the Poynting vector [104]

$$\tilde{\mathbf{P}} = \int \frac{1}{2} \Re \left[\tilde{\mathbf{E}} \times \tilde{\mathbf{H}}^* \right], \tag{A.1.23}$$

where $\Re$ denotes the real part. For an electric field polarised in the **x** direction and travelling in the **z** direction, the Poynting vector is rewritten as

$$\tilde{P} = \frac{1}{2} \int_A \eta \left| \tilde{E} \right|^2 \mathrm{d}A, \tag{A.1.24}$$

where η is the intrinsic impedance of the material and $\tilde{E}$ is the amplitude. This can be rewritten as

$$\tilde{P} = \frac{1}{2} c\varepsilon_0 \int_A n \left| \tilde{E} \right|^2 \mathrm{d}A, \tag{A.1.25}$$

where the integral is now over the squared amplitude of the electric field and the index of refraction. In the next step the amplitude of the electric field is separated into a transverse and longitudinal component and the power is written as

$$\tilde{P} = \frac{1}{2} c\varepsilon_0 \left| \tilde{\mathcal{A}} \right|^2 \int_A n \left| \tilde{F} \right|^2 \mathrm{d}A. \tag{A.1.26}$$

Eq. A.1.26 is often approximated by moving the index of refraction outside the integral. The error is negligible for an almost homogeneous material, which is approximately true for a silica-based fibre

$$\tilde{P} = \frac{1}{2} c\varepsilon_0 n_{eff} \left|\tilde{\mathcal{A}}\right|^2 \int_A \left|\tilde{F}\right|^2 \mathrm{d}A, \tag{A.1.27}$$

where n_{eff} is the effective index of the light in the fibre. In the next step power is written as

$$P = \left|\tilde{A}\right|^2. \tag{A.1.28}$$

To convert the complex amplitude to the unit of $\sqrt{W}$, $\tilde{\mathcal{A}}$ is to be replaced with the following expression

$$\tilde{\mathcal{A}} = \frac{\tilde{A}}{\sqrt{\frac{1}{2} c\varepsilon_0 n_{eff} \int_A \left|\tilde{F}\right|^2 \mathrm{d}A}}, \tag{A.1.29}$$

where $\tilde{A}$ is the new variable with the unit of $\sqrt{W}$.

Moving Time-Frame

Introducing a moving frame with the time $T = t - \frac{z}{v_g^{\mathrm{ref}}} = t - \beta_1^{\mathrm{ref}} z$ and $x = z$, gives a change to the derivatives as follows

$$\frac{\partial A}{\partial z} = \frac{\partial A}{\partial x}\frac{\partial x}{\partial z} + \frac{\partial A}{\partial T}\frac{\partial T}{\partial z} = \frac{\partial A}{\partial x} - \beta_1^{\mathrm{ref}} \frac{\partial A}{\partial T}, \tag{A.1.30}$$

$$\frac{\partial A}{\partial t} = \frac{\partial A}{\partial t}\frac{\partial t}{\partial z} + \frac{\partial A}{\partial T}\frac{\partial T}{\partial t} = \frac{\partial A}{\partial T}. \tag{A.1.31}$$

All Possible Frequency Contributions

The double integral over $\tilde{q}_{A,B,C,D}$ is rewritten as

$$\begin{aligned}\int_{\omega_1}\int_{\omega_2} \tilde{q}_{A,B,C,D} \mathrm{d}\omega_2 \mathrm{d}\omega_1 = \int_A \tilde{F}^*_{N,A}(\omega_\sigma) \int_{\omega_1}\int_{\omega_2} \tilde{R}(\omega_\sigma - \omega_1)\, \tilde{A}_B(\omega_1) \\ \times \tilde{F}_{N,B}(\omega_1)\, \tilde{A}^*_C(\omega_\sigma - \omega_1 - \omega_2)\, \tilde{F}^*_{N,C}(\omega_\sigma - \omega_1 - \omega_2) \\ \times \tilde{A}_D(\omega_2)\, \tilde{F}_{N,D}(\omega_2)\, \mathrm{d}\omega_2 \mathrm{d}\omega_1 \mathrm{d}A,\end{aligned} \tag{A.1.32}$$

where the transverse field distribution is written in the normalised form

$$\tilde{F}_N = \frac{\tilde{F}}{\sqrt{\int_A \left|\tilde{F}\right|^2 \mathrm{d}A}}. \tag{A.1.33}$$

Often when the Generalised Non-Linear Schrödinger Equation (GNLSE) is derived, the frequency dependence of the transverse field is disregarded and all the transverse fields are evaluated at the same frequency of ω_σ. For the derivation of the Transverse-Field Dispersion in the Generalised Non-Linear Schrödinger Equation (TFD-GNLSE) the correct dispersion of the transverse fields are incorporated into the equation by keeping the longitudinal amplitude and the transverse field distribution for each electric field together. In the following $\tilde{G} = \tilde{F}\tilde{A}$, then Eq. A.1.32 is given as

$$\int_{\omega_1}\int_{\omega_2} \tilde{q}_{A,B,C,D}\mathrm{d}\omega_2\mathrm{d}\omega_1 = \int_A \tilde{F}^*_{N,A}(\omega_\sigma) \int_{\omega_1}\int_{\omega_2} \tilde{R}(\omega_\sigma - \omega_1)\,\tilde{G}_B(\omega_1) \times \tilde{G}^*_C(\omega_\sigma - \omega_1 - \omega_2)\,\tilde{G}_D(\omega_2)\,\mathrm{d}\omega_2\mathrm{d}\omega_1\mathrm{d}A, \tag{A.1.34}$$

The integral over ω_2 in A.1.34 can be shown to be equal to a convolution by performing the following transform of variables $\xi = \omega_2$ and $\zeta = \omega_\sigma - \omega_1$. The integral over ω_2 is then written as

$$\int_{\omega_2} \tilde{G}^*_C(\omega_\sigma - \omega_1 - \omega_2)\tilde{G}_D(\omega_2)\,\mathrm{d}\omega_2 = \int_\xi \tilde{G}^*_C(\zeta - \xi)\,\tilde{G}_D(\xi)\,\mathrm{d}\xi \tag{A.1.35}$$

$$= \mathcal{F}\left\{\mathcal{F}^{-1}\left\{\tilde{G}^*_C(\zeta)\right\}\mathcal{F}^{-1}\left\{\tilde{G}_D(\zeta)\right\}\right\} \tag{A.1.36}$$

$$= \tilde{J}(\zeta) = \tilde{J}(\omega_\sigma - \omega_1). \tag{A.1.37}$$

The $\mathcal{F}$ denoted the Fourier transform from time to frequency and $\mathcal{F}^{-1}$ denoted the Fourier transform from frequency to time. As with the integral over ω_2, the integral over ω_1 in A.1.34 can be shown to be a convolution. This is achieved by considering $\tilde{R}(\omega_\sigma - \omega_1)$ and $\tilde{J}(\omega_\sigma - \omega_1)$ as one function $\tilde{RJ}(\omega_\sigma - \omega_1) = \tilde{R}(\omega_\sigma - \omega_1)\,\tilde{J}(\omega_\sigma - \omega_1)$. The integral over ω_1 is then written as

$$\int_{\omega_1} \tilde{G}_B(\omega_1)\,\tilde{RJ}(\omega_\sigma - \omega_1)\,\mathrm{d}\omega_1 = \mathcal{F}\left\{\mathcal{F}^{-1}\left\{\tilde{G}_B(\omega_\sigma)\right\}\mathcal{F}^{-1}\left\{\tilde{RJ}(\omega_\sigma)\right\}\right\}. \tag{A.1.38}$$

Therefore, is it possible to write the double frequency integral as Fourier transforms, which numerically is a significant advantage. The double integral of A.1.34 is written as

$$\int_{\omega_1}\int_{\omega_2}\tilde{q}_{A,B,C,D}\mathrm{d}\omega_2\mathrm{d}\omega_1 = \int_A \tilde{F}^*_{N,A}\mathcal{F}\left\{\mathcal{F}^{-1}\left\{\tilde{G}_B\right\}\mathcal{F}^{-1}\left\{\tilde{R}\right.\right. \\ \left.\left.\times\mathcal{F}\left\{\mathcal{F}^{-1}\left\{\tilde{G}^*_C\right\}\mathcal{F}^{-1}\left\{\tilde{G}_D\right\}\right\}\right\}\right\}\mathrm{d}A. \tag{A.1.39}$$

By using Eq. A.1.39 the correct dispersion of the transverse field is obtained and this is applied in the TFD-GNLSE. In the case of the GNLSE where the dispersion of the transverse field for the interacting electric fields is disregarded, the derivation follows the one outlined above, however, in this case $\tilde{G} = \tilde{A}$ and the transverse field overlap integral is moved outside the double frequency integrals in Eq. A.1.32 resulting in an alternate version of Eq. A.1.39 given as

$$\int_{\omega_1}\int_{\omega_2}\tilde{q}_{A,B,C,D}\mathrm{d}\omega_2\mathrm{d}\omega_1 = \frac{1}{A_{eff,A,B,C,D}}\mathcal{F}\left\{\mathcal{F}^{-1}\left\{\tilde{A}_B\right\}\mathcal{F}^{-1}\left\{\tilde{R}\right.\right. \\ \left.\left.\times\mathcal{F}\left\{\mathcal{F}^{-1}\left\{\tilde{A}^*_C\right\}\mathcal{F}^{-1}\left\{\tilde{A}_D\right\}\right\}\right\}\right\}, \tag{A.1.40}$$

where it is utilised that the transverse field overlap integral is the inverse of the effective area.

Verification of the Numerical Implementation of the Transverse-Field Dispersion in the Generalised Non-Linear Schrödinger Equation

The fibre data used for the verification of the numerical implementation is presented in Sec. 4.1.1. The fibre is the left-sided fibre (LSF), which has a radial symmetric refractive index profile and therefore it is advantageous to solve the transverse problem in cylindrical coordinates.

A comparison test between the standard implementation of the GNLSE with the fourth root method and the implementation of the TFD-GNLSE is carried out in this section. This is performed to verify the TFD-GNLSE implementation. The test example is a higher order soliton in the LSF. The number of points used on the time/frequency grid is 2^{13}, the time discretisation is 10 fs, the centre wavelength of the simulation window is 1030 nm, input wavelength of the pulse is 1064 nm, the shape of the pulse intensity is a sech^2, the full-width at

half-maximum (FWHM) of the pulse intensity is 400 fs, the input peak power of the pulse is 4236.4 W, the intensity-dependent refractive index of the fibre is 2.6×10^{-20} $\frac{\mathrm{m}^2}{\mathrm{W}}$, the f_R ratio is 0.18, the length of the fibre is 10 m and the loss is neglected. The simulation is performed with the Fourth-Order Runge-Kutta in the Interaction-Picture (RK4IP) method [42] and the efficient adaptive step-size method [91], with a local error limit of 10^{-7} for the conserved quantity, which is proportional to the photon number. The radial grid is made by using 18 grid points spanning from 0 μm to 12 μm. In Fig. A.1 the effective area for the $\mathrm{LP}_{0,2}$ mode is calculated with the use of the Gauss-Legendre quadrature and 18 radial grid points spanning from 0 μm to 12 μm is shown together with the discrepancy from the correct calculation of the effective area. It is observed that with 18 grid points it is possible to capture the

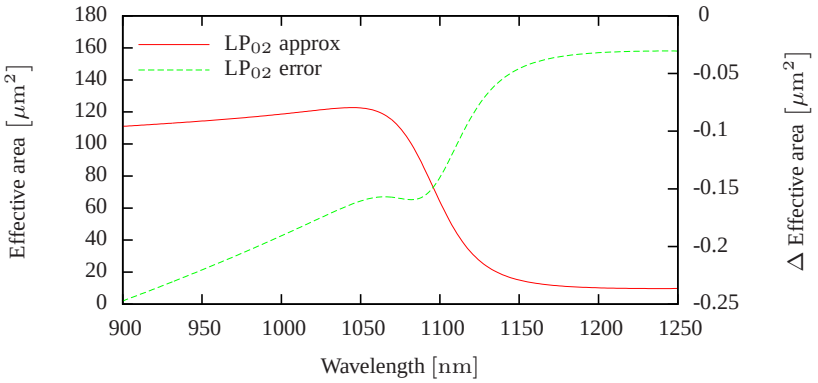

Figure A.1: The effective area calculated with the Gauss-Legendre quadrature method using 18 radial grid points. The error is with respect to the calculation of the effective area without applying the Gauss-Legendre quadrature method.

dispersion of the normalised field distributions without any significant error. The number of radial grid points is a trade-off between computational accuracy and computation time. The group-velocity dispersion curve is shown in Fig. 4.5a.

The spectral characteristics for the simulated soliton propagation are sampled through the fibre and shown in Fig. A.2 for both implementations. By comparing the two sub-figures A.2a and A.2b, it is observed that the two implementations are in good agreement with respect to the pulse evolution for the higher-order soliton in the $\mathrm{LP}_{0,2}$ mode, where it is only intramodal effects that is considered. The agreement between the two implementations is expected as the change in the effective area,

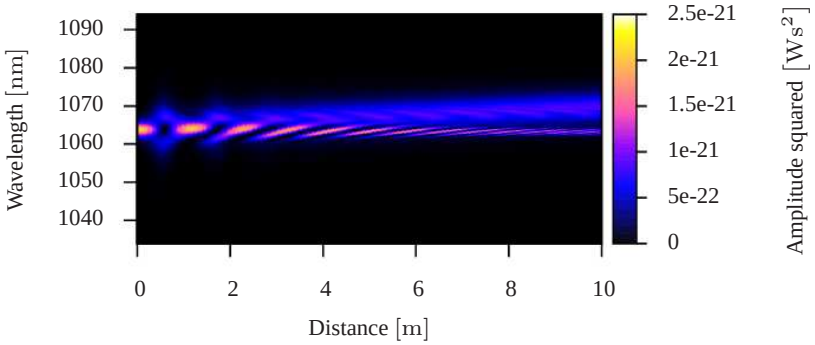

(a) Simulation using the implementation of the GNLSE with the fourth root method of the effective area.

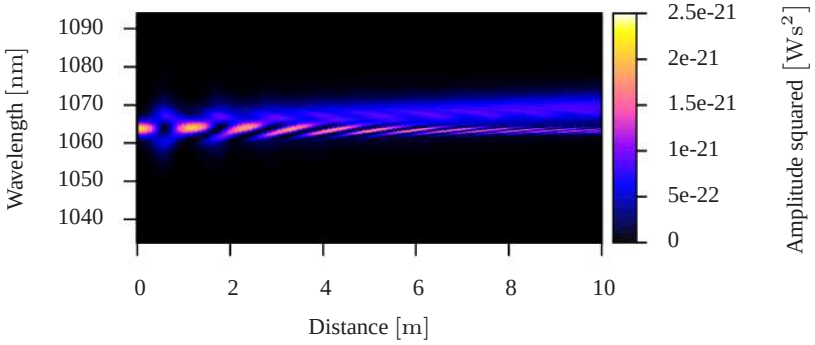

(b) Simulation using the implementation of the TFD-GNLSE with the correct dispersion of the transverse field distribution.

Figure A.2: Spectral characteristics sampled through the fibre for both numerical implementations.

within the bandwidth where the higher order soliton evolves, is close to linear and therefore the fourth root method is a good approximation. From Fig. A.2 it is observed that the higher order soliton breathes like a 2nd order soliton, but is perturbed by the Raman effect and starts to shift towards longer wavelengths. In Fig. A.3 the final output spectra for both the GNLSE and the TFD-GNLSE are shown. The discrepancy

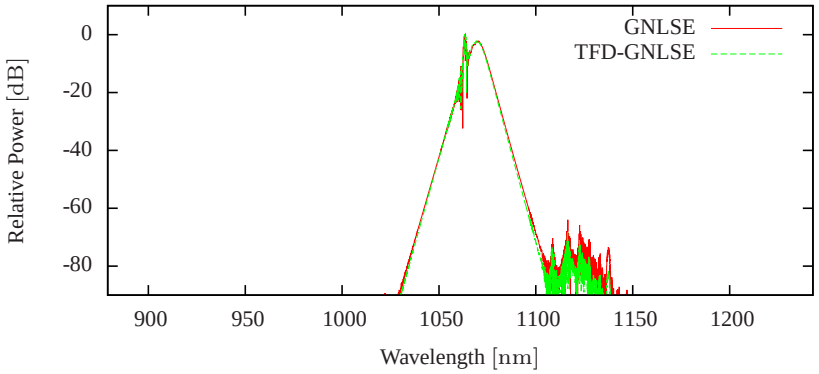

Figure A.3: The output spectrum for both the GNLSE and TFD-GNLSE implementation.

is not noticeable for the main part of the spectra. In Fig. A.4 the final output pulse traces for both the GNLSE and the TFD-GNLSE are shown. There is a discrepancy regarding the accumulated group-delay

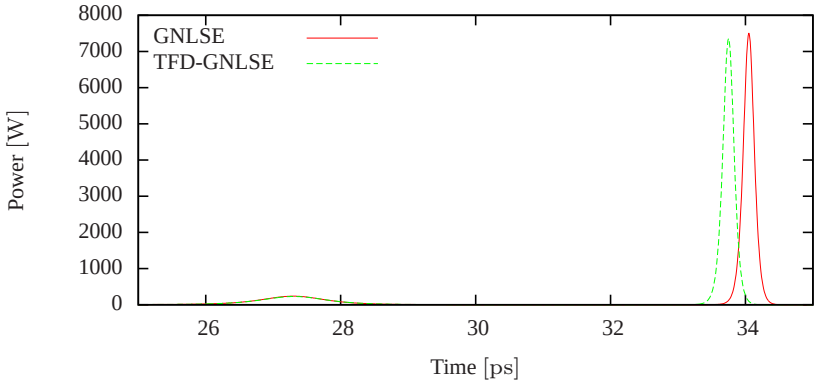

Figure A.4: The output pulse trace for both the GNLSE and TFD-GNLSE implementation.

experience by the soliton between the GNLSE and the TFD-GNLSE.

A.2 Few-Moded Fibres

A.2.1 Characterisation

Sliding Fourier Transform Window - LSF

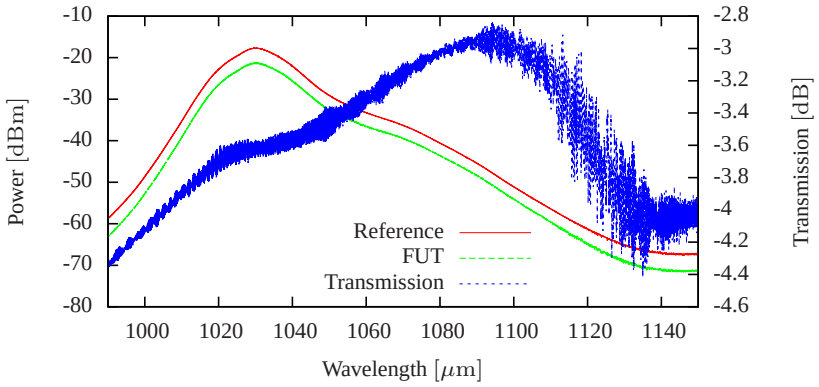

Figure A.5: The recorded data from the interferometric measurement.

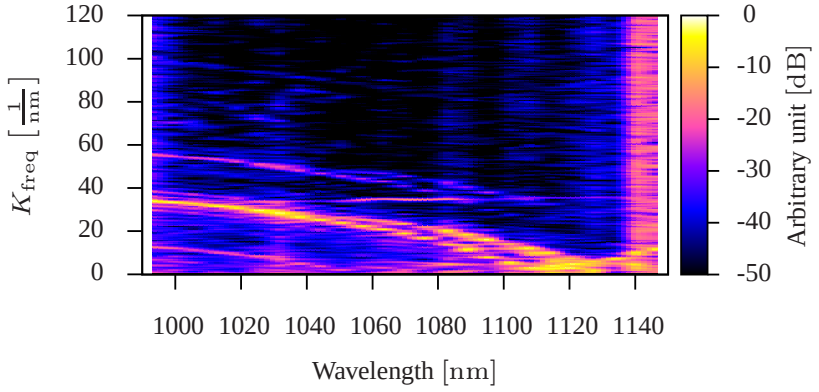

Figure A.6: The sliding Fourier transform window method applied to the interferometric data shown in Fig. A.5. It can be verified that the sampling is sufficient to resolve the oscillations.

Sliding Fourier Transform Window - RSF

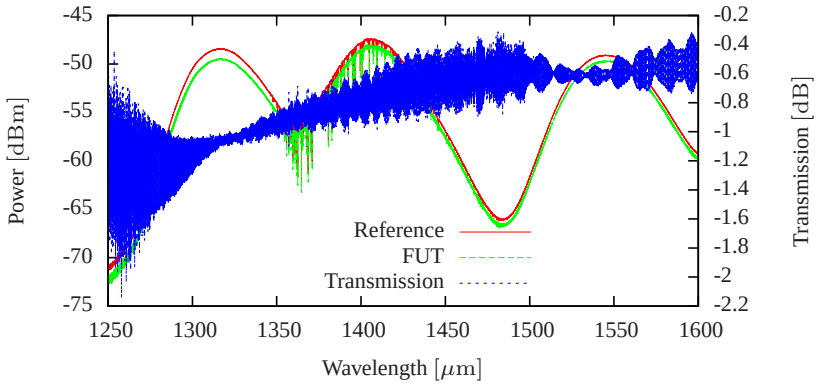

Figure A.7: The recorded data from the interferometric measurement.

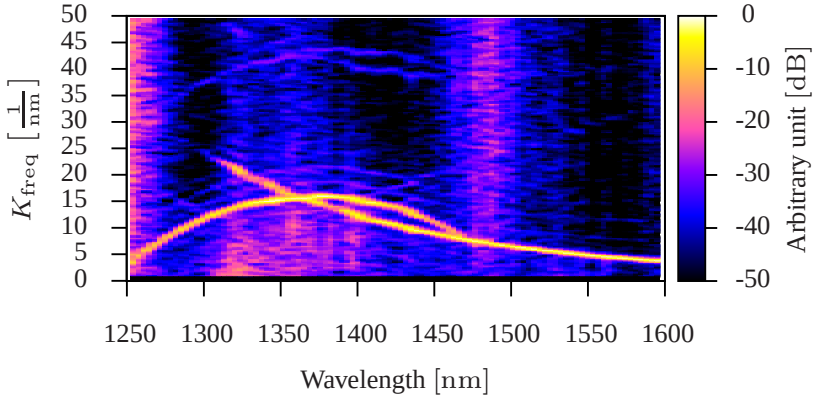

Figure A.8: The sliding Fourier transform window method applied to the interferometric data shown in Fig. A.7. It can be verified that the sampling is sufficient to resolve the oscillations.

A.3 Excitation of the $LP_{0,2}$ Mode

A.3.1 Splicing of Few-Moded Fibres

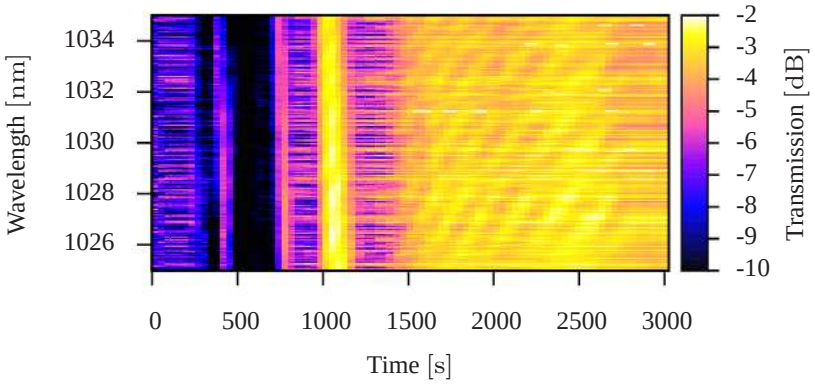

(a) The measured transmission.

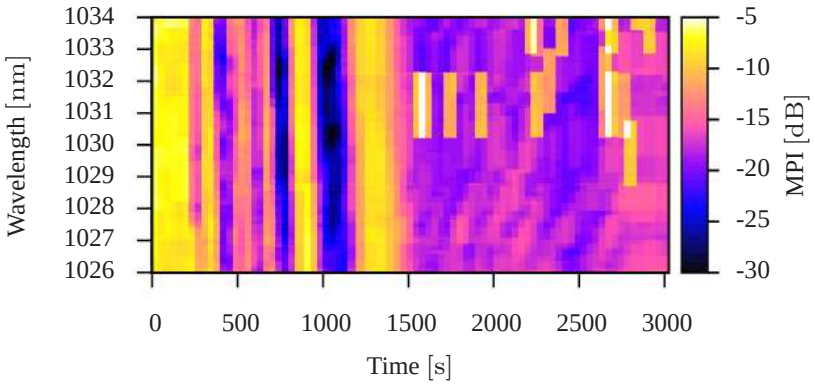

(b) The calculated MPI. The white and orange coloured blocks after an experimental run-time of 1500 s is an effect of some noise spikes from the ASE source.

Figure A.9: The gas-line-burner splice evolution. The length of LSF was 50 m and the resolution of the OSA was 0.02 nm.

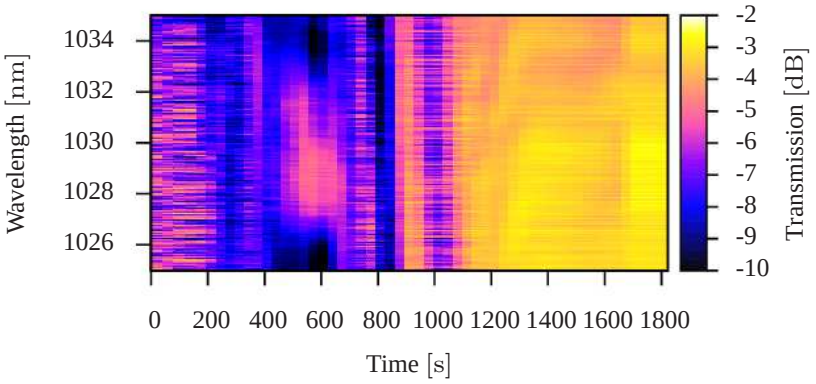

(a) The measured transmission.

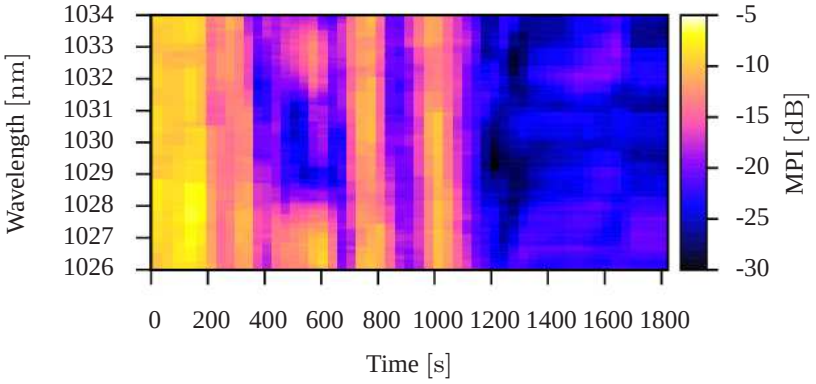

(b) The calculated MPI.

Figure A.10: The gas-line-burner splice evolution. The splice process is stopped just shortly after an experimental run-time of 1000 s and the gas-line burners are moved away. The length of LSF was 70 m and the resolution of the OSA was 0.02 nm.

A.4 Fibre-Based Oscillators

A.4.1 Higher-Order-Mode Dispersion-Balanced Laser

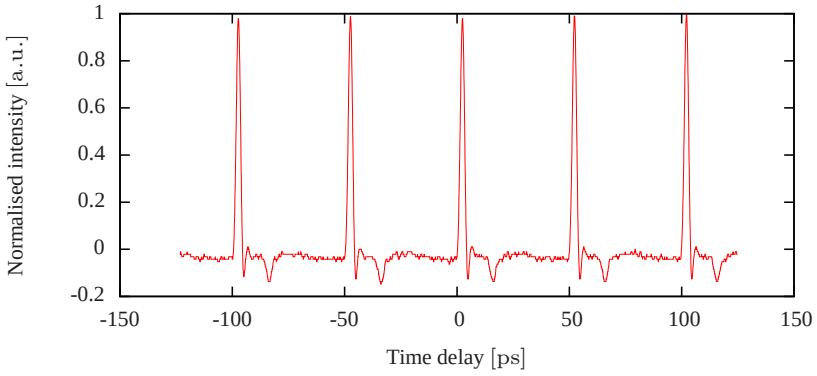

Figure A.11: The measured RF trace of the HOM dispersion-balanced fibre laser. The pulse train has a small amplitude variation from pulse to pulse.

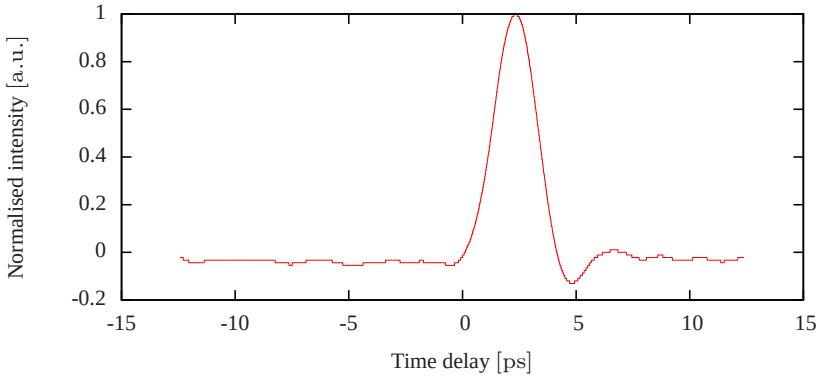

Figure A.12: Single pulse RF trace of the HOM dispersion-balanced fibre laser. This is a close-up of the RF trace is shown in Fig. A.12

A.4.2 All-Normal Dispersive Polarisation-Maintaining Laser

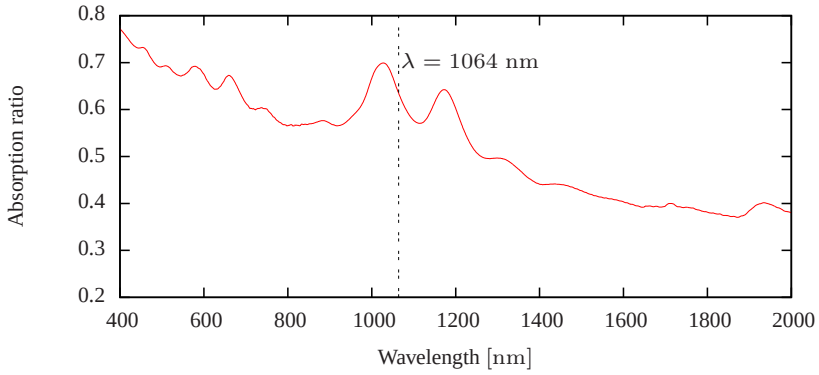

Figure A.13: The measured absorption spectrum for the carbon-nano-tube.

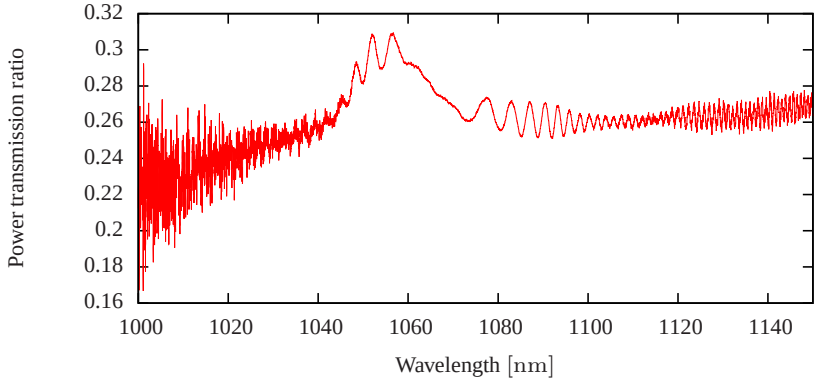

Figure A.14: The measured transmission spectrum for the carbon-nano-tube.

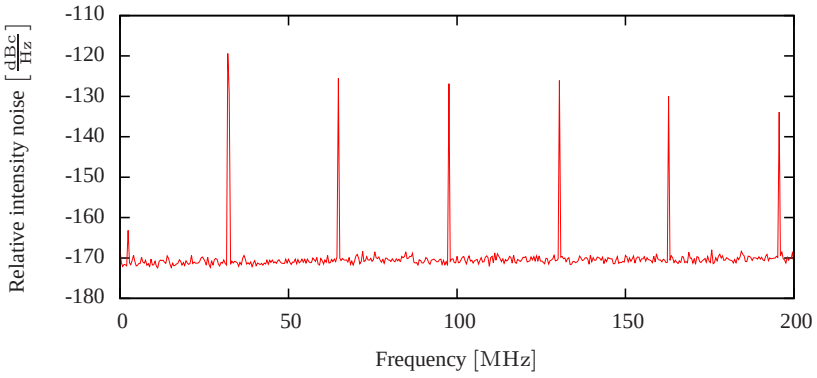

Figure A.15: The measured RIN for the first few harmonics for the ANDi PM laser.

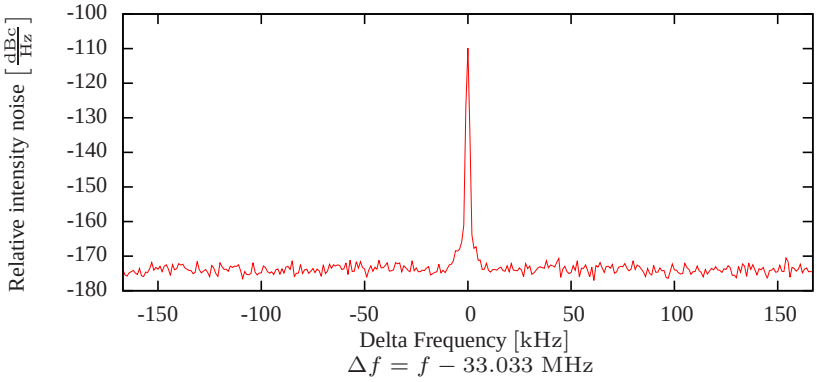

Figure A.16: A close-up on the first harmonic from Fig. A.15. The repetition rate of the laser is 33.033 MHz.

To determine the convergence of the pulse, two different definitions of the FWHM are used, they are the maximum and the minimum FWHM. The maximum FWHM is defined to give largest possible width for a given trace at the signal half maximum value. The minimum FWHM is defined to give smallest possible width for a given trace at the signal half maximum value. Maximum FWHM and minimum FWHM are identical for a converged single pulse. However, in the initial part of the mode-locking process these two measures differ as the pulse has a lot of structure.

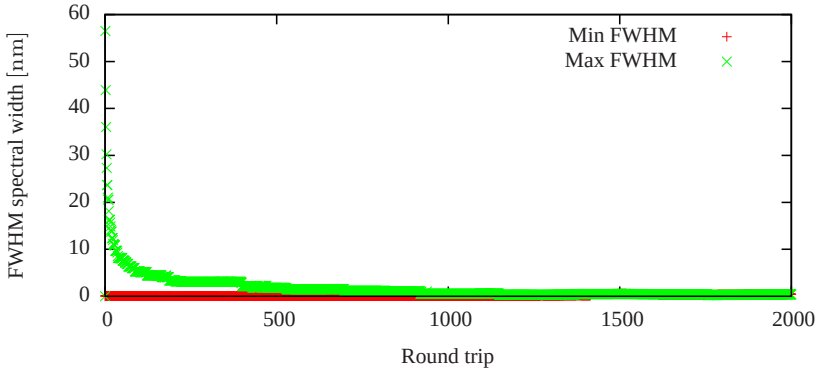

Figure A.17: An example of the mode-locking dynamics in the spectral domain.

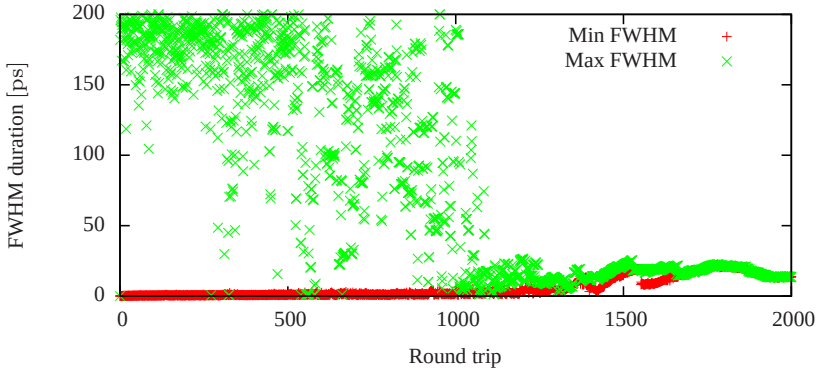

Figure A.18: An example of the mode-locking dynamics in the temporal domain. The temporal domain takes a significant large number of round-trips to reach convergence compared to the spectral domain.

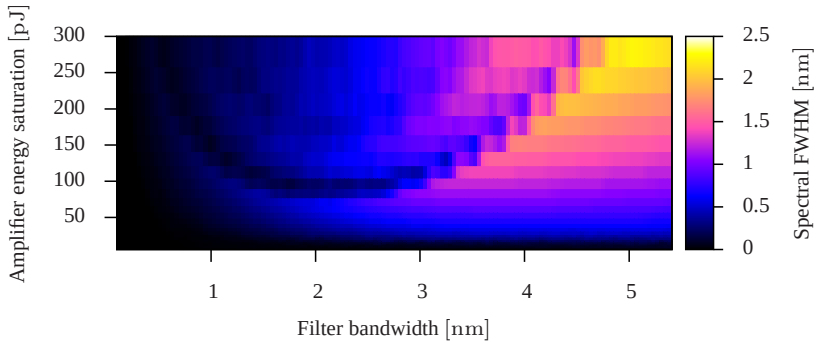

Figure A.19: The corresponding FWHM of the spectrum for the pulse type map shown in Fig. 5.15a.

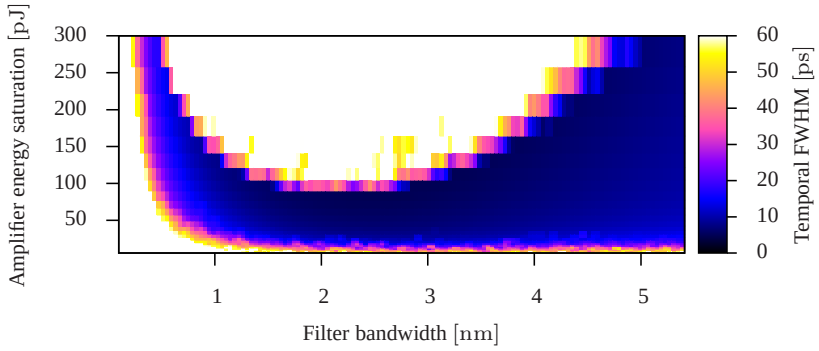

Figure A.20: The corresponding FWHM of the pulse duration for the pulse type map shown in Fig. 5.15a.

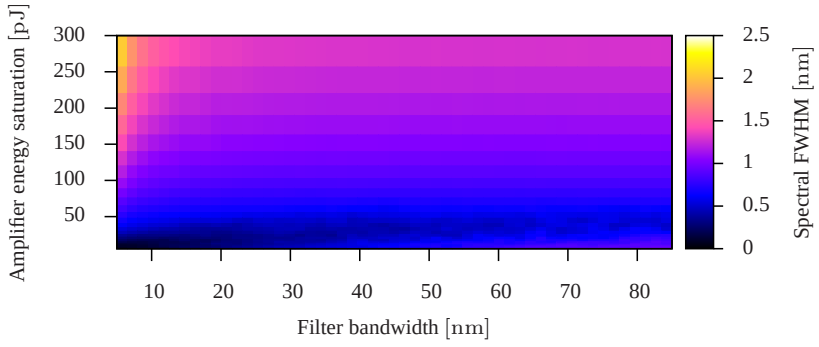

Figure A.21: The corresponding FWHM of the spectrum for the pulse type map shown in Fig. A.21.

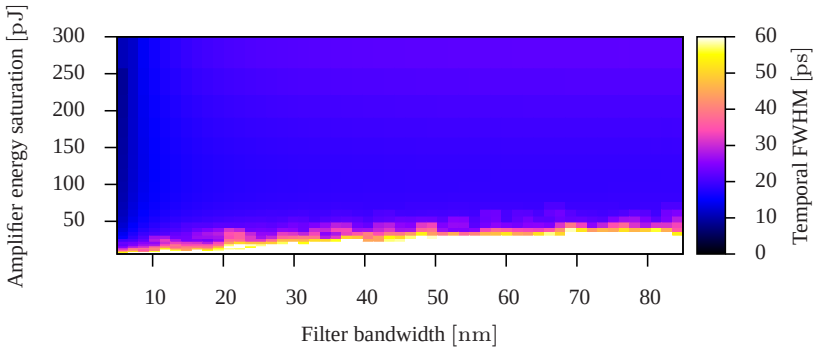

Figure A.22: The corresponding FWHM of the pulse duration for the pulse type map shown in Fig. A.22.

Similar to the variation of the bandwidth of the filter, the group velocity dispersion is varied for the two passive fibres. In this case there is no band-pass filter element included. The pulse type map is shown in Fig. A.23, where the group velocity dispersion of the two passive fibres are varied together along with the energy saturation of the amplifier.

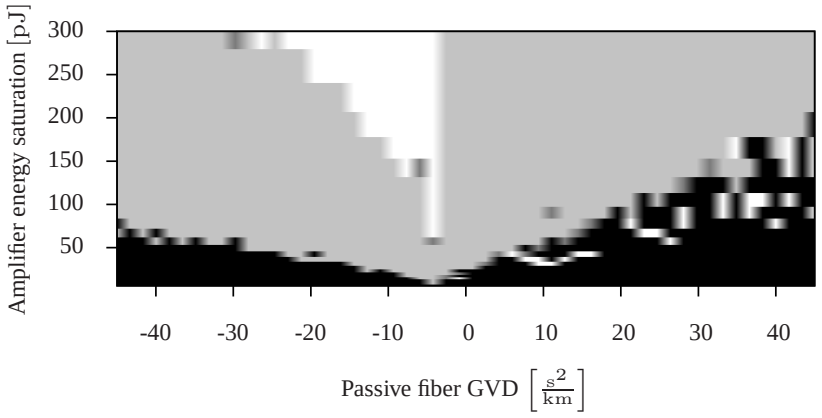

Figure A.23: Pulse type map for the variation of the group velocity dispersion of the passive fibres. The relation to the grey-scale map is as follows: Black is a CW solution, dark grey is an undecided pulse solution, light grey is single-pulse solution, and white is a multi-pulse solution. The spacing between the steps in the amplifier energy saturation are logarithmic.

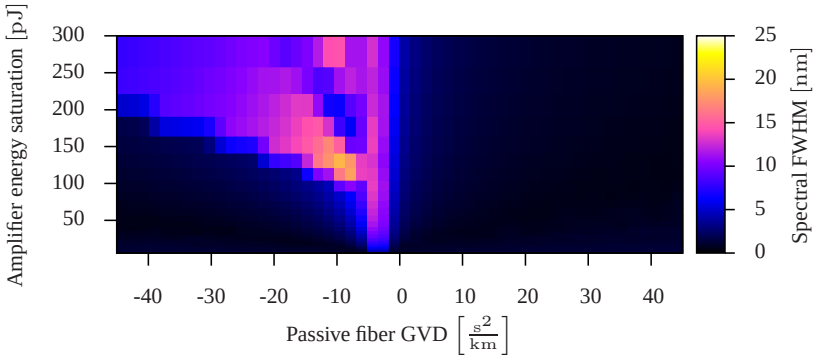

Figure A.24: The corresponding FWHM of the spectrum is shown of the pulse type map shown in Fig. A.23.

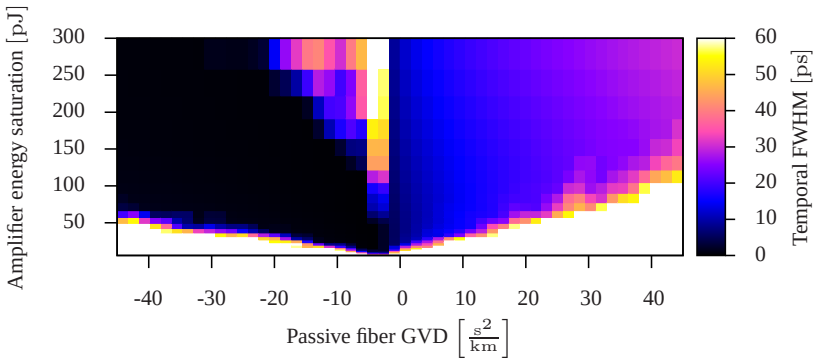

Figure A.25: The corresponding FWHM of the pulse duration is shown of the pulse type map shown in Fig. A.23.

A.5 Soliton Self-Frequency Shift

A.5.1 Femtosecond Input Pulse

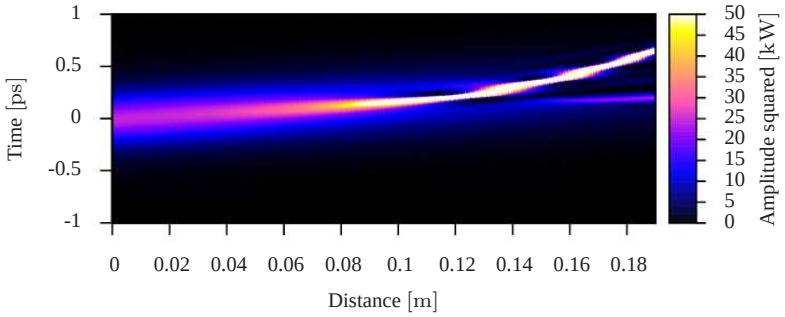

(a) The temporal evolution is shown as a contour plot of time and longitudinal position in the fibre.

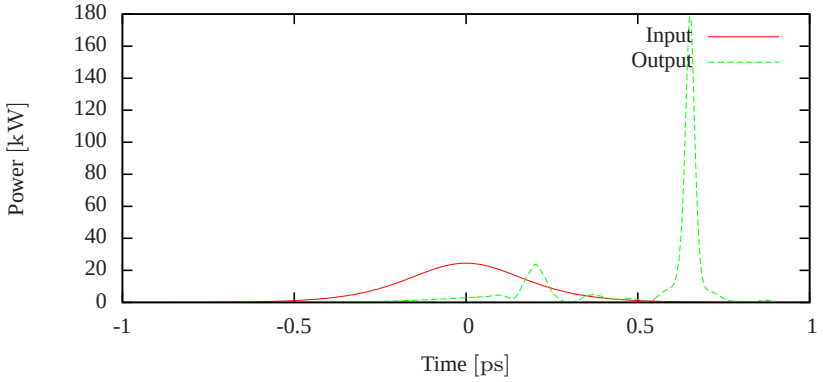

(b) Comparison of the input and the output temporal traces.

Figure A.26: Simulated pulse propagation in the LSF with an unchirped femtosecond pulse as the input pulse.

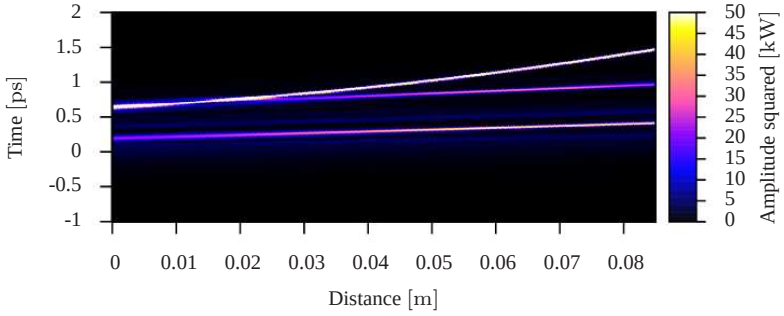

(a) The temporal evolution is shown as a contour plot of time and longitudinal position in the fibre.

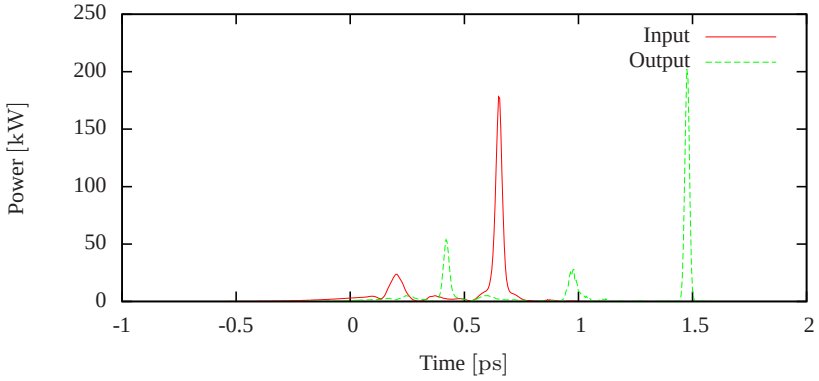

(b) Comparison of the input and the output temporal traces.

Figure A.27: Simulated pulse propagation in the RSF with an unchirped femtosecond pulse as the input pulse to the LSF.

A.5.2 Picosecond Input Pulse

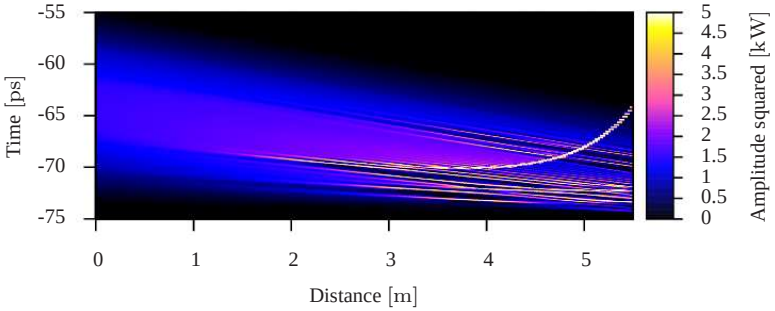

(a) The temporal evolution is shown as a contour plot of time and longitudinal position in the fibre.

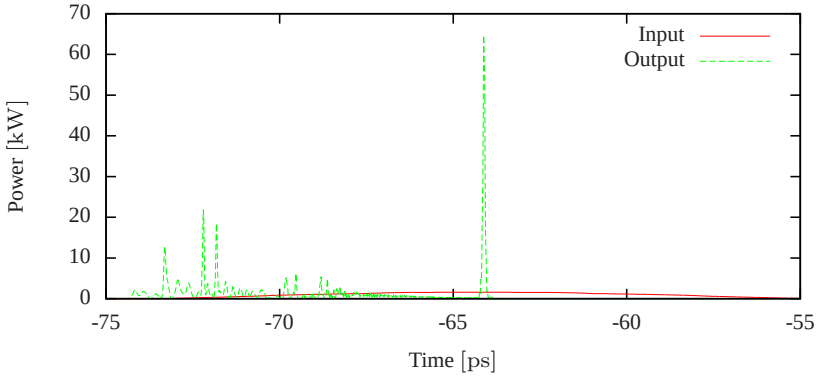

(b) Comparison of the input and the output temporal traces.

Figure A.28: Simulated pulse propagation in the LSF with an chirped picosecond pulse as the input pulse.

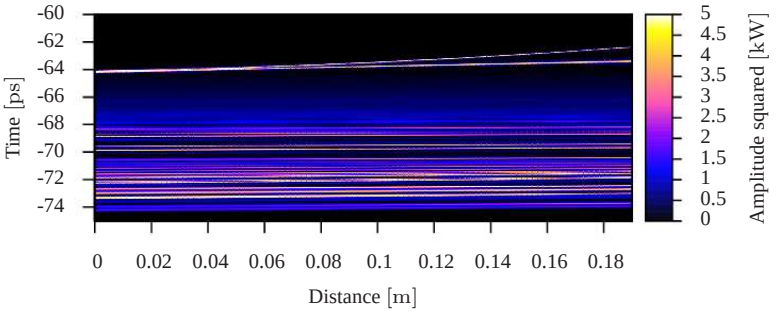

(a) The temporal evolution is shown as a contour plot of time and longitudinal position in the fibre.

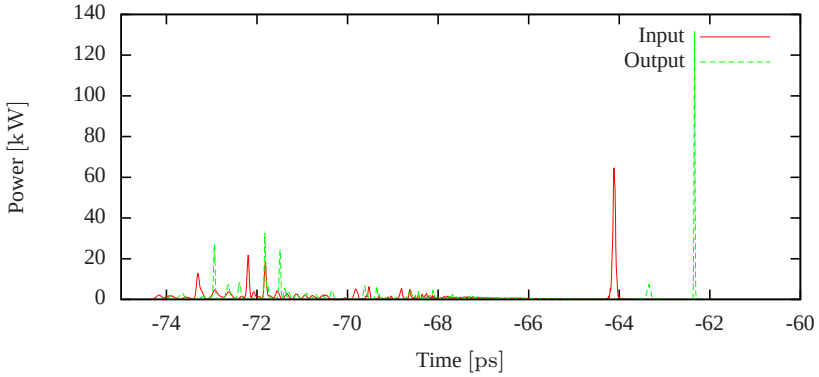

(b) Comparison of the input and the output temporal traces.

Figure A.29: Simulated pulse propagation in the RSF with an chirped picosecond pulse as the input pulse to the LSF.

A.6 Intermodal Non-linearity in Few-Moded Fibres

A.6.1 Čerenkov Radiation

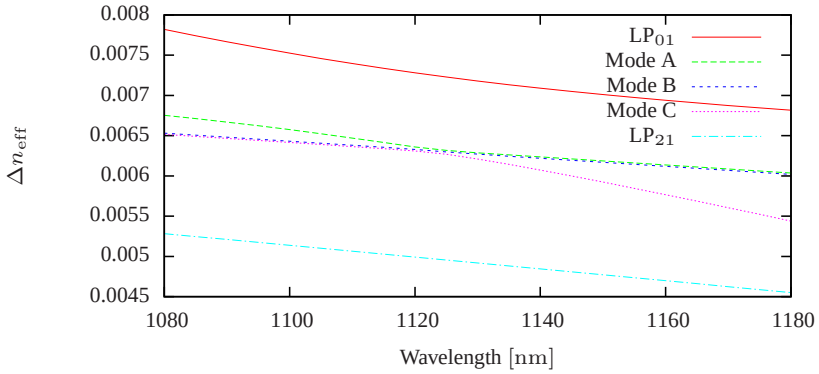

Figure A.30: The calculated effective indices for the LSF with an applied bend radius of 16 cm, where the material contribution from pure silica has been subtracted.

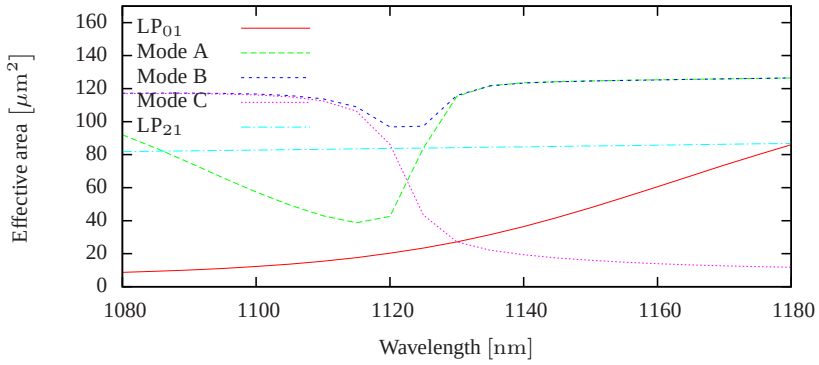

Figure A.31: The calculated effective area for the LSF with an applied bend radius of 16 cm.

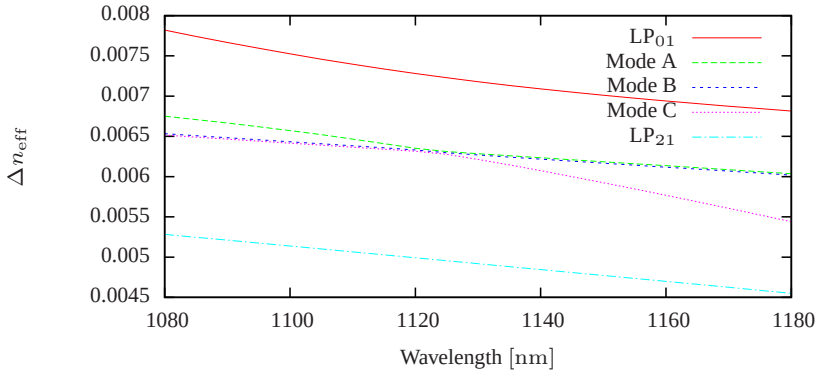

Figure A.32: .The calculated effective indices for the LSF with an applied bend radius of 30 cm, where the material contribution from pure silica has been subtracted.

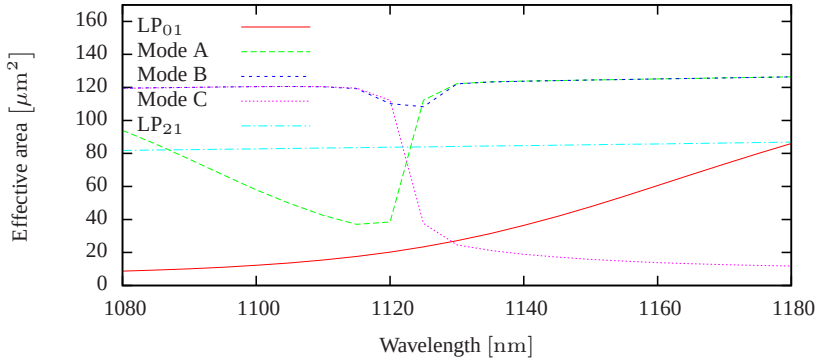

Figure A.33: The calculated effective area for the LSF with an applied bend radius of 30 cm.

Appendix B

Intramodal Soliton Self-Frequency Shift

In general there is nothing new in scientific terms in this appendix, as soliton propagation has been demonstrated numerous times before in the erbium gain-region and in highly non-linear fibres (HNLFs). This appendix is more meant to be an introduction to the soliton self-frequency shift (SSFS). The work, which the content of this appendix is based on, was carried out in the beginning of the Ph.D. for the purpose of obtained numerical and experimental experience with the SSFS process. The oscillator, which provided the seed pulse, is a figure-eight laser described in the next section. The output pulse from the figure-eight laser was amplified before being coupled into the HNLF. In the HNLF the pulse formed a soliton pulse, which shifted to longer wavelength via the SSFS process, which is described in the final section of this chapter.

B.1 Figure-Eight Laser

The figure-eight laser has received significant attention since the beginning of the 1990s [105–107]. The name comes from the physical appearance of the laser. A sketch of the lay-out of the laser is shown in Fig. B.1. The laser was originally built by a former OFS Fitel Denmark employee and was inspired by a laser built by *Jeffrey W. Nicholson* from *OFS Laboratories*. The total length of the figure-eight cavity is 7.31 m, where the 2.55 m is the erbium-doped gain fibre and the rest is single-mode fibre (SMF). The group-velocity dispersion parameters of

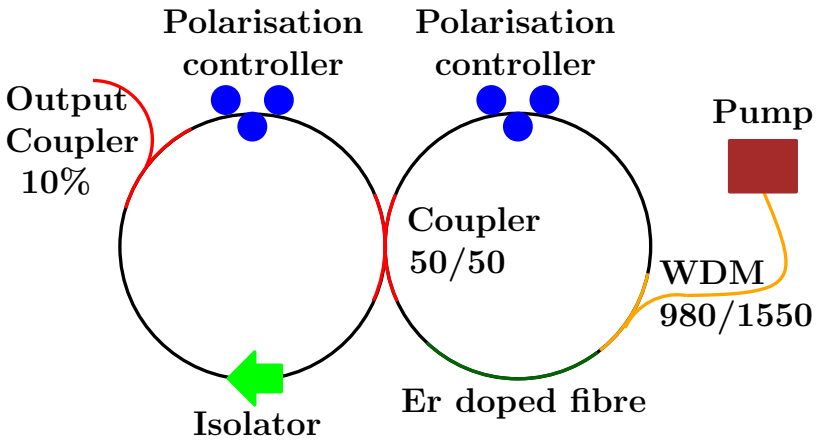

Figure B.1: Sketch of the figure-eight fibre laser.

the SMF and the erbium-doped gain fibre are 17 $\frac{\text{ps}}{\text{nm km}}$ and -38 $\frac{\text{ps}}{\text{nm km}}$ at a wavelength of 1550 nm, respectively. The peak absorption of the erbium-doped gain fibre is 40 $\frac{\text{dB}}{\text{m}}$ a at wavelength of 1530 nm.

The laser works by a non-linear amplifying loop mirror. The laser starts from noise, normally with the help of a physical perturbation. The pulse going along the direction of the isolator experiences a greater amplification and thereby the pulse becomes dominating. As the pulse which follows the direction of the isolator enters the gain fibre in the beginning of the right loop, the accumulated self-phase modulation (SPM) will be greater for this pulse in the final part of the loop. Therefore, the right loop works as a non-linear loop mirror, where the reflection varies sinusoidal as a function of intensity. The non-linear loop mirror behaves similar to a fast saturable absorber [83]. With a careful adjustment of the polarisation controllers, the laser mode-locks at a repetition rate of 28 MHz and an average output power of 0.58 dBm at a centre wavelength of 1570 nm. In Fig. B.2 the measured spectrum of the laser is shown. The spectral full-width at half-maximum (FWHM) is 30.9 nm. The second-harmonic generation (SHG) intensity autocorrelation shown in Fig. B.3 was measured after the pulse out of the figure-eight laser had been amplified and dechirped accordantly after the amplification process. The measured temporal FWHM of the pulse width under the assumption of a sech^2 intensity profile is fitted to 142 fs. There was 0.99 m of SMF before the erbium-doped gain fibre in the amplifier. The length of the erbium-doped gain fibre was 0.58 m and the fibre had

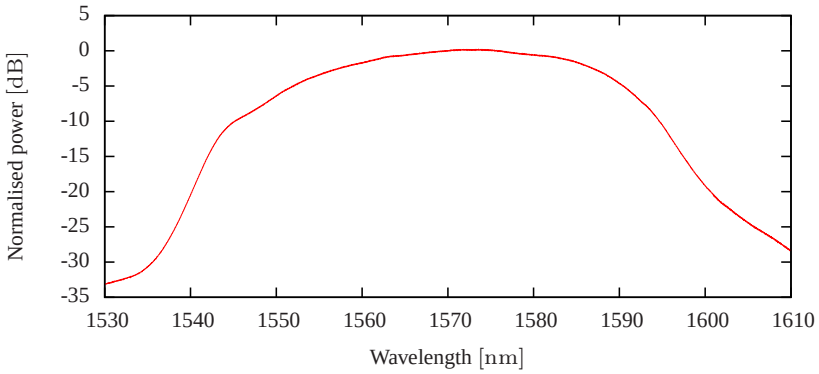

Figure B.2: Output spectrum of the figure-eight laser.

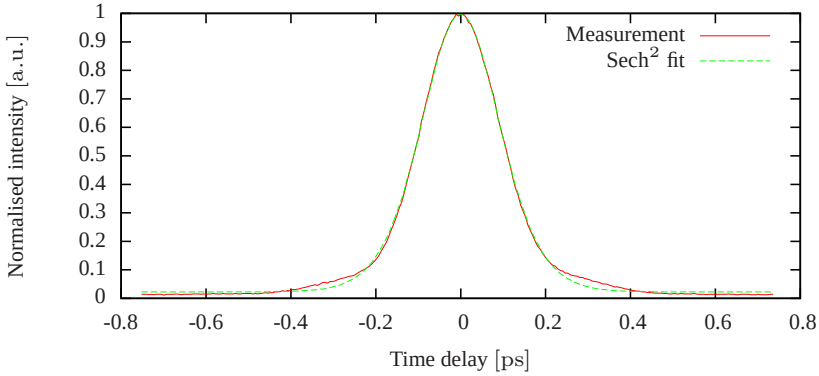

Figure B.3: Intensity autocorrelation for the figure-eight laser. The output has been amplified and compressed to increase the signal-to-noise ratio.

a group-velocity dispersion parameter of $-46.6\ \frac{\text{ps}}{\text{nm km}}$ at a wavelength of 1550 nm and a peak absorption of 150 $\frac{\text{dB}}{\text{m}}$ at a wavelength of 1530 nm. After the amplifier there was 4.40 m of SMF for re-compression. The maximum average output power after the amplifier stage was increased to 16.3 dBm.

B.2 Highly Non-Linear Fibre

The HNLF was spliced onto the compression fibre, which was used to compress the amplified output of the figure-eight laser. In Fig. B.4 the measured spectra after the 30 m of HNLF is shown as contour plot as a function of wavelength and pump current. The pump current is directly related to the pump power. The soliton is observed

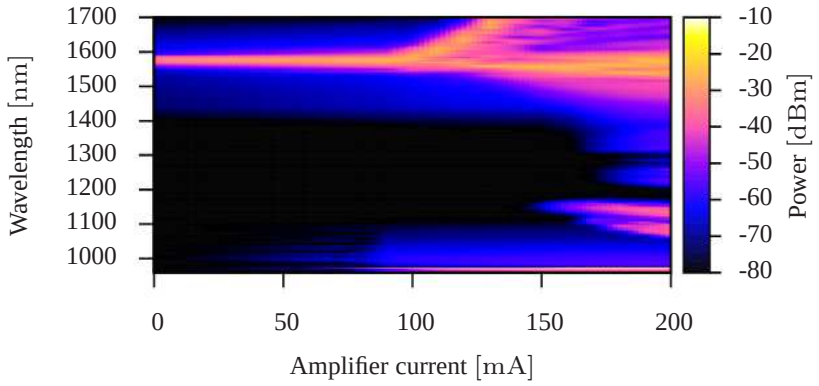

Figure B.4: The measured SSFS in 30 m of HNLF.

to split of the amplified input from the figure-eight laser and shift towards longer wavelengths at an amplifier current just above 100 mA. It is approximately at the same pump current that the residue from the 980 nm pump begins to be noticeable. At a pump current just above 150 mA light is generated approximately at a wavelength of 1100 nm, which is light generated by Čerenkov process in the normal dispersion region. Light generated by Čerenkov process is a special case of four-wave mixing (FWM) between a soliton and a dispersive wave in the normal dispersion region. The dispersion compression fibre, which the HNLF is spliced onto, is optimised for a maximum amplifier-current of

218 mA and therefore if the pump current was increased even further, it was expected that a non-linear effect will occur in the compression fibre. The non-linear interaction is in general a product of the peak power and the length. When the pulse is compressed the peak power increases and thereby the non-linear interaction. It is expected that the pulse experiences SPM in the compression fibre. It might also be possible to generate a soliton in the compression fibre, however, the soliton threshold is much lower in the HNLF due to a smaller effective area of the mode and a higher intensity-dependent index of refraction.

The observable SSFS in Fig. B.4 was limited by the bandwidth of the optical-spectrum analyser (OSA). However, simulations of the SSFS were carried out to longer wavelengths. To investigate the experiment shown in Fig. B.4, a transform limited soliton-pulse with a FWHM pulse duration of 144 fs is propagated through 4.30 m of pseudo fibre with the exact opposite group-velocity dispersion properties of a SMF and without non-linear effects. This is performed to ensure a chirped pulse, which is to be amplified and afterwards compressed in the 4.30 m of SMF. Thereafter, the pulse is propagated through 0.30 m of HNLF. In Fig. B.5 the output of the HNLF is shown for a variation in the pulse energy. Comparing Fig. B.4 and Fig. B.5, it is observed that the

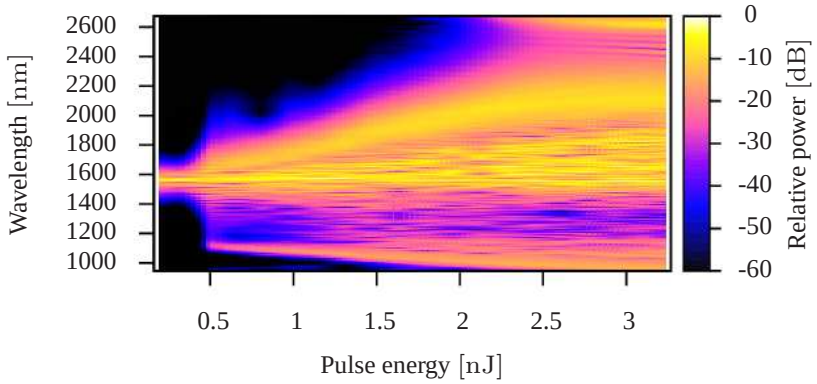

Figure B.5: The simulated SSFS in the HNLF.

simulation reproduces the features of the measurement. As the pulse energy is increased to approximately 2.5 nJ the soliton shift is halted at a wavelength approximately of 2200 nm and at the same time light is

generated at the edge of the simulation domain at a wavelength of approximately 2600 nm. This is an example of SSFS cancellation [66]. The SSFS is decreasing as the soliton approaches the second-zero-dispersion wavelength at 2290 nm and via the Čerenkov effect the soliton is phase-matched to a dispersive wave in the normal dispersion region, where the coupling strength is increasing as the soliton shifts closer to the zero-dispersion wavelength [65]. The transfer of energy from the soliton to the dispersive wave causes a spectral recoil-effect on the soliton, which shift the soliton away from the zero-dispersion wavelength SSFS [65]. As the SSFS and the spectral recoil-effect oppose each other the soliton comes to complete halt, when the effect from the two processes is equal. The group velocity dispersion and the effective area of the HNLF is shown in Fig. B.6. The HNLF has two zero dispersion wavelengths in

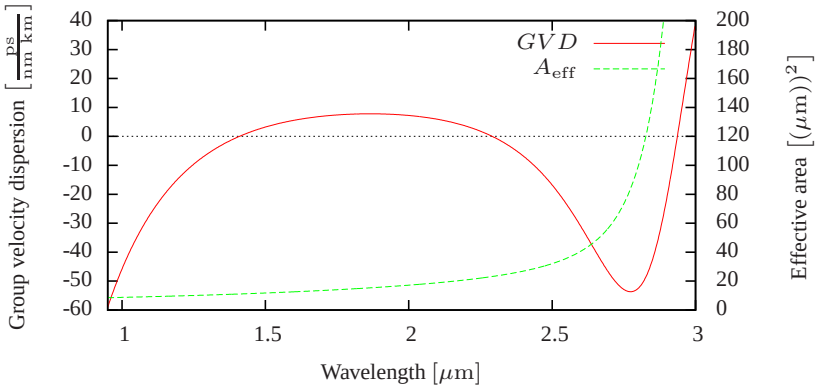

Figure B.6: The group velocity dispersion and the effective area of the HNLF.

the considered wavelength region. At the longer wavelengths the effective area is observed to rapidly increase, which indicates that the mode field of the fundamental mode is expanding further out in the cladding. The mode is guided, however the mode becomes more susceptible to micro and macro bends. This adds to the intrinsic loss, which also is rapidly increasing [108].

In summery the first dispersive wave generated by the Čerenkov process at approximately 1100 nm is generated in the beginning of the HNLF, when the soliton splits off the input pulse and shifts towards longer wavelengths. The second dispersive wave generated by the Čerenkov process at approximately 2600 nm is generated in the final part of the HNLF, when the SSFS is halted.

Appendix C

List of Acronyms

ANDi	all-normal dispersive
ASE	amplified spontaneous emission
CW	continuous-wave
DFB	distributed-feedback
FMF	few-moded fibre
FUT	fibre-under-test
FWHM	full-width at half-maximum
FWM	four-wave mixing
GNLSE	Generalised Non-Linear Schrödinger Equation
GVD	group-velocity dispersion
HNLF	highly non-linear fibre
HOM	higher-order-mode
LPG	long-period grating
LSF	left-sided fibre
MM	multi-mode
MMF	multi-mode fibre

MPI	multi-path interference
NLSE	Non-Linear Schrödinger Equation
OSA	optical-spectrum analyser
PCF	photonic-crystal fibre
PM	polarisation-maintaining
RF	radio frequency
RHS	right-hand side
RIN	relative-intensity noise
RK4IP	Fourth-Order Runge-Kutta in the Interaction-Picture
RSF	right-sided fibre
SBS	stimulated-Brillouin scattering
SESAM	semiconductor-saturable-absorber mirror
SHG	second-harmonic generation
SMCW-RSF	shorter mode-crossing wavelength variation of the right-sided fibre
SMF	single-mode fibre
SPM	self-phase modulation
SSFS	soliton self-frequency shift
TAP	turn-around-point
TFD-GNLSE	Transverse-Field Dispersion in the Generalised Non-Linear Schrödinger Equation
UV	ultraviolet
WDM	wavelength-division multiplexer

Appendix D

Bibliography

[1] T. H. Maiman, "Stimulated optical radiation in ruby," *Nature*, vol. 187, no. 4736, pp. 493–494, Aug 1960.

[2] A. L. Schawlow and C. H. Townes, "Infrared and optical masers," *Phys. Rev.*, vol. 112, pp. 1940–1949, Dec 1958.

[3] A. Javan, W. R. Bennett, and D. R. Herriott, "Population inversion and continuous optical maser oscillation in a gas discharge containing a he-ne mixture," *Phys. Rev. Lett.*, vol. 6, pp. 106–110, Feb 1961.

[4] P. A. Franken, A. E. Hill, C. W. Peters, and G. Weinreich, "Generation of optical harmonics," *Phys. Rev. Lett.*, vol. 7, pp. 118–119, Aug 1961.

[5] E. Snitzer, "Optical maser action of nd^{+3} in a barium crown glass," *Phys. Rev. Lett.*, vol. 7, pp. 444–446, Dec 1961.

[6] R. N. Hall, G. E. Fenner, J. D. Kingsley, T. J. Soltys, and R. O. Carlson, "Coherent light emission from gaas junctions," *Phys. Rev. Lett.*, vol. 9, pp. 366–368, Nov 1962.

[7] Nobelprize.org. (2013, 8 Apr) The nobel prize in physics 2009. [Online]. Available: `http://www.nobelprize.org/nobel_prizes/physics/aureates/2009/`

[8] J. Nilsson, W. Clarkson, R. Selvas, J. Sahu, P. Turner, S.-U. Alam, and A. Grudinin, "High-power wavelength-tunable

cladding-pumped rare-earth-doped silica fiber lasers," *Optical Fiber Technology*, vol. 10, no. 1, pp. 5 – 30, 2004.

[9] G. P. Agrawal, *Nonlinear Fiber Optics*, 4th ed. Academic Press, 2007.

[10] C. Yoon, Y. Choi, M. Kim, J. Moon, D. Kim, and W. Choi, "Experimental measurement of the number of modes for a multimode optical fiber," *Opt. Lett.*, vol. 37, no. 21, pp. 4558–4560, Nov 2012.

[11] C. D. Poole, J. M. Wiesenfeld, A. R. McCormick, and K. T. Nelson, "Broadband dispersion compensation by using the higher-order spatial mode in a two-mode fiber," *Opt. Lett.*, vol. 17, no. 14, pp. 985–987, Jul 1992.

[12] C. Poole, J. Wiesenfeld, D. DiGiovanni, and A. M. Vengsarkar, "Optical fiber-based dispersion compensation using higher order modes near cutoff," *Lightwave Technology, Journal of*, vol. 12, no. 10, pp. 1746–1758, 1994.

[13] S. Ramachandran, B. Mikkelsen, L. Cowsar, M. Yan, G. Raybon, L. Boivin, M. Fishteyn, W. Reed, P. Wisk, D. Brownlow, R. Huff, and L. Gruner-Nielsen, "All-fiber grating-based higher order mode dispersion compensator for broad-band compensation and 1000-km transmission at 40 gb/s," *Photonics Technology Letters, IEEE*, vol. 13, no. 6, pp. 632 –634, june 2001.

[14] S. Ramachandran, J. W. Nicholson, S. Ghalmi, M. F. Yan, P. Wisk, E. Monberg, and F. V. Dimarcello, "Light propagation with ultralarge modal areas in optical fibers," *Opt. Lett.*, vol. 31, no. 12, pp. 1797–1799, Jun 2006.

[15] S. Ramachandran, S. Ghalmi, J. W. Nicholson, M. F. Yan, P. Wisk, E. Monberg, and F. V. Dimarcello, "Anomalous dispersion in a solid, silica-based fiber," *Opt. Lett.*, vol. 31, no. 17, pp. 2532–2534, Sep 2006.

[16] T. Morioka, Y. Awaji, R. Ryf, P. Winzer, D. Richardson, and F. Poletti, "Enhancing optical communications with brand new fibers," *Communications Magazine, IEEE*, vol. 50, no. 2, pp. s31 –s42, february 2012.

[17] R. Ryf, S. Randel, A. H. Gnauck, C. Bolle, A. Sierra, S. Mumtaz, M. Esmaeelpour, E. C. Burrows, R.-J. Essiambre, P. J. Winzer, D. W. Peckham, A. H. McCurdy, and R. Lingle, "Mode-division multiplexing over 96 km of few-mode fiber using coherent 6 × 6 mimo processing," *J. Lightwave Technol.*, vol. 30, no. 4, pp. 521–531, Feb 2012.

[18] V. Sleiffer, Y. Jung, V. Veljanovski, R. van Uden, M. Kuschnerov, H. Chen, B. Inan, L. G. Nielsen, Y. Sun, D. Richardson, S. Alam, F. Poletti, J. Sahu, A. Dhar, A. Koonen, B. Corbett, R. Winfield, A. Ellis, and H. de Waardt, "73.7 tb/s (96 x 3 x 256-gb/s) mode-division-multiplexed dp-16qam transmission with inline mm-edfa," *Opt. Express*, vol. 20, no. 26, pp. B428–B438, Dec 2012.

[19] N. Bozinovic, Y. Yue, Y. Ren, M. Tur, P. Kristensen, A. Willner, and S. Ramachandran, "Orbital angular momentum (oam) based mode division multiplexing (mdm) over a km-length fiber," in *European Conference and Exhibition on Optical Communication*. Optical Society of America, 2012, p. Th.3.C.6.

[20] D. Kobat, M. E. Durst, N. Nishimura, A. W. Wong, C. B. Schaffer, and C. Xu, "Deep tissue multiphoton microscopy using longer wavelength excitation," *Opt. Express*, vol. 17, no. 16, pp. 13 354–13 364, Aug 2009.

[21] D. Kobat, N. G. Horton, and C. Xu, "In vivo two-photon imaging of cortical vasculature in mice to 1.5-mm depth with 1280-nm excitation," in *CLEO:2011 - Laser Applications to Photonic Applications*. Optical Society of America, 2011, p. PDPB3.

[22] ——, "In vivo two-photon microscopy to 1.6-mm depth in mouse cortex," *Journal of Biomedical Optics*, vol. 16, no. 10, p. 106014, 2011.

[23] N. G. Horton, K. Wang, D. Kobat, F. W. Wise, C. B. Schaffer, and C. Xu, "In vivo three-photon microscopy of subcortical structures within an intact mouse brain." Optical Society of America, 2012, p. CTh5C.5.

[24] N. G. Horton, K. Wang, D. Kobat, C. G. Clark, F. W. Wise, C. B. Schaffer, and C. Xu, "In vivo three-photon microscopy of

subcortical structures within an intact mouse brain," *Nat Photon*, vol. 7, no. 3, pp. 205–209, Mar 2013.

[25] F. M. Mitschke and L. F. Mollenauer, "Discovery of the soliton self-frequency shift," *Opt. Lett.*, vol. 11, no. 10, pp. 659–661, Oct 1986.

[26] J. P. Gordon, "Theory of the soliton self-frequency shift," *Opt. Lett.*, vol. 11, no. 10, pp. 662–664, Oct 1986.

[27] J. Knight, J. Arriaga, T. Birks, A. Ortigosa-Blanch, W. Wadsworth, and P. Russell, "Anomalous dispersion in photonic crystal fiber," *Photonics Technology Letters, IEEE*, vol. 12, no. 7, pp. 807 –809, july 2000.

[28] I. Cormack, D. Reid, W. Wadsworth, J. Knight, and P. Russell, "Observation of soliton self-frequency shift in photonic crystal fibre," *Electronics Letters*, vol. 38, no. 4, pp. 167 –169, feb 2002.

[29] D. G. Ouzounov, F. R. Ahmad, D. Müller, N. Venkataraman, M. T. Gallagher, M. G. Thomas, J. Silcox, K. W. Koch, and A. L. Gaeta, "Generation of megawatt optical solitons in hollow-core photonic band-gap fibers," *Science*, vol. 301, no. 5640, pp. 1702–1704, 2003.

[30] J. van Howe, J. H. Lee, S. Zhou, F. Wise, C. Xu, S. Ramachandran, S. Ghalmi, and M. F. Yan, "Demonstration of soliton self-frequency shift below 1300nm in higher-order mode, solid silica-based fiber," *Opt. Lett.*, vol. 32, no. 4, pp. 340–342, Feb 2007.

[31] R. Hellwarth, "Third-order optical susceptibilities of liquids and solids," *Progress in Quantum Electronics*, vol. 5, pp. 1–68, 1979.

[32] P. Butcher and D. Cotter, *The Elements of Nonlinear Optics*, ser. Cambridge Studies in Modern Optics. Cambridge University Press, 1991.

[33] S. A. V. and T. M. Monro, "A full vectorial model for pulse propagation in emerging waveguides with subwavelength structures part i: Kerr nonlinearity," *Opt. Express*, vol. 17, no. 4, pp. 2298–2318, Feb 2009.

[34] M. D. Turner, T. M. Monro, and S. A. V., "A full vectorial model for pulse propagation in emerging waveguides with subwavelength structures part ii: Stimulated raman scattering," *Opt. Express*, vol. 17, no. 14, pp. 11 565–11 581, Jul 2009.

[35] S. A. V., W. Q. Zhang, H. Ebendorff-Heidepriem, and T. M. Monro, "Small core optical waveguides are more nonlinear than expected: experimental confirmation," *Opt. Lett.*, vol. 34, no. 22, pp. 3577–3579, Nov 2009.

[36] K. Blow and D. Wood, "Theoretical description of transient stimulated raman scattering in optical fibers," *Quantum Electronics, IEEE Journal of*, vol. 25, no. 12, pp. 2665–2673, 1989.

[37] D. Milam, "Review and assessment of measured values of the nonlinear refractive-index coefficient of fused silica," *Appl. Opt.*, vol. 37, no. 3, pp. 546–550, Jan 1998.

[38] J. Laegsgaard, "Mode profile dispersion in the generalised nonlinear schrödinger equation," *Opt. Express*, vol. 15, no. 24, pp. 16 110–16 123, Nov 2007.

[39] D. Hollenbeck and C. D. Cantrell, "Multiple-vibrational-mode model for fiber-optic raman gain spectrum and response function," *J. Opt. Soc. Am. B*, vol. 19, no. 12, pp. 2886–2892, Dec 2002.

[40] Q. Lin and G. P. Agrawal, "Raman response function for silica fibers," *Opt. Lett.*, vol. 31, no. 21, pp. 3086–3088, Nov 2006.

[41] R. H. Stolen, J. P. Gordon, W. J. Tomlinson, and H. A. Haus, "Raman response function of silica-core fibers," *J. Opt. Soc. Am. B*, vol. 6, no. 6, pp. 1159–1166, Jun 1989.

[42] J. Hult, "A fourth-order runge–kutta in the interaction picture method for simulating supercontinuum generation in optical fibers," *J. Lightwave Technol.*, vol. 25, no. 12, pp. 3770–3775, Dec 2007.

[43] A. Hasegawa and F. Tappert, "Transmission of stationary nonlinear optical pulses in dispersive dielectric fibers. i. anomalous dispersion," *Applied Physics Letters*, vol. 23, no. 3, pp. 142–144, 1973.

[44] ——, "Transmission of stationary nonlinear optical pulses in dispersive dielectric fibers. ii. normal dispersion," *Applied Physics Letters*, vol. 23, no. 4, pp. 171–172, 1973.

[45] F. Poletti and P. Horak, "Description of ultrashort pulse propagation in multimode optical fibers," *J. Opt. Soc. Am. B*, vol. 25, no. 10, pp. 1645–1654, Oct 2008.

[46] ——, "Dynamics of femtosecond supercontinuum generation in multimode fibers," *Opt. Express*, vol. 17, no. 8, pp. 6134–6147, Apr 2009.

[47] M. Kolesik, E. Wright, and J. Moloney, "Simulation of femtosecond pulse propagation in sub-micron diameter tapered fibers," *Applied Physics B: Lasers and Optics*, vol. 79, pp. 293–300, 2004.

[48] M. Pedersen, P. Kristensen, L. Gruner-Nielsen, and K. Rottwitt, "Impact of the scalar approximation on the prediction of the group velocity dispersion," *Lightwave Technology, Journal of*, vol. 29, no. 21, pp. 3129 –3134, nov.1, 2011.

[49] M. Pedersen, T. Palsson, K. Jespersen, D. Jakobsen, B. Palsdottir, and K. Rottwitt, "The raman contribution to the intensity dependent refractive index in optical fibers," in *Photonics Conference (PHO), 2011 IEEE*, oct. 2011, pp. 571 –572.

[50] K. S. Kim, R. H. Stolen, W. A. Reed, and K. W. Quoi, "Measurement of the nonlinear index of silica-core and dispersion-shifted fibers," *Opt. Lett.*, vol. 19, no. 4, pp. 257–259, Feb 1994.

[51] T. Kato, Y. Suetsugu, and M. Nishimura, "Estimation of nonlinear refractive index in various silica-based glasses for optical fibers," *Opt. Lett.*, vol. 20, no. 22, pp. 2279–2281, Nov 1995.

[52] A. Boskovic, S. V. Chernikov, J. R. Taylor, L. Gruner-Nielsen, and O. A. Levring, "Direct continuous-wave measurement of n2 in various types of telecommunication fiber at 1.55 μm," *Opt. Lett.*, vol. 21, no. 24, pp. 1966–1968, Dec 1996.

[53] D. Philen, D. Peckham, and I. Brener, "Measurement of the nonlinear index of refraction, n2, for various fiber types," in *Optical Fiber Communication Conference, 2000*, vol. 3, 2000, pp. 184 –186 vol.3.

[54] K. Nakajima and M. Ohashi, "Dopant dependence of effective nonlinear refractive index in geo 2- and f-doped core single-mode fibers," *Photonics Technology Letters, IEEE*, vol. 14, no. 4, pp. 492 –494, apr 2002.

[55] A. Martínez-Rios, A. N. Starodumov, Y. O. Barmenkov, V. N. Filippov, and I. Torres-Gomez, "Influence of the symmetry rules for raman susceptibility on the accuracy of nonlinear index measurements in optical fibers," *J. Opt. Soc. Am. B*, vol. 18, no. 6, pp. 794–803, Jun 2001.

[56] F. A. Oguama, H. Garcia, and A. M. Johnson, "Simultaneous measurement of the raman gain coefficient and the nonlinear refractive index of optical fibers: theory and experiment," *J. Opt. Soc. Am. B*, vol. 22, no. 2, pp. 426–436, Feb 2005.

[57] S. Herstrøm, L. Grüner-Nielsen, and B. Pálsdóttir, "Acoustic index of ge-doped optical fibers," *Opt. Lett.*, vol. 34, no. 23, pp. 3689–3691, Dec 2009.

[58] K. Rottwitt, J. Bromage, A. J. Stentz, L. Leng, M. E. Lines, and H. Smith, "Scaling of the raman gain coefficient: Applications to germanosilicate fibers," *J. Lightwave Technol.*, vol. 21, no. 7, p. 1652, Jul 2003.

[59] D. Hutchings, M. Sheik-Bahae, D. Hagan, and E. Stryland, "Kramers-krönig relations in nonlinear optics," *Optical and Quantum Electronics*, vol. 24, pp. 1–30, 1992.

[60] M. E. Pedersen, J. Cheng, K. Charan, K. Wang, C. Xu, L. Grüner-Nielsen, and D. Jakobsen, "Optimization of a higher-order-mode fiber for energetic soliton propagation," in *CLEO: Science and Innovations*. Optical Society of America, 2012, p. CTh4G.2.

[61] ——, "Higher-order-mode fiber optimized for energetic soliton propagation," *Opt. Lett.*, vol. 37, no. 16, pp. 3459–3461, Aug 2012.

[62] S. Ramachandran, Ed., *Fiber based dispersion compensation*, ser. Optical and Fiber Communications Reports. Springer, 2007, ch. Fiber design for high figure of merit and high slope dispersion compensating fibers.

[63] Y. Kodama and A. Hasegawa, "Nonlinear pulse propagation in a monomode dielectric guide," *Quantum Electronics, IEEE Journal of*, vol. 23, no. 5, pp. 510–524, 1987.

[64] C. Agger, S. T. Sørensen, C. L. Thomsen, S. R. Keiding, and O. Bang, "Nonlinear soliton matching between optical fibers," *Opt. Lett.*, vol. 36, no. 13, pp. 2596–2598, Jul 2011.

[65] N. Akhmediev and M. Karlsson, "Cherenkov radiation emitted by solitons in optical fibers," *Physical Review A*, vol. 51, pp. 2602–2607, Mar. 1995.

[66] D. V. Skryabin, F. Luan, J. C. Knight, and P. S. J. Russell, "Soliton self-frequency shift cancellation in photonic crystal fibers," *Science*, vol. 301, no. 5640, pp. 1705–1708, 2003.

[67] D. Menashe, M. Tur, and Y. Danziger, "Interferometric technique for measuring dispersion of high order modes in optical fibres," *Electronics Letters*, vol. 37, no. 24, pp. 1439 –1440, nov 2001.

[68] J. Cheng, M. E. V. Pedersen, K. Wang, C. Xu, L. Grüner-Nielsen, and D. Jakobsen, "Time-domain multimode dispersion measurement in a higher-order-mode fiber," *Opt. Lett.*, vol. 37, no. 3, pp. 347–349, Feb 2012.

[69] D. Donlagic, "In-line higher order mode filters based on long highly uniform fiber tapers," *Lightwave Technology, Journal of*, vol. 24, no. 9, pp. 3532 –3539, sept. 2006.

[70] I. K. Hwang, S. H. Yun, and B. Y. Kim, "Long-period fiber gratings based on periodic microbends," *Opt. Lett.*, vol. 24, no. 18, pp. 1263–1265, Sep 1999.

[71] S. Savin, M. F. Digonnet, G. S. Kino, and H. J. Shaw, "Tunable mechanically induced long-period fiber gratings," *Opt. Lett.*, vol. 25, no. 10, pp. 710–712, May 2000.

[72] D. Davis, T. Gaylord, E. Glytsis, S. Kosinski, S. Mettler, and A. Vengsarkar, "Long-period fibre grating fabrication with focused co2 laser pulses," *Electronics Letters*, vol. 34, no. 3, pp. 302 –303, feb 1998.

[73] C. Smelser, S. Mihailov, and D. Grobnic, "Formation of type i-ir and type ii-ir gratings with an ultrafast ir laser and a phase mask," *Opt. Express*, vol. 13, no. 14, pp. 5377–5386, Jul 2005.

[74] K. O. Hill, Y. Fujii, D. C. Johnson, and B. S. Kawasaki, "Photosensitivity in optical fiber waveguides: Application to reflection filter fabrication," *Applied Physics Letters*, vol. 32, no. 10, pp. 647 –649, may 1978.

[75] M. Beijersbergen, R. Coerwinkel, M. Kristensen, and J. Woerdman, "Helical-wavefront laser beams produced with a spiral phaseplate," *Optics Communications*, vol. 112, no. 5-6, pp. 321 – 327, 1994.

[76] M. A. A. Neil, F. Massoumian, R. Juškaitis, and T. Wilson, "Method for the generation of arbitrary complex vector wave fronts," *Opt. Lett.*, vol. 27, no. 21, pp. 1929–1931, Nov 2002.

[77] S. Ramachandran, Z. Wang, and M. Yan, "Bandwidth control of long-period grating-based mode converters in few-mode fibers," *Opt. Lett.*, vol. 27, no. 9, pp. 698–700, May 2002.

[78] P. Lemaire, R. Atkins, V. Mizrahi, and W. Reed, "High pressure h2 loading as a technique for achieving ultrahigh uv photosensitivity and thermal sensitivity in geo2 doped optical fibres," *Electronics Letters*, vol. 29, no. 13, pp. 1191 –1193, june 1993.

[79] S. Ramachandran, S. Ghalmi, S. Chandrasekhar, I. Ryazansky, M. Yan, F. Dimarcello, W. REED, and P. Wisk, "Tunable dispersion compensators utilizing higher order mode fibers," *Photonics Technology Letters, IEEE*, vol. 15, no. 5, pp. 727–729, 2003.

[80] T. Volotinen, M. Zimnol, M. Tomozawa, Y.-K. Lee, and K. Raine, "Effect of mechanical stripping and arc-fusion on the strength and aging of a spliced recoated optical fiber," *MRS Proceedings*, vol. 531, 0 1998.

[81] K. Jespersen, Z. Li, L. Gruner-Nielsen, B. Palsdottir, F. Poletti, and J. W. Nicholson, "Measuring distributed mode scattering in long, few-moded fibers," in *Optical Fiber Communication Conference*. Optical Society of America, 2012, p. OTh3I.4.

[82] L. Gruner-Nielsen, Y. Sun, J. Nicholson, D. Jakobsen, K. Jespersen, R. Lingle, and B. Palsdottir, "Few mode transmission fiber with low dgd, low mode coupling, and low loss," *Lightwave Technology, Journal of*, vol. 30, no. 23, pp. 3693–3698, 2012.

[83] J. Diels and W. Rudolph, *Ultrashort Laser Pulse Phenomena*, 2nd ed. Academic Press, 2006.

[84] M. Pedersen, E. Kelleher, J. Travers, Z. Sun, T. Hasan, A. Ferrari, S. Popov, and J. Taylor, "Stable gain-guided soliton propagation in a polarized yb-doped mode-locked fiber laser," *Photonics Journal, IEEE*, vol. 4, no. 3, pp. 1058 –1064, june 2012.

[85] A. Chong, J. Buckley, W. Renninger, and F. Wise, "All-normal-dispersion femtosecond fiber laser," *Opt. Express*, vol. 14, no. 21, pp. 10 095–10 100, Oct 2006.

[86] B. G. Bale, J. N. Kutz, A. Chong, W. H. Renninger, and F. W. Wise, "Spectral filtering for high-energy mode-locking in normal dispersion fiber lasers," *J. Opt. Soc. Am. B*, vol. 25, no. 10, pp. 1763–1770, Oct 2008.

[87] W. H. Renninger, A. Chong, and F. W. Wise, "Dissipative solitons in normal-dispersion fiber lasers," *Phys. Rev. A*, vol. 77, no. 2, p. 023814, Feb 2008.

[88] A. Chong, W. H. Renninger, and F. W. Wise, "Properties of normal-dispersion femtosecond fiber lasers," *J. Opt. Soc. Am. B*, vol. 25, no. 2, pp. 140–148, Feb 2008.

[89] L. M. Zhao, D. Y. Tang, H. Zhang, T. H. Cheng, H. Y. Tam, and C. Lu, "Dynamics of gain-guided solitons in an all-normal-dispersion fiber laser," *Opt. Lett.*, vol. 32, no. 13, pp. 1806–1808, Jul 2007.

[90] J. Travers, J. Morgenweg, E. Obraztsova, A. Chernov, E. Kelleher, and S. Popov, "Using the e22 transition of carbon nanotubes for fiber laser mode-locking," *Laser Physics Letters*, vol. 8, no. 2, pp. 144–149, 2011.

[91] A. Heidt, "Efficient adaptive step size method for the simulation of supercontinuum generation in optical fibers," *Lightwave Technology, Journal of*, vol. 27, no. 18, pp. 3984 –3991, sept.15, 2009.

[92] M. Schultz, H. Karow, D. Wandt, U. Morgner, and D. Kracht, "Ytterbium femtosecond fiber laser without dispersion compensation tunable from 1015 nm to 1050 nm," *Optics Communications*, vol. 282, no. 13, pp. 2567 – 2570, 2009.

[93] L. Kong, X. Xiao, and C. Yang, "Tunable all-normal-dispersion yb-doped mode-locked fiber lasers," *Laser Physics*, vol. 20, pp. 834–837, 2010.

[94] J. Cheng, M. Pedersen, K. Charan, C. Xu, L. Gruner-Nielsen, and D. Jacobsen, "High-efficiency intermodal four-wave mixing in a higher-order-mode fiber," in *Lasers and Electro-Optics (CLEO), 2012 Conference on*, may 2012, pp. 1 –2.

[95] J. Cheng, M. E. V. Pedersen, K. Charan, K. Wang, C. Xu, L. Gruner-Nielsen, and D. Jakobsen, "Intermodal four-wave mixing in a higher-order-mode fiber," *Applied Physics Letters*, vol. 101, no. 16, p. 161106, 2012.

[96] M. Pedersen, J. Cheng, C. Xu, and K. Rottwitt, "Transverse field dispersion in the generalised non-linear schrödinger equation: Four wave mixing in a higher-order-mode fiber," *Lightwave Technology, Journal of*, Submitted.

[97] J. Cheng, M. Pedersen, K. Charan, K. Wang, C. Xu, L. Grüner-Nielsen, and D. Jakobsen, "Simultaneous wavelength and mode conversion in a higher-order-mode fiber," in *Frontiers in Optics Conference*. Optical Society of America, 2012, p. FW5D.4.

[98] J. Cheng, M. E. V. Pedersen, K. Charan, K. Wang, C. Xu, L. Grüner-Nielsen, and D. Jakobsen, "Intermodal cherenkov radiation in a higher-order-mode fiber," *Opt. Lett.*, vol. 37, no. 21, pp. 4410–4412, Nov 2012.

[99] C. de Matos, J. Taylor, T. Hansen, K. Hansen, and J. Broeng, "All-fiber chirped pulse amplification using highly-dispersive air-core photonic bandgap fiber," *Opt. Express*, vol. 11, no. 22, pp. 2832–2837, Nov 2003.

[100] J. Limpert, T. Schreiber, S. Nolte, H. Zellmer, and A. Tünnermann, "All fiber chirped-pulse amplification system based on compression in air-guiding photonic bandgap fiber," *Opt. Express*, vol. 11, no. 24, pp. 3332–3337, Dec 2003.

[101] K. O. Hill, "Aperiodic distributed-parameter waveguides for integrated optics," *Appl. Opt.*, vol. 13, no. 8, pp. 1853–1856, Aug 1974.

[102] K. O. Hill, F. Bilodeau, B. Malo, T. Kitagawa, S. Thériault, D. C. Johnson, J. Albert, and K. Takiguchi, "Chirped in-fiber bragg gratings for compensation of optical-fiber dispersion," *Opt. Lett.*, vol. 19, no. 17, pp. 1314–1316, Sep 1994.

[103] J. Nicholson, A. Yablon, J. Fini, and M. Mermelstein, "Measuring the modal content of large-mode-area fibers," *Selected Topics in Quantum Electronics, IEEE Journal of*, vol. 15, no. 1, pp. 61–70, 2009.

[104] J. Jackson, *Classical electrodynamics*, 3rd ed. Wiley, 1998.

[105] D. Richardson, R. Laming, D. Payne, V. Matsas, and M. Phillips, "Selfstarting, passively modelocked erbium fibre ring laser based on the amplifying sagnac switch," *Electronics Letters*, vol. 27, no. 6, pp. 542 –544, march 1991.

[106] I. Duling, I.N., "Subpicosecond all-fibre erbium laser," *Electronics Letters*, vol. 27, no. 6, pp. 544 –545, march 1991.

[107] J. Nicholson, A. Yablon, P. Westbrook, K. Feder, and M. Yan, "High power, single mode, all-fiber source of femtosecond pulses at 1550 nm and its use in supercontinuum generation," *Opt. Express*, vol. 12, no. 13, pp. 3025–3034, Jun 2004.

[108] S. Kobayashi, T. Izawa, N. Shibata, and S. Shibata, "Characteristics of optical fibers in infrared wavelength region," *Electronics Communications of Japan*, vol. 26, pp. 453–467, Apr. 1978.